Determination of the non-linear roll damping of a barge by means of viscous flow simulations

Anastasios Stampoultzoglou

Technische Universiteit Delft

TU Delft

Seaway Heavy Lifting

Determination of the nonlinear roll damping of a barge by means of viscous flow simulations

An advanced approach to compute roll damping characteristics with CFD

by

Anastasios Stampoultzoglou

to obtain the degree of Master of Science in Offshore and Dredging Engineering at the Delft University of Technology, to be defended publicly on Monday September 4, 2017 at 10:00 AM.

Student number:	4500172	
Project duration:	September 29, 2016 – September 4, 2017	
Thesis committee:	Prof. Dr. A.V. Metrikine,	TU Delft, Chairman
	Dr.ir. Duncan R. van der Heul,	TU Delft, Supervisor
	Dr.ir. Yang Qu,	TU Delft, Supervisor
	Roy Weustink,	Seaway Heavy Lifting, Supervisor

This thesis is confidential and cannot be made public until September 4, 2017.
An electronic version of this thesis is available at `http://repository.tudelft.nl/`.

Seaway Heavy Lifting

Preface

First of all, I would like to thank Dr.ir. Duncan R. van der Heul, my supervisor, for his excellent guidance during this project. His patience, commitment and critical glance in combination with the fact that he was always available have undoubtedly contributed to complete this thesis. In addition, I would like to express my sincere gratitude and appreciation to Roy Weustink, my daily supervisor at Seaway Heavy Lifting, who truly believed in me, trusted me and gave me the chance to take decisions. He is always there to support me whenever I need him. Also, I own a thank you to Yang Qu, for his support and the constructive discussions that we had throughout the project.

My deep gratitude goes out to Prof. Dr. A.V. Metrikine for guiding me through the whole process and for his valuable suggestions about my thesis project that were absolutely decisive. The academic background that he provided me with through his courses is enormous and I would like to wholeheartedly express my gratitude to him.

Moreover, it is important to me to deeply thank Frederick Jaounen from Maritime Research Institute Netherlands (MARIN) for his advise and for sharing his valuable knowledge on this topic. In addition, I would like to thank CPU 24/7, which is a leading provider of CAE and HPC, for providing me with the required hardware for the implementation of this master thesis.

Last but not least, I would like to extend my sincere acknowledgment to Seaway Heavy Lifting as a company. Throughout my thesis I had the chance to collaborate with high calibre professionals who helped me and supported me every single time that I needed them.

Anastasios Stampoultzoglou
Delft, August 2017

Abstract

For many types of floating structures, roll motion is the most important wave induced motion. More specifically, roll motion is of high significance for barges, in order to correctly predict the acceleration of the structure caused by roll motion and determine the procedure of sea-fastening and off-loading.

The correct forecast of roll motion requires accurate estimation of roll damping. At the same time, the main sources of roll damping are the creation of waves, skin friction and creation of vortices (eddies), due to roll motion. For this reason, the physics of the problem cannot be fully described by a flow model based on potential theory, as it is highly dependent on vorticity and viscous effects. As a consequence, potential theory algorithms underestimate roll damping, which results in over-prediction of roll motion and thus in a conservative estimate of workability.

It is also important to mention that the vorticity and the viscous effects, lead to non-linear damping characteristics. More specifically, the roll damping moment is controlled by its odd numbered harmonics, the first of which is dominant. Consequently, it is common to express the damping moment in an equivalent linearized form, equal to the first harmonic.

During the last years simulating the flow around the rolling vessel using viscous-flow algorithms is becoming more and more popular. Using CFD (Computational Fluid Dynamics) is a cheap and fast way to create a "numerical" wave tank and perform numerical decay tests, forced roll simulations, and roll response simulations in regular waves. Of course the underlying algorithm should be validated, before any commercial or scientific use.

In this thesis, roll damping will be estimated by performing virtual forced oscillation tests, and the computed roll damping coefficients will be presented as a function of roll amplitude. The virtual forced oscillation tests have been performed with the open-source CFD software OpenFOAM. Additionally, numerous numerical experiments are performed in order to choose the optimum discretization schemes, turbulence model, mesh and time configurations. Finally, Ikeda's experimental data is used in order to validate the viscous-flow algorithm and the numerical model.

Two methodologies have been used in order to determine the non-linear roll damping. In the first case the free surface is included in the viscous-flow model, using the Volume of Fluid method. The second approach disregards any free surface effect and the total damping is calculated as a superposition of viscous (by viscous-flow algorithm) and wave (by potential theory algorithm) damping. Both approaches are compared with Ikeda's experimental data and it is concluded that both methods are able to capture accurately the linearized roll damping coefficients, for various amplitudes.

Finally, viscous-flow simulations of the full scale barge, in order to calculate the roll damping coefficients, are notably time-consuming. For this reason, in order to reduce the computational time, the methodology which neglects the free surface effect, is chosen, as it is a good compromise between time efficiency and accuracy.

Contents

List of Figures

List of Tables

Symbols

M_H	Total hydrodynamic moment
$M_{H\alpha}$	Amplitude of the total hydrodynamic moment
u	Flow velocity
U	Average flow velocity
g	Gravitational acceleration
p	Hydrodynamic pressure
r	Lever arm
$\boldsymbol{n}$	Unit normal vector
$\boldsymbol{t}$	Tangential vector
τ	Shear stress
S	Surface of the object
ϕ	Roll angle
F_f	Shear forces
F_p	Pressure forces
M_{tot}	Total moment
M_{ext}	External / excitation moment
M_a	Added mass moment
ε	Phase shift
$M_{b\alpha}$	Amplitude of the added damping moment
M_b	Added damping moment
M_c	Restoring moment
b_1, b_2, b_3	Non-linear roll damping coefficients
b_{eq}	Equivalent linearised roll damping
b_{tot}	Total roll damping
b_w	Wave damping
b_F	Frictional damping
b_E	Eddy damping
b_L	Lift damping
b_{BK}	Bilge keel damping
ρ_{water}	Density of water
ρ_{air}	Density of air
μ_{water}	Dynamic viscosity of water
μ_{air}	Dynamic viscosity of air
α	Volume fraction
y^+	Dimensionless distance
u^*	Friction velocity
τ_w	Wall shear stress
R	Reynolds shear tensor
I	Mass moment of inertia
$\gamma(l)$	Diffusivity
c	Restoring coefficient
a	Added mass
l	Cell distance to the nearest moving boundary
t	Time
$\boldsymbol{\omega}$	Frequency of the sinusoidal roll motion
ω	Frequency of turbulence
ϕ	Roll angle
ϕ_α	Roll amplitude
D	Draft

U_ϕ	Maximum velocity at the corner of the bilge
L_r	Level arm to the bilge corner
ν	Kinematic viscosity
μ	Dynamic viscosity
ν_t	Eddy kinematic viscosity
B	Breadth
b^*_{eq}	Dimensionless equivalent roll damping
b^*_1, b^*_2	Dimensionless non-linear roll damping coefficients
ω^*_z	Dimensionless vorticity
$\lambda_{1/2}$	Minimum length of the half domain
λ	Approximated length of the generated wave
N	Number of cycles
Δx	Half the breadth of the cross section
ω^*	Frequency of oscillation
VCG	Vertical Centre of Gravity

1

Determination of the roll damping by means of viscous-flow algorithm

1.1. Importance of roll damping

Roll motion is probably the most important wave induced motion of a floating structure (barge) in order to correctly predict the acceleration of the structure caused by roll motion and determine the procedure of sea-fastening and off-loading. At the same time the physics of the problem cannot be described by a flow model based on potential theory, as it is highly dependent on viscous effects. These viscous effects, lead to nonlinear damping characteristics. The use of a flow model based on potential theory results in over-prediction of the roll motion, which leads to a conservative estimate of workability.

During the past decades, several approaches were developed for prediction of roll damping characteristics. Both experimental (free-roll decay tests, excited roll motion, fixed roll axis technique) and theoretical approaches (Ikeda-Tanaka-Himeno method [23, 27]) have been proposed. Model testing is time consuming and expensive, making it unfeasible to investigate the roll damping dependency on amplitude, frequency and draft. Moreover experiments suffer from Reynolds scaling effects as generally Froude scaling is applied. The theoretical methods are based on limited numbers of hull shapes, while roll damping is highly shape dependent.

During the last years simulating the flow around the rolling vessel using viscous flow algorithms is becoming more and more popular. Using CFD (Computational Fluid Dynamics) is a cheap and fast way to create a "numerical" wave tank and perform numerical decay tests, forced roll simulations and roll response simulations in regular waves. Of course the underlying algorithm should be validated, before any commercial or scientific use. In this thesis, roll damping will be estimated by performing virtual forced oscillation tests, and the computed roll damping coefficients will be presented as a function of roll amplitude. An additional aim is to apply the obtained roll damping coefficients in a potential theory algorithm.

1.2. Thesis goals and research questions

Roll damping depends on the characteristics of the submerged area of a floating structure (e.g. shape, volume etc.), and additionally on the nature of the examined fluid (which is assumed to be water in all cases considered here). Moreover, it strongly depends on the two main characteristics of the motion: the amplitude and the frequency of the oscillation. Indirectly, roll damping also depends on the natural frequency of the floating structure (the barge in our case). When the frequency of the oscillation coincides with the natural frequency, there is a connection between the natural frequency and the roll damping (as the roll damping depends on the frequency of the oscillation and the frequency of the oscillation is equal to the natural frequency). This connection is important, because the response of the structure to the natural frequency determines the al-

lowable workability.

Moreover, roll damping is highly dependent on viscous effects, vorticity and turbulence of the flow. However, potential-flow models are not able to capture these phenomena (and thus some components of the roll damping), as they assume an inviscid and irrotational flow. For this reason, the open source, CFD (Computational Fluid Dynamics) software, OpenFOAM is used, which solves the incompressible turbulent Navier-Stokes equations, and thus, it can predict the complicated viscous flow around the floating structure accurately.

The main goal of this thesis is the numerical determination of the roll damping characteristics, of a two dimensional barge, using viscous flow simulations, for different drafts, amplitudes and oscillation frequencies. In order to achieve the final goal, OpenFOAM has to be validated with experimental data and data from other simulations. Finally, the influence of many aspects of the flow model has to be investigated. Some of these are turbulence modelling, discretisation in space and time, boundary (and initial) conditions, influence of the amplitude, frequency of oscillation, draft on the nonlinearity, and magnitude of damping.

1.3. Document Structure

In the first chapter, the examined literature and a description of the roll motion are introduced, in order to provide a better understanding of the examined problem. The second chapter describes the basic principles of the roll motion. The third chapter presents the governing equations, which describe the physics of the investigated subject and the mathematical background. Moreover, in the fourth chapter the used methodology and the verification-validation study of Ikeda's case are presented. In the next chapter, the damping coefficients of a full-scale barge, for a number of different amplitudes, frequencies and drafts, are determined and discussed. Lastly, the final chapter presents the conclusions of this thesis and recommendations for future research and development.

2

Current state-of-the-art in experimental and numerical determination of roll-damping characteristics.

In this chapter, the reviewed literature is described. The literature study aims to provide the required knowledge, in order to better understand the physical and numerical problem and finally provide a solution. During the literature study, lots of methods and techniques are analysed in order to conclude to the chosen approach. For a more efficient categorization, the methods and techniques, for the roll damping estimation, were summed up into several groups.

2.1. Physics of roll motion

Each floating body has six degrees of freedom. More specifically, based on the reference system of Figure 2.1 it has:

- three translations of the center of gravity (CoG) in x, y and z direction:
  -surge in the longitudinal x-direction, positive forwards
  -sway in the lateral y-direction, positive to port side
  -heave in the vertical z-direction, positive upwards

- three rotations about the x, y and z axis:
  -roll about the x-axis, positive right turning
  -pitch about the y-axis, positive right turning
  -yaw about the z-axis, positive right turning

In Figure 2.1, roll motion is defined as rotation ϕ of the structure around the x_b axis. In reality the roll axis of a ship is a non-stationary axis parallel to the x_b axis, which is influenced by the center of rotation and center of gravity.

During the roll motion, the structure interacts with the water and this generates normal (pressure) and tangential stresses on the surface of the structure. This results in a hydrodynamic force (and moment), which can be divided in two main parts: the pressure force F_p and the frictional force F_f, as depicted in Figure 2.2.

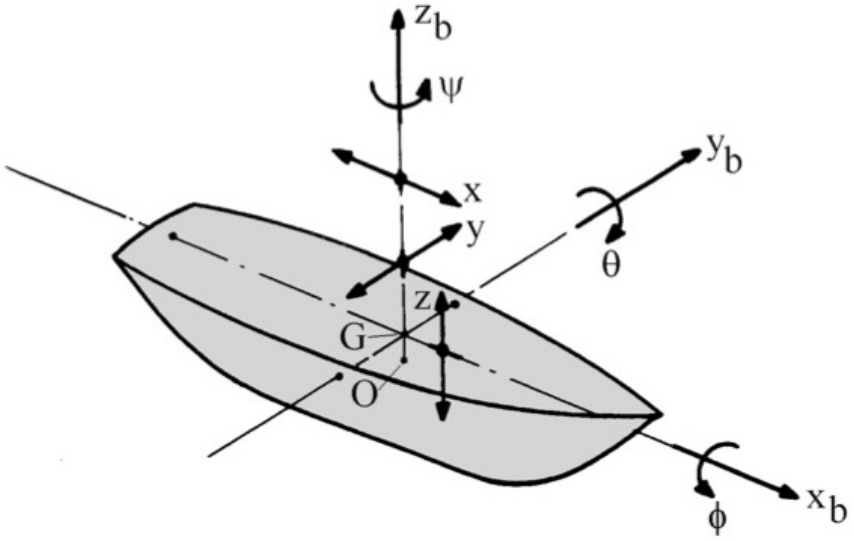

Figure 2.1: Definition of the six degrees of freedom of ship motion

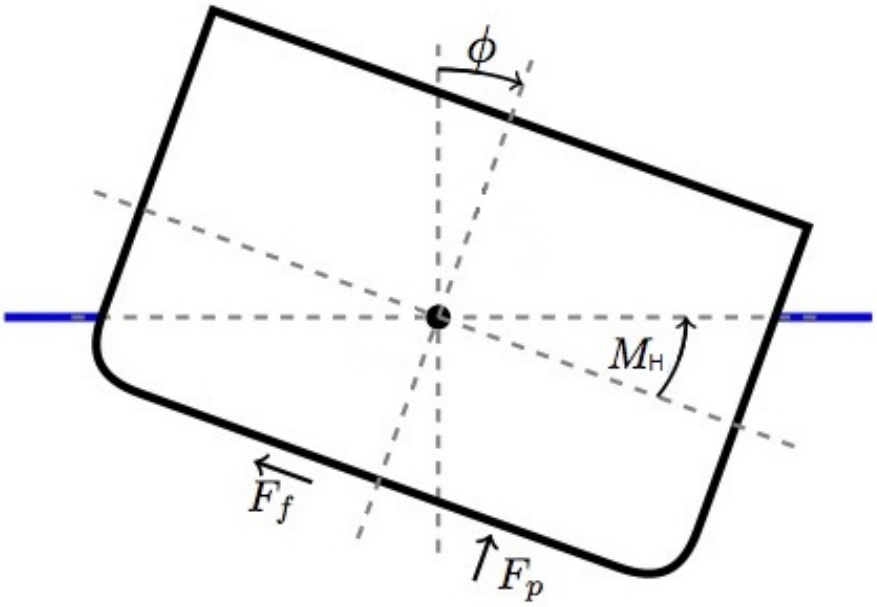

Figure 2.2: Hydrodynamic forces acting on a rolling hull

Based on the described reasoning, the total hydrodynamic force can be calculated by pressure and stress integration and thus the total moment can be determined by multiplying each force component with the respective lever arm, as it is shown in equation 2.1:

$$M_H = \int_S \mathbf{r} \times \left(-pI + \overline{\overline{\tau}}\right) \hat{\mathbf{n}} dS \tag{2.1}$$

Where M_H is the hydrodynamic moment in the direction of the roll axis, $\mathbf{r}$ is the lever arm, p is the hydrodynamic pressure and $\overline{\overline{\tau}}$ stands for the shear stress. Moreover, $\hat{\mathbf{n}}$ is the unit normal vector and S is the surface of the object.

If it is assumed that the floating structure has negligible deformations, then Newton's second law of motion can be used, in order to derive an (rigid body) equation which describes the roll motion of a floating structure, as described below:

$$M_{tot} = I\ddot{\phi} \Rightarrow M_{ext} - M_H = I\ddot{\phi}. \tag{2.2}$$

Where M_{tot} is total moment on the body, M_{ext} represents the external or excitation moment and I is the mass moment of inertia along the axis of roll motion.

As it is decomposed above the M_H describes the total moment due to the water and therefore, it can be expressed as follows:

$$M_H = M_\alpha(\ddot{\phi}) + M_b(\dot{\phi}) + M_c(\phi). \tag{2.3}$$

Where M_α is the added mass moment, M_b represents the added damping moment and M_c is the restoring moment.

With this differential equation, the total hydrodynamic roll moment can be expressed as a superposition of moments, which depend on the rotational acceleration (added mass part), rotational velocity (added damping part) and roll angle (stiffness/ hydrostatic part) respectively. In order to obtain equation 2.3, two main assumptions have been made:
1. The roll motion is uncoupled from the other ship motions
2. There are no cross sectional terms (e.g. dependence on both velocity and acceleration at the same time).

2.2. Sources of estimate roll damping characteristics.

The main sources of roll damping are the creation of waves, skin friction and creation of vortices (eddies), as will be described in Figure 2.3.

Wave damping represents the energy dissipation due to the presence of the free surface. More specifically, waves are generated while a floating structure is performing a roll motion.

Friction damping is caused by the viscosity of the fluid and it happens when the fluid is “sheared” across the surface of the structure. There is a thin layer of water attached to the moving body, which is called the boundary layer. The physics of the boundary layer is explained in section 3.4. This water layer follows the body motion and thus a difference of the water’s velocity close to and away from the structure is created. This results in a large normal derivative of the tangential velocity and a shear stress, which results in frictional drag.

Eddy damping is influenced by the fluid properties and the shape of the structure, and it is caused by the pressure differences along the moving structure. As a floating structure is rolling, high and low pressure regions are created based on the rolling direction. The water always follows “the easiest” path and thus has a direction from the high to the low-pressure areas (opposite to the gradient). When the flow experiences a positive pressure gradient it tends to separate from the surface and create eddies. Apart from a positive pressure gradient, another necessary condition for the creation of eddies is the vorticity of the fluid. These eddies are the source of the eddy (vortex) damping.

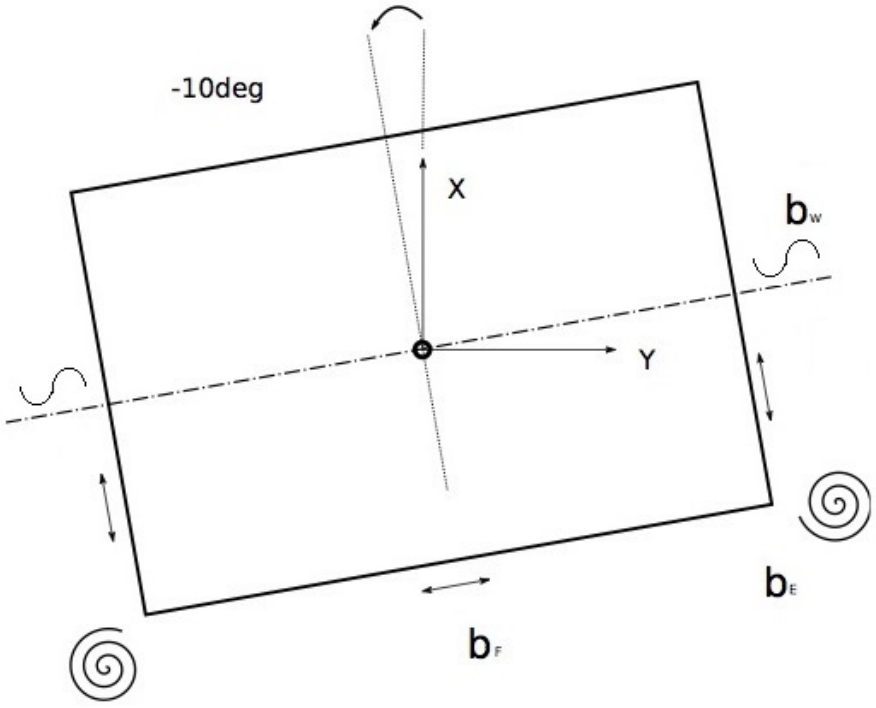

Figure 2.3: Description of the roll damping components

As is widely mentioned in the literature, roll damping is highly non linear. The main source of non-linearity is the creation of vortices at the bilges of the rolling structure. In order to capture this important non-linearity, the fluid properties (such as vorticity, viscous effects and turbulence) should be realistically represented. As a model based on potential theory is not capable of capturing such complicated phenomena, viscous flow simulations can play an important role in the prediction of complex fluid behaviour around the appendages of the structure and thus accurately simulate viscous damping.

2.3. Approaches to estimate roll damping

The methods to estimate the roll damping are divided into three main categories. These three categories are:

- The use of empirical models,
- Extract data from model tests,
- Extract data from viscous flow simulations.

Using experimental data or simulations for the determination of the roll damping characteristics, are based on the same approaches, as both techniques generate a time signal for the moment, and extract the roll damping from this. The main differences will be discussed below.

2.3.1. Determination of the damping coefficients using empirical relations

As mentioned above, roll damping was and still is really difficult to predict, due to the fact that it is highly dependent on viscous effects. For this reason, fifty years ago, when the simulation of viscous flow was not feasible and model-tests already expensive, engineers and scientists tried to predict roll damping with empirical and semi-empirical formulas, based on statistical analysis of model tests and experience. Ikeda's et al [27] empirical method is one of the most famous ways to estimate roll damping. Ikeda and his team published many papers, in which they presented the most widely accepted empirical technique until now. According to this technique, the linearised roll damping is separated into several components and the interaction between the components is ignored. These components can be described by equation 2.4.

$$b_{tot}(\dot{\phi}) = b_W + b_F + b_E + b_L + b_{BK}. \tag{2.4}$$

Where b_{tot} is the total roll damping, and b_w, b_F, b_E, b_L and b_{BK} are the wave, frictional, eddy, lift and bilge keel components respectively.

Each component is described by separate empirical relations. For further information, the reader is referred to [23, 30]. As expected, Ikeda applied many corrections and adjustments since his first publication in order to improve the accuracy of his empirical prediction formulas. An example is [27].

Moreover, Professor Yoji Himeno, who collaborated with Ikeda [23], published in 1981 one of the most useful papers to date. In his paper he summarizes Ikeda's "separation" method and describes other classic ways to model roll damping. As already mentioned roll damping is highly nonlinear and can be described in the following way:

$$M_b(\dot{\phi}) = b_1\dot{\phi} + b_2\dot{\phi}|\dot{\phi}| + b_3\dot{\phi}^3 + ..., \tag{2.5}$$

where b_1, b_2, b_3 are the coefficients of the non-linear representation of the roll damping.

The coefficients b_1, b_2, b_3 etc., are considered constant during a steady periodic oscillation (harmonically excited or forced roll motion and motion under regular waves) and fully dependant on the frequency and amplitude of the oscillation (ω, ϕ_α). The damping coefficients also depend on the natural frequency (indirectly), because at the peak of the RAO (resonance frequency area) the oscillation frequency is equal to the natural frequency.

Because it is really difficult to use and analyse a nonlinear equation, Himeno [23] introduced a linearisation, which has the following form:

$$M_b(\dot{\phi}) = b_{eq}\dot{\phi}, \tag{2.6}$$

where b_{eq}, is equivalent linearised roll damping.

This approach is used further in the thesis, in order to extract the equivalent linearised roll damping.

2.3.2. Experimental determination of damping coefficients

Following Wassemann et al [60], there are three main (experimental) ways to estimate the roll damping of a floating structure. These three techniques are:

- The roll decay test
- The harmonically excited roll motion experiment
- The harmonically forced roll motion experiment

For each technique, there are many sub-techniques to calculate the roll damping coefficient. These sub-techniques will be described in section 2.4. It is important to mention that experimental determination of the roll damping coefficient is a widely accepted technique, as it has been validated extensively. However, this method has two main drawbacks: inflexibility and potentially high errors due to scale effects. The first means that it is too difficult to represent the true physical conditions at a basin (laboratory) and the second that the errors due to Reynolds or Froude scaling can be really high. (As it is well known, it is practically impossible to apply Reynolds and Froude scaling at the same time – or not.)

2.3.3. Determination of roll damping coefficients using viscous-flow simulations

As computational power increases, the use of numerical simulations becomes more widespread in the field of floating structure hydrodynamics. The reason for this is a combination of three main characteristics: low cost, accurate results and flexibility. Moreover, in viscous flow simulations, it is possible to apply both Reynolds

and Froude scaling at the same time, because all variables and physical properties (e.g. viscosity of the fluid) can be controlled [34]. In a real model test, this is unfeasible.

However, the set-up of a viscous-flow simulation can be really challenging, as it is highly sensitive to the selection of the numerical schemes and turbulence models. Additionally, a special and temporal verification is required, in order to ensure the reliability of the model. Finally, the viscous-flow algorithms should be validated, by comparing the numerical results with experimental data.

The challenges mentioned above make the determination of the non-linear roll damping by means of viscous-flow simulations a research topic and for this reason many institutions and companies still investigate this subject. In 2014 a JIP (Joint Industry Project) was formed in order to research the non-linear roll damping of an FPSO, by performing roll forced oscillation experiments and viscous-flow simulations.

The techniques for extracting the roll damping characteristics from viscous-flow simulations are more or less the same as those used with experimental data. However, there are some cases where roll damping has been calculated in a unique way. One example is the paper of Korpus et al. [42], where he calculated the roll damping components (wave, friction, eddy) separately. Firstly, he separately calculated the wave damping, using a diffraction model. Then, he assumed that the wetted part of the floating body is fully submerged (neglecting the free surface and waves) and performed a numerical forced oscillation test. It is important to mention that the submerged wetted surface is mirrored in order to avoid vortex interaction between the top and the bottom parts. Finally, he separately calculated the friction and the eddy damping, by integrating the shear stresses and the normal pressures at the wetted surfaces respectively. The total damping was determined as a superposition of all roll-damping components (wave, friction and eddy).

Jaouen et al. [33, 34] used a similar approach for the determination of roll damping. They compared their numerical results with experimental data of Ikeda, and a very good agreement was found, with deviations lower than 10%.

The solution, which was performed, by Korpus et al. and Jaouen et al. [33, 42] is not exact as the roll damping components are neither independent nor additive. However, this engineering approach provides reliable and fast results.

2.4. Classic procedures to compute roll damping

As mentioned before, there are several techniques to estimate roll damping. Most of these techniques are used in combination with most of the described methods (experimental and viscous flow simulations) for the estimation of roll damping. The most important techniques are described below.

2.4.1. Roll decay

In the roll decay technique, the floating body (barge, vessel etc.) is initially positioned at a specific roll angle, and then released. The roll angle is monitored until all energy dissipates. It is one of the simplest ways to estimate roll damping and at the same time it is powerful, as it gives information for various amplitudes with only one excitation. Moreover the oscillation frequency is equal to the natural frequency of the structure and for this reason the decay method automatically captures the roll damping at the natural frequency. This is of great importance, as the correct determination of roll damping at the natural frequency (resonance), provides a trustworthy RAO at this frequency area.

The ways to extract the roll damping coefficient from a decay test are based mainly on logarithmic roll decrement and on energy conservation (Wassemann et al. [21, 60], which give a linearised form of the roll damping coefficient.

The main drawback of this technique is the fact that the roll amplitudes cannot be controlled (except for the initial inclination). Additionally, the roll damping is influenced by the prior roll motion of the floating

structure, as the water particles are affected by the roll amplitudes and the roll periods of the previous cycles. This phenomenon is known, as the “memory effect” of the water. More specifically, decay tests with different excitations may result in differences up to 25% for the quadratic damping part, (Van't Veer and Fathi [55]). In some cases, numerical (CFD) and experimental decay results are compared for the validation of the CFD code. Some useful examples are [66, 69].

2.4.2. Harmonically excited and forced roll motion

The harmonically excited and forced roll motion techniques are similar ways to determine roll damping. In both cases the oscillation is periodic (response). In the former case, the angle of rotation (usually simple sinusoidal) is controlled, while in the latter the external-excitation force is imposed (again usually sinusoidal). The great advantage of these two methods is that they completely control the amplitude and the frequency of the motion and excitation force respectively. Additionally, the harmonically excited roll motion is independent of the resonance phenomenon. To be more specific, resonance cannot exist (even at the resonance frequency), as the motion is completely controlled. Moreover, in this case the roll damping is independent of the memory effect as the coefficient is extracted when the hydrodynamic moment has reached a steady state and periodic form. In this thesis, the harmonically excited roll motion is used. In the paper of Wassemann et al. [60] three different extraction methods, which are based on the concept of conservation of energy, are mentioned.

There are a lot of publications where the results from simulations of harmonically excited roll motion are compared with experimental data for validation purposes. Important examples are, Bonfiglio et al. [5], Yidiz et al. [68] and Jaouen et al. [34].

2.4.3. Determination of roll damping coefficients in regular waves

In some cases, roll-response tests under regular waves are performed, for the estimation of roll damping. Although there are a lot of restrictions and difficulties in order to perform this kind of experiments, this technique is more realistic due to response under waves. For this reason, roll response simulations in regular (and irregular) waves have become popular, as they are fast, efficient and relatively accurate. However, before any commercial or scientific use, validation of such models should be performed. The paper of Mohsin A.R et al. [29] is a good example of this validation procedure.

3

Governing Equations and Numerical Model – Theoretical background

3.1. Navier-Stokes equations

The viscous-flow algorithm is solving the conservative form of the incompressible Navier-Stokes equations, with variable density and viscosity , which are presented below.

$$\frac{\partial u_i}{\partial x_i} = 0, \tag{3.1}$$

$$\frac{\partial \rho u_i}{\partial t} + \frac{\partial \rho u_i u_j}{\partial x_j} = -\frac{\partial p}{\partial x_i} + \frac{\partial}{\partial x_j}\left[\mu\left(\frac{\partial u_i}{\partial x_j} + \frac{\partial u_j}{\partial x_i}\right)\right] + \rho g_i. \tag{3.2}$$

Where u is the velocity vector of the flow, μ is the dynamic viscosity, ρ is the density and g is the gravitational acceleration.

In addition, the following equations are generated, in order to avoid resolving the turbulent flow on the smallest length and time scales, by applying the averaging technic of Reynolds (Appendix A.1) on the Navier-Stokes equations.

$$\frac{\partial U_i}{\partial x_i} = 0, \tag{3.3}$$

$$\frac{\partial \rho U_i}{\partial t} + \frac{\partial \rho U_i U_j}{\partial x_j} = -\frac{\partial p}{\partial x_i} + \frac{\partial}{\partial x_j}\left[\mu\left(\frac{\partial U_i}{\partial x_j} + \frac{\partial U_j}{\partial x_i}\right) - \rho u_i' u_j'\right] + \rho g_i. \tag{3.4}$$

Where U is the average velocity and the extra term represents the Reynolds (turbulent) stress tensor. The influence of the velocity variations on the mean flow is described by turbulence models, some of which are illustrated in section 3.2.

Even though, the conservative form of the Navier-Stokes equations are used, it is speculated that in multiphase flows the non-conservative form perform better, as it is described by Henrik Rusche [52] and Tryggvason et al. [54].

3.2. Turbulence models

The examined turbulence models belong to the RANS (Reynolds-Averaged Navier-Stokes) family. When the Reynolds-Averaged technique is applied to the Navier-Stokes equations (equations 3.3 and 3.4) the system of equations cannot be solved directly, as the number unknowns exceed the number of equations. This means that the RANS turbulence models are created in order to close the system of equations and give expressions for the Reynolds stresses (extra term in equation 3.4).

From the perspective of hydrodynamics, roll damping depends on flow separation and vortex creation. Moreover, turbulence plays an important role in order to capture these two phenomena accurately, and thus

turbulence modelling is essential for the roll damping determination. For this reason, in order to find a suitable model for the examined case, $k-\varepsilon$ Realizable, $k-\omega$ SST and $kkl-\omega$ turbulence models are used, and compared with each other. A brief description of the used turbulence models follows.

$\underline{k-\varepsilon}$

$k-\varepsilon$ Realizable is a modification of the standard k-epsilon model and has three main differences from the original version.
1. It has another formulation for the eddy viscosity (the mean rate-of-rotation tensor is included in the eddy viscosity equation).
2. It has a new formulation for the dissipation rate (ε), which derives from the transport equation of the mean-square vorticity fluctuations.

Due to these reasons, the $k-\varepsilon$ realizable model performs better for flows involving rotation, boundary layers under strong adverse pressure gradients, separation and recirculation. The term realizable means that the model satisfies certain constrains about the Reynolds stresses.

More information about the $k-\varepsilon$ Realizable model can be found in [14].

$\underline{k-\omega \text{ SST}}$

The $k-\omega$ SST model belongs to the family of RANS turbulence models. This two-equation model combines the positive characteristics of the simple $k-\omega$ and $k-\varepsilon$ models. Specifically, the $k-\omega$ SST model is equivalent to the $k-\omega$ model in the inner part of the boundary layer. This means that it is valid all the way down to the wall (through the viscous sub-layer), and for this reason, no wall functions (approximations close to the wall) are required. In addition, the $k-\omega$ SST model behaves as the $k-\varepsilon$ model outside the boundary layer and thereby partially overcomes the sensitivity of the $k-\omega$ model to the inlet free-stream boundary conditions. Finally, it is known for its good performance in adverse pressure gradients and separating flows.

For more information someone can refer to the book of Dr. Wilcox [64].

$\underline{kkl-\omega}$

The $kkl-\omega$ is a RANS based turbulence model, which is suitable for modeling transitional flows and low-Reynolds number turbulent flow cases. This three-equation model is based on the low Reynolds $k-\omega$ model, with an additional equation for laminar kinetic energy. Moreover, it has the advantage that the dependence of the solution on the initial and boundary conditions for the turbulent quantities is limited. Finally, this turbulence model is very accurate in cases of an adverse pressure gradient.

For a more elaborate discussion of the $kkl-\omega$ model the reader is referred to J.Furst's publication [18].

3.3. Volume of Fluid (VOF) method

The Volume of Fluid (VoF) method is used to describe the evolution of the free surface. This method is based on a Eulerian formulation. The VoF method describes the interface of a two-phase flow using an advection equation (equation 3.8) and this equation should be solved in combination with the incompressible Navier-Stokes equations, in order to capture the free surface. More specifically, the density and viscosity in the Navier-Stokes equations vary based on the phase flow.

The VoF method is based on the scalar volume fraction (α) and describes the percentage of each fluid in each cell and thus the phase of the flow. In our case the two fluids are water and air. When a cell is filled with water the α value is equal to 1, while when it is filled with air α is equal to 0. The surface is described by a one-cell layer, in which the value of α is between 0 and 1. This means that the free surface is not defined sharply, but it is distributed over the height of one cell. For this reason, the mesh at the free surface should be fine enough. However, the discretised form of α is a discontinuous function as its value jumps from 0 to 1

(in cases where the "surface" cells have a really small or really big α values). Moreover, it is assumed, that the fluids are immiscible (cannot exchange mass and heat). Finally, the surface tension (elastic tendency of the fluid surface, caused by the cohesive forces among liquid molecules) can be additionally included. The importance of the surface tension forces compared to the gravitational forces, can be determined by the Eotvos number:

$$E_o = \frac{\Delta\rho g L^2}{\sigma}, \tag{3.5}$$

$\Delta\rho$:difference in density of the two phases (in the examined case is $1000 kg/m^2$),
g: gravitational acceleration,
σ: surface tension (for air in contact with water is equal to approximately $0.07 N/m$),
L: reference length.

When the Eotvos number is high, the surface tension is negligible and vice-versa. Based on numerical experiments (with and without modelling the surface tension forces) and on Eotvos number, it can be concluded that the surface tension effects are insignificant and for this reason are neglected.

Navier-Stokes and advection equation of α, are connected through density and viscosity. Density and viscosity of a cell, which contains both fluids (in our case water and air), can be represented as follows:

$$\rho(x,t) = \rho_{water}\alpha + \rho_{air}(1-\alpha), \tag{3.6}$$

$$\mu(x,t) = \mu_{water}\alpha + \mu_{air}(1-\alpha). \tag{3.7}$$

Where $\rho_{water}, \mu_{water}, \rho_{air}$ and μ_{air} are the density and dynamic viscosity of water and air respectively. Figure 3.1 describes the density and viscosity based on the varying volume fraction. It can be seen that at the interface the density and the viscosity is nor of water, nor of air and the values of these variables are determined by equations 3.6 and 3.7 respectively.

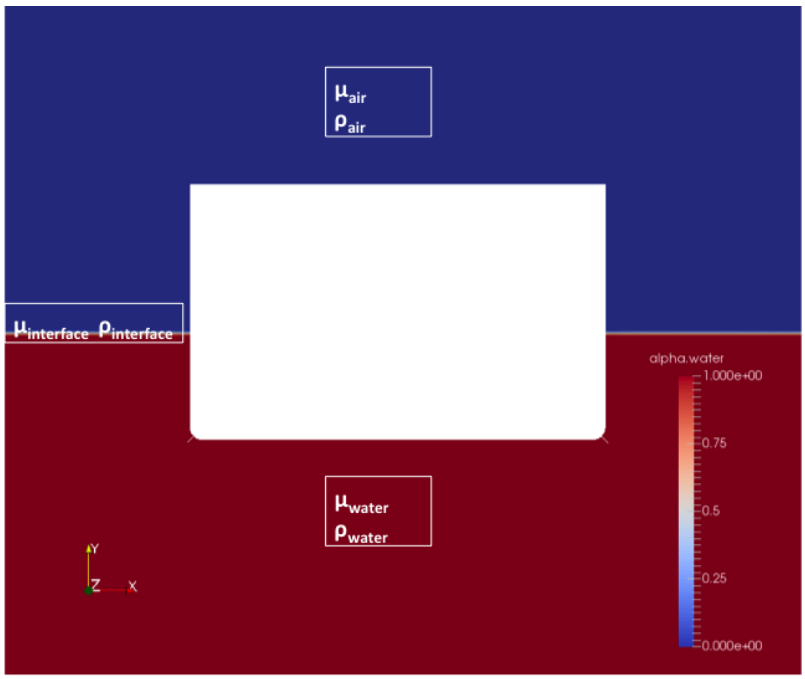

Figure 3.1: Density and viscosity based on the varying volume fraction

After solving the Navier-Stokes equations (at each time step), determination of α is done by solving an advection equation (transport equation because α is a scalar). The differential form of this equation therefore becomes:

$$\frac{\partial \alpha_q}{\partial t} + U_i \frac{\partial \alpha_q}{\partial x_i} = 0, \tag{3.8}$$

Where α_q is the volume fraction of the phase q.

3.4. Boundary layer – Wall treatment

Within the boundary layer three different layers can be distinguished, lowed on y^+. The distinction between the different layers is done based on the y^+ (dimensionless distance) value. The y^+ can be calculated by the following formula:

$$y^+ = \frac{\rho u^* \Delta y}{\mu}, \tag{3.9}$$

Where u^* is the friction velocity and is defined as: $u^* = \sqrt{\frac{\tau_w}{\rho}}$. Moreover, τ_w is the wall shear stress and Δy represents the distance from the examined boundary (wall).

Specifically:
For $y^+ < 5$: Viscous sub-layer
For $5 < y^+ < 30$: Buffer layer
For $30 < y^+ < 300$: Log-law layer
For $300 < y^+$: Outer region – Free stream flow

Figure 3.4 describes in detail the previous description.

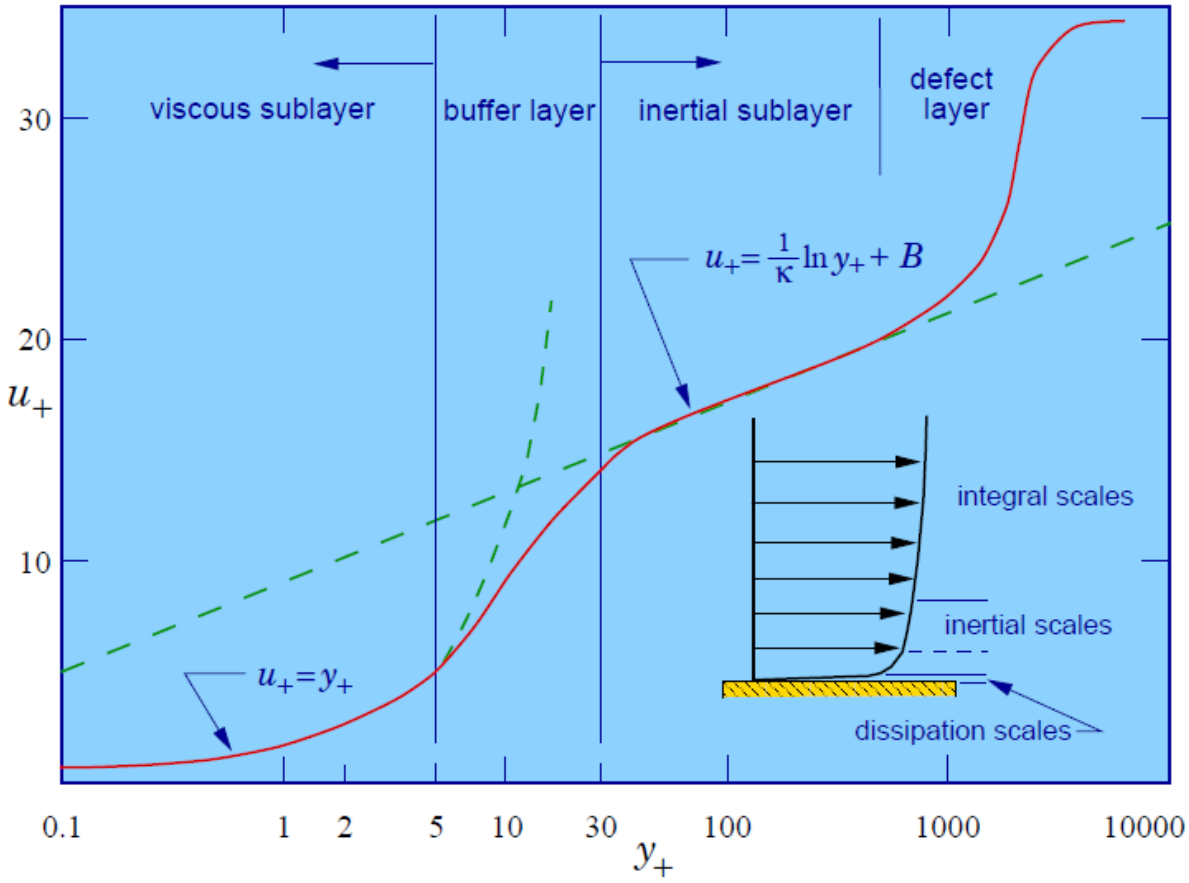

Figure 3.2: Description of the turbulent boundary layer

Wall functions

Based on y^+ formulation some $k-\varepsilon$ and $k-\omega$ models are using wall-functions for near wall treatment. Wall functions are used, because it is not practical to refine the turbulent boundary layer, in order to resolve

the viscous sub-layer, because this could lead to an enormous number of small sized cells and thus to extremely small time-step (based on Courant number). Wall functions aim to describe μ_{total} at the nodes on and near the walls, based on the law of the wall. In order to do so, it is assumed that:
$\Rightarrow$ The closest node to the wall is positioned at the inertia sub-layer (log-law region, $300 > y^+ > 30$).
$\Rightarrow$ The wall shear stress should be modelled (predicted), based on the value of the mean velocity, of the closest node.

It is important to mention that some turbulence models are compatible only with wall functions ($k-\varepsilon$ Realizable) and some others without ones ($kkl-\omega$). There are some exceptional models, which can use both approaches ($k-\omega$ SST). When Reynolds number is low (lower than 10^5) and flow separation happens, it is much more accurate to resolve the boundary layer in order to avoid the use of wall functions and approximations of the velocity profile in the boundary layer. In cases where no wall functions are used, the y^+ value should be lower than 1 (one). However, this refinement makes computations more time consuming and sensitive. In some cases using wall functions is unavoidable (e.g. simulations at full scale with high Reynolds number).

3.5. Boundary and initial conditions

A boundary value problem should be defined, in order to predict the motion of a fluid. Specifically, a boundary value problem is composed by a set of differential equations together with some additional constrains, which are called boundary conditions. In this section necessary boundary and initial conditions are formulated for the incompressible NS equations and the interface model.

3.5.1. Boundary conditions

The boundary condition for velocity at structure walls, is a "no slip" (Dirichlet) condition, which means that the relative velocity at the wall is constant and specifically in our case zero (both tangential and normal components). However, the wall velocity of the structure is not fixed (as the structure is oscillating) and thus a special moving no slip condition is applied (water velocity is equal to the wall velocity). Finally, for the pressure, a special Neumann condition for moving walls is used. This choice was made based on the velocity boundary condition.

For cases in which the free surface is present, a slip condition is applied for the bottom, left, and right walls, which means that only the normal component of the velocity is zero and that the tangential component of the fluid has no interaction with the wall. This boundary condition is chosen, instead of a no slip condition, because the mesh resolution close to the side and bottom boundaries of the domain is not sufficient in order to capture correctly the turbulent effects, as the y^+ requirements are not fulfilled. Thus, it is preferred to neglect the tangential component of the velocity, as it is one of the main sources of turbulent effects close to a wall. Based on the velocity boundary condition, a Neumann condition is chosen for the pressure at the wall boundary. For the top wall, a non-reflective boundary condition is selected in order to realistically represent the far field atmosphere.

When the structure is assumed to be fully submerged, the far field is chosen to be an outlet boundary. For this reason the velocity boundary condition is chosen to be a combination of Neumann and Dirichlet conditions (inlet, outlet). Specifically, if the velocity vector at the outlet points out of the domain, then the boundary condition will be of the Neumann type, while if the velocity vector points into the domain, the boundary becomes Dirichlet, which means constant. For pressure a zero Dirichlet boundary condition is selected which means that pressure at the far field boundaries is constantly zero.

It is important to mention that regarding pressure there are no actual boundary conditions but the pressure conditions at the boundaries are an outcome of the velocity boundary conditions in combination with Navier -Stokes equations. However, in OpenFOAM it is compulsory to specify both initial and boundary conditions for the pressure field in accordance with the velocity field and Navier-Stokes equations.

The phase fraction alpha also requires boundary conditions. For this dimensionless parameter a Neu-

mann boundary condition is selected, and more specifically the value of the normal gradient at the boundary is set to zero. This means that the alpha value at the boundary is equal to the value of the first cell adjacent to the boundary.

Additionally, boundary conditions at the walls for the turbulent quantities should be specified. If the turbulence model is for a high Reynolds number (e.g. $k-\varepsilon$ Realizable) then wall-function boundary conditions are used, which means that the turbulent quantities at the boundaries are approximated based on a specified velocity profile (chapter 3.4). On the other hand, for low Reynolds number flows, the boundary layer is resolved straight down to the boundary and there is no need for wall functions. However, even in this case, special boundary conditions may be necessary (e.g. calculation of the turbulent viscosity).

More information about the implemented boundary conditions in OpenFOAM, are included in Appendix B.1.

3.5.2. Initial conditions

The initial (internal) conditions for the velocity and pressure fields are zero as the simulation starts from rest. The initial condition for the volume fraction (α) is determined based on the free surface level at the beginning of the simulation. Finally, initial conditions for turbulent quantities, such as k, ω and ε, are specified based on empirical and semi-empirical formulas [64]. The importance of the last one is examined in subsection 4.1.1.

3.6. Relaxation zones – Non-reflective zones

The open-source wave generation and absorption toolbox wave2foam, developed by Jacobsen et al. [31, 32], is used in order to generate non-reflective areas, known as relaxation zones, at the far field and thus avoid wave reflection. By using this approach the size of the computational domain can be decreased and thus the computational time can be reduced.

As the relaxation zones, the velocity field (u) and the volume fraction (α), are updated explicitly every time step based on the following function:

$$\psi = a_R \psi_{com} + (1 - a_R)\psi_{target}, \tag{3.10}$$

where ψ represents the velocity or the volume fraction, ψ_{target} defines the target value, which is calculated using the applied wave theory (in the examined cases, uniform current with zero velocity), and ψ_{com} illustrates the numerically computed values based on Navier-Stokes and VOF equations. α_R is the weighting factor for the two solutions and it is calculated as follows:

$$a_R(\chi_R) = 1 - \frac{exp(\chi_R^{3.5}) - 1}{exp(1) - 1}, \tag{3.11}$$

χ_R represents local co-ordinate system for the relaxation zone and takes values between 0 and 1. It is important to mention, that the weighting factor α_R takes higher values close to the boundary and vice versa. Therefore, the boundary condition at the wall, is specified by the target value (ψ_{target}) and it is not affected by the computational domain. Figure 3.3 represents the relaxation zones:

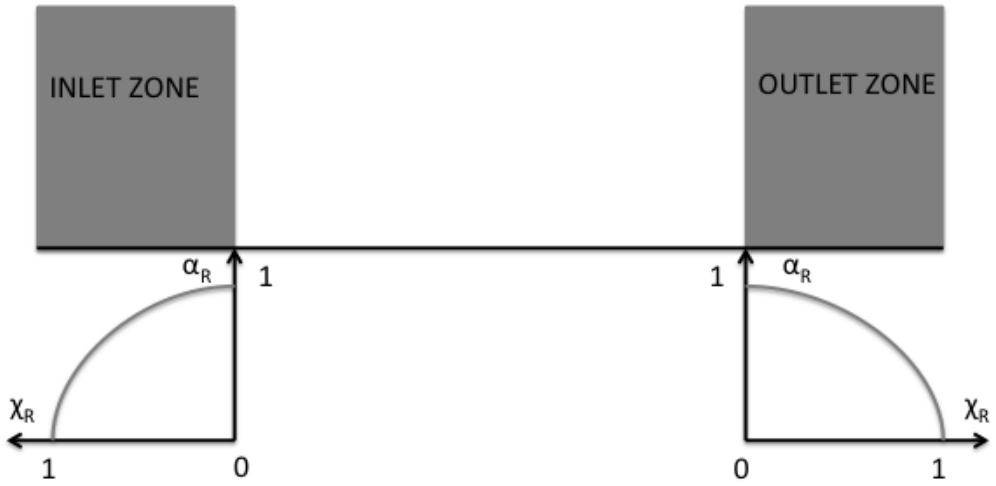

Figure 3.3: Relaxation zones and variation of α_R and χ_R

For further explanation someone can refer to [31, 32].

3.7. Numerical schemes - Discretization methods

Another important aspect in Computational Fluid Dynamics is the selection of the discretisation schemes in space and time. A low order scheme may reduce the accuracy or require high resolution of the discretisation in space and time. However, a high order scheme may be less robust. For this reason the numerical schemes should be selected in a way in which a compromise between accuracy and tolerance can be achieved. In the examined cases, the described balance is accomplished, since the numerical schemes are carefully chosen.

The time derivative is discretised with the first order, implicit, Euler backward scheme. As the accuracy of the time discretisation is of high importance, the second order Crank-Nicolson method was tested for the discretisation of time derivative of velocity. However, the above method led to high instability (especially in cases with free surface) and for this reason was rejected.

The discretisation of the convective term of the momentum equation (or convection of the velocity) is founded on an unbounded second-order upwind scheme. For a given mesh width, this second order scheme is more accurate than the ordinary upwind scheme. Additionally, it is more robust than the linear scheme, due to the fact that it is bounded. Moreover, the same scheme is used for the discretisation of the convection terms of the turbulent quantities. In addition, it is important to mention, that this discretisation scheme requires the discretisation of the velocity gradient as well.

The second order, limited vanLeer scheme is chosen for the advection of the phase fraction. The limited choice can be justified, as the alpha field (and thus the free surface) is very sensitive. Finally, a second order central scheme (linear) is selected for the diffusive term of the momentum equation (divergence of shear stress), as it is calculated based on the velocity field and thus there are no instability issues.

The discretisation of the gradient operator is used indirectly, as it does not appear precisely in the used solvers. However, it is necessary for the application of the (divergence) linear-upwind scheme, which is mentioned above, and it is applied in the discretisation of the shear stress term. Moreover, it appears in the equations of the turbulent quantities. For the discretisation of the gradient operator, a limited, second-order scheme is selected, which restricts the gradient in such a way that when cell values are extrapolated to faces using the calculated gradient, the faces values do not fall outside the bounds of values in surrounding cells. This improves the stability for moving and deforming meshes.

The surface normal gradient schemes appear both in the momentum equation at the pressure term and in the pressure-correction equation. Moreover, these schemes are required to evaluate a Laplacian term using Gaussian integration. A surface normal gradient is calculated at the cell face. Specifically, it is computed based on the gradients at the centers of the two cells that the face connects, and represents the component normal to the face. It is calculated with a central difference scheme and this provides second-order accuracy in cases where the cells are orthogonal. However, in most of the time this is not the case and especially in these examined cases where the mesh is deformed. For this reason, in order to maintain the second-order accuracy, a scheme which provides a non-orthogonal correction is selected. The orthogonal correction is applied implicitly (by adding) to the non-corrected solution.

Finally, the Laplace operator, which appears in the momentum and pressure-correction equation, is discretised as the surface normal gradient and thus a similar discretisation scheme is selected.

More information about the selected schemes appear in Appendix B.2.

3.8. Solution algorithm

Most solvers for viscous-flow simulations use the pressure-implicit split-operator (PISO), the semi-implicit method for pressure-linked equations (SIMPLE) or a combination of these two, which is referred to as PIMPLE by the OpenFOAM developers. These algorithms are iterative procedures for coupling the momentum and the mass (pressure correction) equations. PISO and PIMPLE are used for transient problems, while SIMPLE has been designed for steady state problems.

In the current application this PIMPLE algorithm is applied. Therefore, the properties of this algorithm are briefly reviewed. A flowchart of the algorithm is given in Figure 3.4. This algorithm has many input parameters, which control the different iterative processes within the solution procedure of the governing equations (momentum and pressure correction equations). The most important parameters are listed and explained below:
$\Rightarrow$ Inner loop (nCorrectors): This parameter sets the number of times, that the algorithm solves the pressure equation and momentum corrector in each time-step.
$\Rightarrow$ Outer loop (nOuterCorrectors): This parameter determines the number of loops over the entire system of equations within one time-step. More specifically, it represents the total number of times the system is solved.

In order to further explain the PIMPLE algorithm, an example is required. The momentum and pressure correction equations can be expressed in a vector form as follows:

$$\frac{\partial \rho u}{\partial t} + \nabla \bullet (\rho u u) + \nabla \bullet R = -\nabla p, \tag{3.12}$$

$$\nabla^2 p = f(u, \nabla p). \tag{3.13}$$

If the Inner loop and Outer loop have value 2, the following steps will be performed:
1. Calculate momentum from pressure of previous time-step (equation 1)
2. Calculate pressure from the calculated momentum (equation 2)
3. Correct velocity
4. Calculate pressure again, with the corrected velocity (because the Inner loop parameter is 2)
5. Recalculate momentum from the new pressure (equation 1)
6. Calculate pressure from the new calculated momentum (equation 2)
7. Correct velocity
8. Calculate pressure again, (because the Inner loop parameter is 2).

It is important to mention that the described loops are the main reason that the solution is truly implicit and thus it is allowed a larger non-dimensional time-step size, i.e. a larger Courant number.

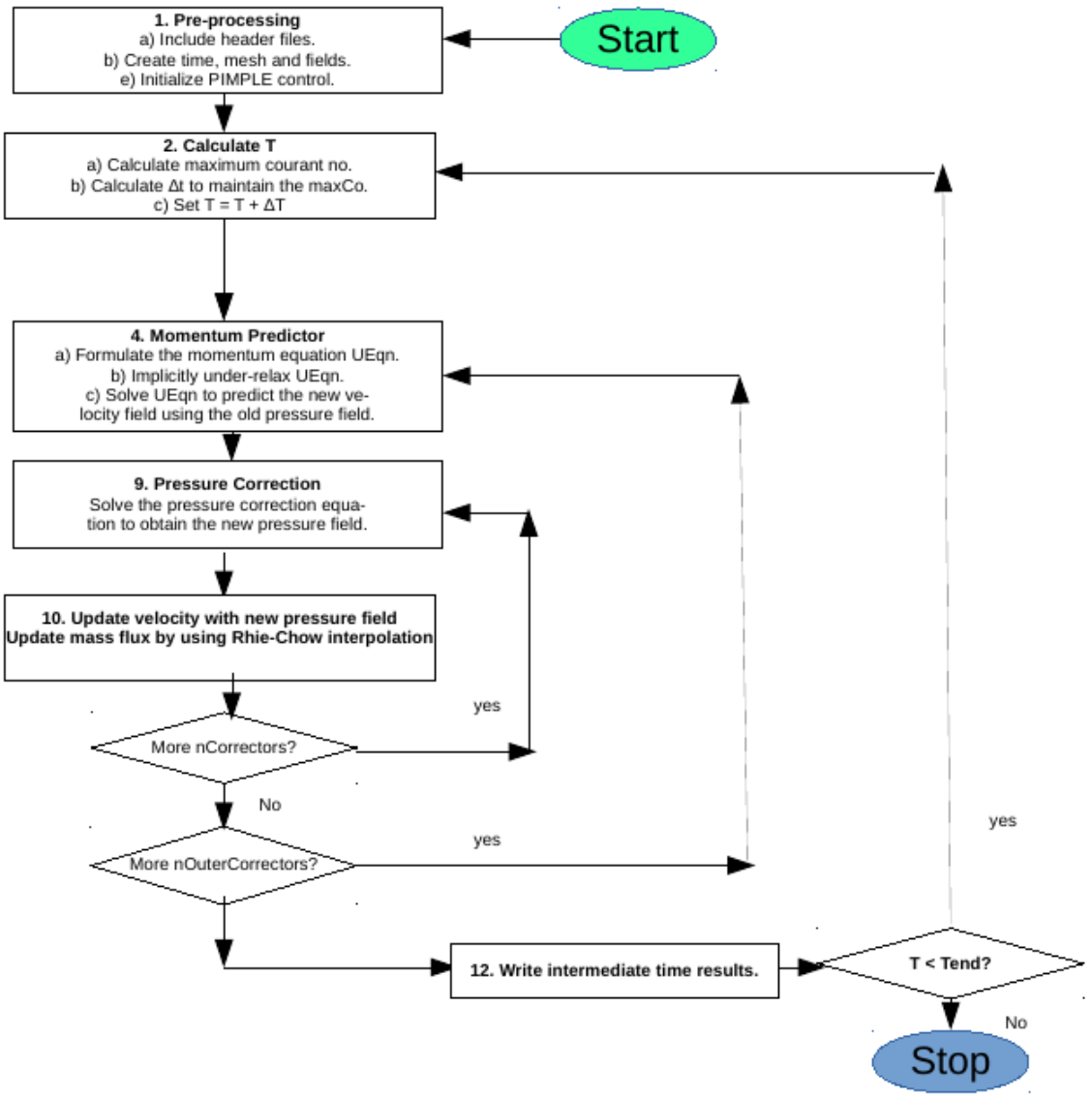

Figure 3.4: Diagrammatic representation of PIMPLE algorithm

3.9. A domain with moving boundaries Methods

In the examined case, forced roll oscillation tests are performed with a viscous-flow algorithm. This means that the boundary of the domain, which represents the hull of the vessel, performs a roll motion around a specified axis.

In viscous-flow algorithms, the motion of a “body” is handled by dynamic mesh functions. There are two ways to apply this motion: deforming mesh and sliding mesh. The definition of these two categories was given very accurately by Professor Hrvoje Jasak [35]: ‘Dynamic mesh handling includes deforming mesh cases, where the number and the connectivity of mesh elements remains unchanged, and topological changes, where mesh size and connectivity varies during the simulation.’

3.9.1. Sliding Mesh

Sliding mesh (or topologically changing mesh) means that the topology of the mesh is changing during the simulation. The chosen cells are moving (changing orientation and position of the cell faces) at each time-

step and they exchange values at the current position. To be more specific, initially a group of cells is specified, and then, this group prescribes a controlled motion, which is specified by the user (e.g. rotational and sinusoidal in this case). Between the inner and outer part of the mesh there are two AMI (Arbitrary Mesh Interface) surfaces, which connect the two parts of the mesh and allow them to exchange values. AMI surfaces are almost identical, meaning that the one should almost coincide with the other. This method has the advantage that allows really high angle rotations as the internal part of the mesh moves together with the solid body and the near wall resolution close to the body remains intact. It is not compulsory for the inner and the outer parts to match (size and number of cells) at the sliding interface (AMI's), but if this is the case the flux is transferred more accurately. Based on this, the user should be aware of conservation errors between moving and static mesh. Figure 3.3 represents the internal mesh (Left), which follows the barge motion and the AMI interface (Right) which is responsible for exchanging the values from the internal (dynamic) mesh to the external (static) mesh.

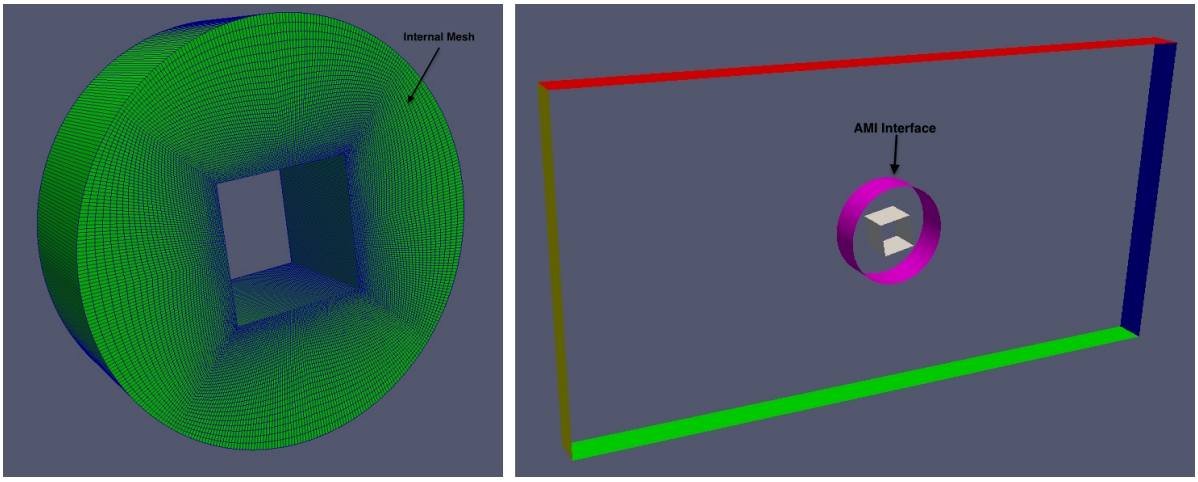

Figure 3.5: Visualization of the internal mesh and AMI interface used for sliding mesh technique

3.9.2. Deforming Mesh

In deforming mesh, the cell shapes change (deform) close to or away from the moving boundaries in order to "handle" the motion. In this case, there are no conservation errors, as there are no sliding interfaces and the connectivity of the mesh elements do not change. For this reason, deforming mesh techniques are easier to implement and are numerically superior. Of course this method is valid when the resolution is not changing significantly during the mesh motion. Moreover, the cell aspect ratio along the moving boundary should be relatively low, as the high aspect ratio cells can be skewed during the deformation.

In order to implement these motions, a relationship between the rate of change of the cell volume (V) and the velocity of the boundary (v_s) should be defined based on the space conservation law:

$$\frac{d}{dt}\int_V dV - \oint_S n \cdot v_s dS = 0, \tag{3.14}$$

A simple and numerically cheap way to ensure space conservation and at the same time minimize the distortion of the control volume is the Laplacian equation with variable diffusivity.

$$\nabla \cdot (\gamma \nabla x) = 0, \tag{3.15}$$

With this pseudo-solid Laplace smoothing equation, mesh deformation displacement (x) is found. In the mentioned equation γ is the diffusivity through which the boundary motion is distributed to the inner grid points. However, Laplacian equation is not suitable for cases where the boundary (solid body) performs a rotational motion (as in the examined cases). In these cases a special rotational motion solver, which uses the solid-body rotation (SBR) stress equation, is selected. Figure 3.6 compares the SBR stress (Left) and the

Laplacian displacement methods (Right), for a rotation motion.

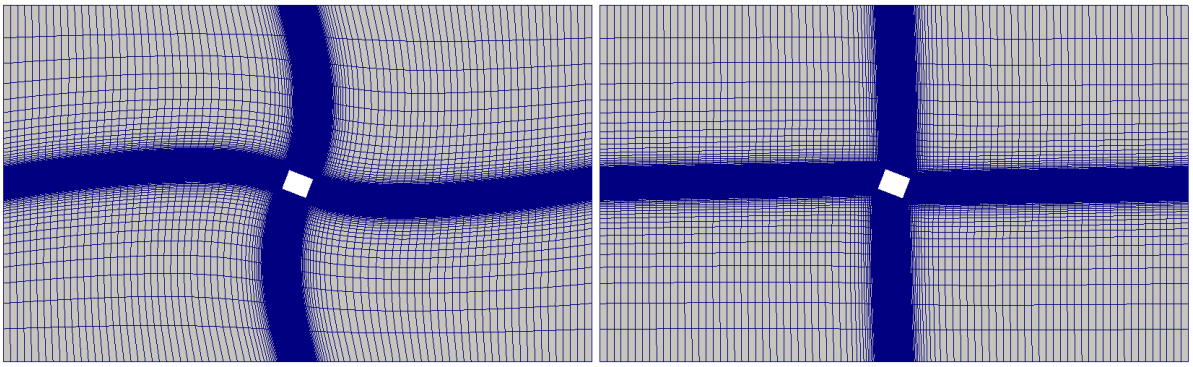

Figure 3.6: Mesh deformation of the outer domain with SBR stress and Laplacian displacement method

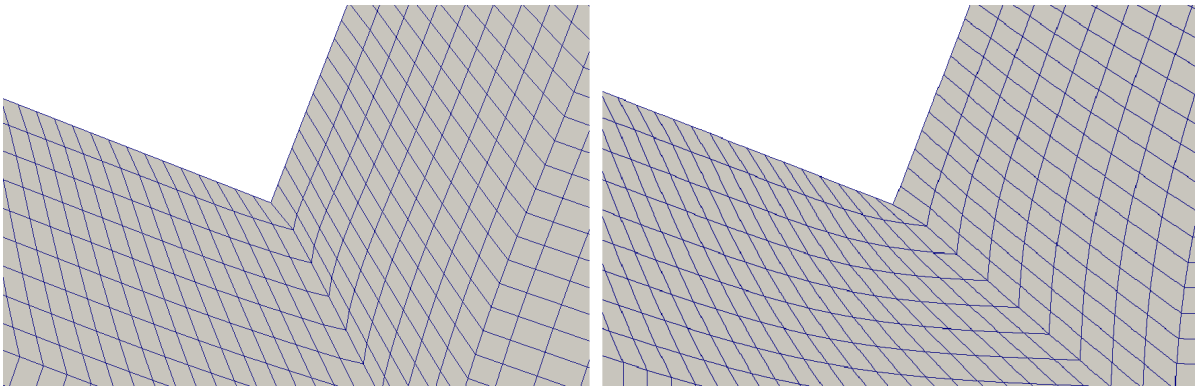

Figure 3.7: Mesh deformation at the vicinity of the bilge with SBR stress and Laplacian displacement method

It can be seen that with the SBR stress method, the mesh deformation is transferred away from the examined boundary, while with the Laplacian method it is not. Moreover, Figure 3.7 shows that this has an impact on the skewness of the cells close to the body. This phenomenon is more intense in more refined meshes and for this reason the SBR stress method is necessary for rotational bodies.

The used viscous-flow algorithm provides different diffusivity models that allow us to solve the cell movement equation. In this case the inverse quadratic diffusivity model is used. Inverse diffusivity means that the diffusivity of the field is based on the inverse of the cell distance from a specified boundary. More specifically:

$$\gamma(l) = \frac{1}{l^m}, \tag{3.16}$$

where l is the cell distance to the nearest moving boundary and m is, in our case, two (quadratic). In particular, this means that the deformation of the mesh based on the body motion, is transferred further away from the boundaries of the body. Figure 3.8 shows the mesh deformation with the SBR stress method and the inverse quadratic diffusivity, at different time instances.

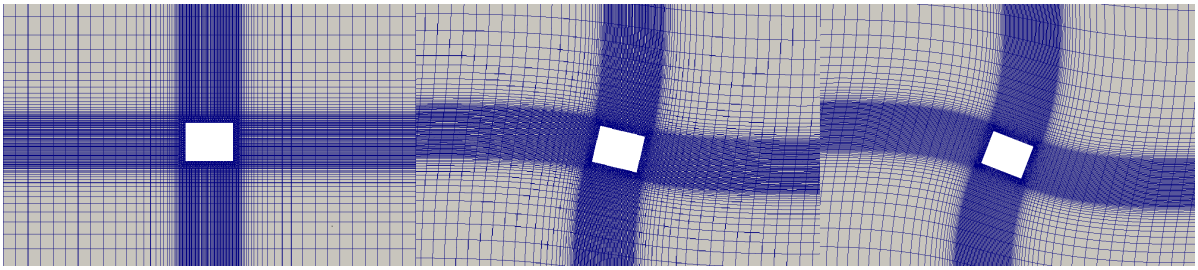

Figure 3.8: Mesh deformation with SBR stress method and inverse quadratic diffusivity

Because in the examined case, boundary layer close to the barge is of high importance (we need low cell deformation in order to achieve high force accuracy), inverse quadratic diffusivity model in combination with SBR stress method is selected.

3.9.3. Deforming vs. Sliding mesh

The mentioned dynamic mesh-handling methods were tested in order to choose the optimum technique for the examined case. Finally, the deforming method was chosen, as high conservation errors resulted from the use of the sliding mesh. On the other hand, the deforming mesh (with the SBR stress method) proved to be robust, even in extreme roll angle cases.

3.10. Damping extraction methods

As mentioned in section 2.1, the equation, which describes the roll motion as a single degree of freedom, can be described by the following equation.

$$M_H = M_\alpha(\ddot{\phi}) + M_b(\dot{\phi}) + M_c(\phi). \tag{3.17}$$

3.10.1. Equivalent linearised roll damping

Based on the literature [23, 27], this equation is non-linear and this non-linearity is expected to appear in the added damping term. The other terms are expected to be approximately linear (for the examined structures). In cases where the first harmonic of the damping force is dominant, it is acceptable to assume that the equation 3.18 has a linear form, as given by:

$$M_H = a\ddot{\phi} + b_{eq}\dot{\phi} + c\phi. \tag{3.18}$$

Where a, b and c are the added mass, equivalent linearised added damping and restoring coefficients respectively.

Taking into account the previous assumption, three different methods were investigated in order to extract the equivalent roll damping. All three of them are presented here.

Harmonic-analysis method

As mentioned in subsection 2.4.2, in a harmonically exited roll motion the roll angle has a sinusoidal form. If this is the case, then it can be assumed that the total reactive moment also has a sinusoidal form:

$$\phi = \phi_\alpha \sin(\omega t) \Rightarrow M_H = M_{H_\alpha} \sin(\omega t + \varepsilon). \tag{3.19}$$

Where ϕ_α and ω is the amplitude and frequency of the sinusoidal roll motion respectively, M_{H_α} is the amplitude of the hydrodynamic force and ε indicates the phase angle between the prescribed roll motion and the hydrodynamic moment. Substitution of equation 3.19 to equation 3.18 gives the following relation:

$$-\omega^2\phi_\alpha a\sin(\omega t) + \omega\phi_\alpha b_{eq}\cos(\omega t) + \phi_\alpha c\sin(\omega t) = M_{H_\alpha}\sin(\omega t)\cos(\varepsilon) + M_{H_\alpha}\cos(\omega t)\sin(\varepsilon). \tag{3.20}$$

From this equation it is possible to obtain a relation for the equivalent added damping and added mass respectively:

$$b_{eq} = \frac{M_{H_\alpha}\sin(\varepsilon)}{\phi_\alpha \boldsymbol{\omega}} \qquad a = \frac{c\phi_\alpha - M_{H_\alpha}\cos(\varepsilon)}{\phi_\alpha \boldsymbol{\omega}}. \tag{3.21}$$

This method is preferred and used by Jaouen et al. [33].

Morison's method

Morison's method was selected by Ikeda et al. [27] in order to capture the equivalent roll damping. Specifically, this method expresses the roll damping force and its equivalent linear form in the following way:

$$M_b = b_1\dot{\phi} + b_2\dot{\phi}|\dot{\phi}| = b_{eq}\dot{\phi}. \tag{3.22}$$

Furthermore,

$$M_b = b_{eq}\dot{\phi} \Rightarrow M_{b\alpha}\cos(\boldsymbol{\omega} t) = b - eq\phi_\alpha \boldsymbol{\omega}\cos(\boldsymbol{\omega} t) \Rightarrow b_{eq} = \frac{M_{b\alpha}}{\phi_\alpha \boldsymbol{\omega}}. \tag{3.23}$$

In the previous equation, the amplitude of the roll damping moment ($M_{b\alpha}$) can be calculated as the value of the total hydrodynamic moment, at the time when the roll angle (ϕ) is equal to zero, i. e. when the roll velocity becomes maximum.

Fourier series

This approach is similar to the previous. The only difference is that the amplitude of the drag force is calculated using Fourier series. More specifically, the hydrodynamic moment can be expressed as a finite summation of sinusoidal functions as follows:

$$M_H(t) = \sum_{n=1}^{N} M_{H_\alpha}\sin(\boldsymbol{\omega} n t + \varepsilon_n) = \sum_{n=1}^{N}\Big[M_{H_\alpha}\sin(\varepsilon_n)\cos(\boldsymbol{\omega} n t) + M_{H_\alpha}\cos(\varepsilon_n)\sin(\boldsymbol{\omega} n t)\Big]. \tag{3.24}$$

Where n indicated the order of the harmonic component. From the inverse relationship, the terms $M_{H\alpha}\sin(\varepsilon n)$ and $M_{H\alpha}\cos(\varepsilon n)$ (known as Fourier coefficients) can be estimated as follows:

$$M_{H\alpha}\sin(\varepsilon n) = \tfrac{2}{\zeta T}\int_0^{\zeta T} M_H(t)\cos(n\boldsymbol{\omega} t)\,dt, \tag{3.25}$$

$$M_{H\alpha}\cos(\varepsilon n) = \tfrac{2}{\zeta T}\int_0^{\zeta T} M_H(t)\sin(n\boldsymbol{\omega} t)\,dt, \tag{3.26}$$

ζ indicates the number of the cycles. The Fourier coefficients, represent the amplitudes of the components, which are in phase with $\cos(n\boldsymbol{\omega} t)$ and $\sin(n\boldsymbol{\omega} t)$ respectively. For the first harmonic component of the drag force, the amplitude, which is in phase with $\cos(\boldsymbol{\omega} t)$ is extracted, as presented in equation 3.26.

$$M_{b\alpha} = \frac{2}{\zeta T}\int_0^{\zeta T} M_H(t)\cos(\boldsymbol{\omega} t)\,dt. \tag{3.27}$$

3.10.2. Nonlinear roll damping

Apart from the equivalent linearised form, the damping moment can be expressed as a series expansion of $\dot{\phi}$ and $|\dot{\phi}|$ in the form:

$$M_b(\dot{\phi}) = b_1\dot{\phi} + b_2\dot{\phi}|\dot{\phi}| + b_3\dot{\phi}^3 + ..., \tag{3.28}$$

which is a nonlinear representation. Based on equation 3.22 and 3.28 it can be assumed that:

$$M_b(\dot{\phi}) = b_1\dot{\phi} + b_2\dot{\phi}|\dot{\phi}|... \approx b_{eq}\dot{\phi}. \tag{3.29}$$

It is important to mention that equation 3.29, is an approximation, as the nonlinear representation contains higher, odd numbered harmonics, while the equivalent linearised form contains only a first harmonic

component. For this reason, the first harmonic of the nonlinear representation should be extracted, in order to truly equate the nonlinear and the linearised part and create an equation between the equivalent and the nonlinear damping coefficients. Therefore, the Fourier coefficients of the non-linear and equivalent (linearised) damping moment, which are in phase with the first harmonic, and more specifically with the velocity, are extracted and equated:

$$\frac{1}{T}\int_0^T (b_{eq}\dot{\phi})\cos(\boldsymbol{\omega} t)\,dt = \frac{1}{T}\int_0^T (b_1\dot{\phi} + b_2\dot{\phi}|\dot{\phi}|\cos(\boldsymbol{\omega} t)\,dt \Rightarrow$$

$$\frac{1}{T}\int_0^T b_{eq}\phi_\alpha\boldsymbol{\omega}\cos(\boldsymbol{\omega} t)\cos(\boldsymbol{\omega} t)\,dt = \frac{1}{T}\int_0^T b_1\phi_\alpha\boldsymbol{\omega}\cos(\boldsymbol{\omega} t)\cos(\boldsymbol{\omega} t)\,dt + \frac{1}{T}\int_0^T b_2\phi_\alpha\boldsymbol{\omega}\cos(\boldsymbol{\omega} t)|\phi_\alpha\boldsymbol{\omega}\cos(\boldsymbol{\omega} t)|\cos(\boldsymbol{\omega} t)\,dt \Rightarrow$$

$$b_{eq}\phi_\alpha\boldsymbol{\omega} = b_1\phi_\alpha\omega + \phi_\alpha\boldsymbol{\omega}(b_2\phi_\alpha\boldsymbol{\omega}\tfrac{8}{3\pi}) \Rightarrow b_{eq} = b_1 + b_2\phi_\alpha\boldsymbol{\omega}\tfrac{8}{3\pi}. \tag{3.30}$$

Another way to achieve the same result is to equate the energy loss during a cycle, due to non-linear and equivalent linear damping.

Additionally, in cases where the equivalent linear damping (b_{eq}) is linear with the roll amplitude (ϕ_α) (for constant roll frequency), in combination with equation 3.30, it can be concluded that the non-linear roll damping coefficients (b_1 and b_2) are constant. More specifically, equation 3.30 can be evaluated at two points (equivalent linear damping – roll amplitude graph). Afterwards, the system of two equations with two unknowns can be solved the non-linear coefficients can be obtained.

By applying the same methodology, the non-linear cubic coefficient b_3 can be included. The final equation will have the following form:

$$b_{eq} = b_1 + b_2\phi_\alpha\omega\frac{8}{e\pi} + b_3\phi_\alpha^2\omega^2\frac{3}{4}. \tag{3.31}$$

3.10.3. Dimensionless coefficients

Damping coefficient, frequency of oscillation and vorticity are expressed in a dimensionless manner, in order to make the comparison between different scales easier and express these quantities in a more universal way. The dimensionless forms of the coefficients are:

$$b_{eq}^* = \frac{b_{eq}}{\rho\nabla B^2}\sqrt{\frac{B}{2g}}, \tag{3.32}$$

$$\boldsymbol{\omega}^* = \boldsymbol{\omega}\sqrt{\frac{B}{2g}}, \tag{3.33}$$

$$\boldsymbol{\omega}_z^* = \boldsymbol{\omega}_z\left(\frac{T}{2\pi}\right). \tag{3.34}$$

4

Simulation of harmonically excited roll motion– Validation cases

As mentioned earlier, the 2D numerical harmonically excited roll motion in still water, including free surface and relaxation zones (for absorption of the reflected waves) is used for the determination of the roll damping of a barge. Ikeda et al. [27] performed a great number of experiments in order to investigate the behaviour of roll damping and formulate empirical formulas for the determination of the roll damping coefficients. In these experiments the influence of different shapes, drafts, frequencies and amplitudes on the roll damping was examined. In addition, this experiments were 2 1/2 D which means that the object was invariant in one direction and it was large enough to this direction to make the end effects negligible. Thus, Ikeda's experiments can be simulated using a 2D viscous flow model. In order to validate the 2D model, Ikeda's experimental data [27] is chosen, for a range of different amplitudes and period $T = 1s$ as shown in Figure 4.1 .

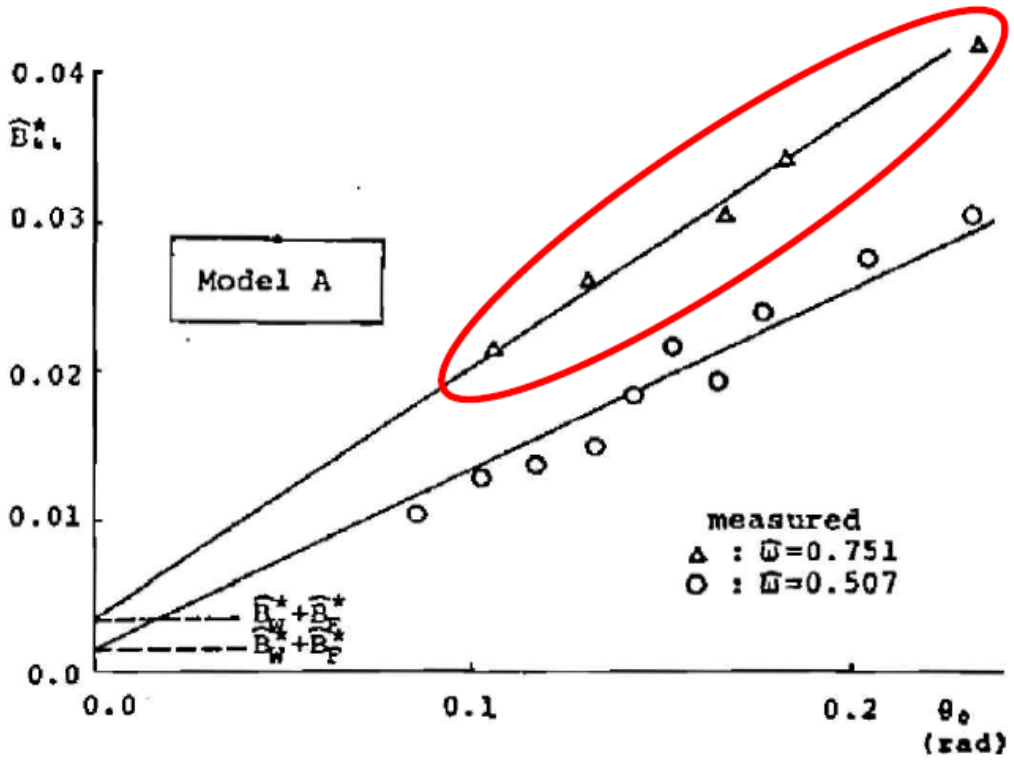

Figure 4.1: Results from Ikeda's experiment for a rectangular hull with sharp bilges

In addition, an FPSO hull section with rounded bilges and bilge keels is examined. A number of institutions and companies formed a "Joint Industry Project" (JIP) in order to investigate the non-linear damping. In this thesis, the geometry of this JIP, for one roll amplitude and frequency of oscillation, is investigated in order to examine the spatial and temporal convergence for various turbulence models. At this point the experimental results of this JIP are not available but there will become in the future.

Moreover, different numerical schemes, mesh configurations, time-steps and cell sizes, were examined in order to validate the model and achieve a balance between accuracy and computational time/efficiency. Another important aspect is the correct prediction of the details of the turbulent flow, because the separation point and vortex creation (size and duration) are determined by the turbulence. In some cases, the separation point is fixed (case with bilge keels), regardless of the intensity of the turbulence. However, the size and duration of the vortex creation is highly dependent on turbulence and for this reason, an extensive investigation of the turbulence modelling is performed.

In addition, a fully submerged case following the approach proposed by Jaouen et al. [34] is examined and compared with the results obtained with the model that directly takes into account the presence of the free surface. In this case, the free surface is neglected and the hydrodynamic moment is calculated by integrating the shear stresses and the pressures at the "true" wetted area. Afterwards, the viscous damping coefficients are obtained with Morison's method as described in subsection 3.10.1. Finally, the total damping coefficients are estimated by summing up the wave damping (calculated by potential theory) and the viscous damping (calculated viscous flow simulations). The previous approximation is decribed by equation (2.4) which is based on Ikeda's approach [27].

Finally, another free surface case, without relaxation zones is examined. In this approach the computational domain is chosen to be larger in order to avoid wave reflection. This case is examined in order to investigate how the relaxation zones and the size of the domain influence the accuracy of the numerical results.

For all cases, a start-up function $G(t)$ is applied to the roll angle in order to avoid strong transient flows at the earlier stages of the simulations. More specifically, the roll angle is multiplied with the $G(t)$ function for the first T_F periods of the simulations. Figure 4.2 shows the evolution of the roll angle in time:

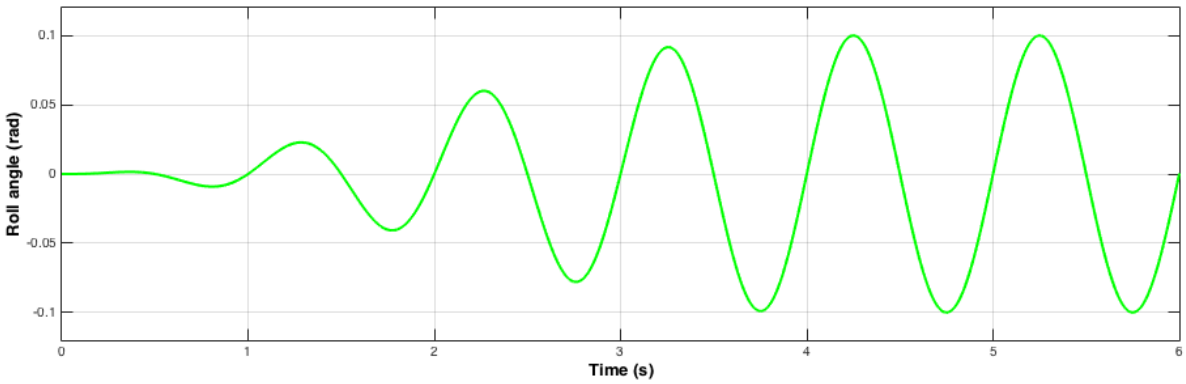

Figure 4.2: Gradual increase of the roll angle in time after multiplying it by $G(t)$ function

The start-up function is defined as:

$$G(t) = \begin{cases} \frac{1}{2}\sin\left(\frac{\omega t}{2T_F} - \frac{\pi}{2}\right) + \frac{1}{2}, & for \quad t < T_F T \\ 1, & for \quad t \geq T_F T. \end{cases} \tag{4.1}$$

Thus, the roll angle is described as:

$$\phi = G(t)\phi_\alpha \sin(\omega t). \tag{4.2}$$

4.1. Ikeda's rectangular barge with free surface and relaxation zones

In Ikeda's case, a rectangular barge with bilge radius 0 (hull with sharp bilges) is numerically analysed. The dimensions of the examined hull are $L * B * D = 0,80 * 0,28 * 0,112m$. The geometry of the hull are shown in Figure 4.3:

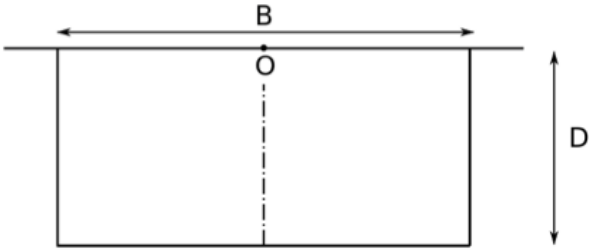

Figure 4.3: Geometry of rectangular hull shape with sharp bilges

In this case, the experiments were carried out for an amplitude range between 0.085 and $0.232rad$, and period $T = 1s$. Moreover, there are also data from simulations for Ikeda's case, by F.Jaouen et al (MARIN) and for this reason the numerical results of this study are also compared with their results. It is important to mention that the numerical results by Jaouen et al. were obtained based on the fully submerged approach [33].

Three turbulence models ($k-\varepsilon$ Realizable, $k-\omega$ SST and $kkl-\omega$) were chosen based on the reasons presented in Section 3.2 and they were applied in order to accurately capture the separation of the flow and the roll damping correctly. For all turbulence models, a verification study was performed, in order to find the optimum time-step and cell size. The verification study (in time and space) for the three turbulence models is performed for oscillation period (T) equal to 1 and roll amplitude (ϕ_a) equal to $0.107rad$. The examined turbulence models require different mesh and time configuration, and this is because the $k-\varepsilon$ Realizable model uses wall functions ($20 < y^+ < 300$) while the $k-\omega$ SST (low Re mode) and $kkl-\omega$ do not ($y^+ < 1$ and in some cases this could be relaxed to $y^+ < 3$). This means that in the first case, the mesh width orthogonal to the surface of the barge is much larger than in the second case. The same holds for the time-step, in order to have an acceptable value of the non-dimensional time-step size expressed in the Courant number and thus, stable and accurate simulation. However, the general layout of the computational domain and the distribution of the control volumes, for the 3 turbulence models is the same and it is presented in Figure 4.4.

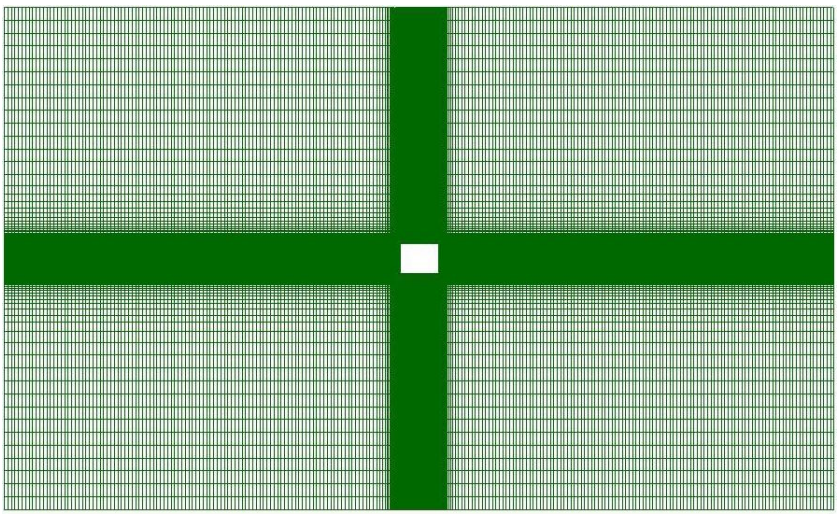

Figure 4.4: Overview of the computational domain for the Ikeda's case with free surface

Figure 4.5 presents an overview of the boundary conditions, which are used for the case with free surface. A slip condition is used for the bottom, left and right walls. In subsection 3.5.1. a descriptive explanation on

choosing this boundary condition is given. Moreover, a dynamic boundary condition, which is a combination of inlet and outlet, is selected to represent the atmospheric boundary. A moving no-slip boundary condition is chosen for the hull. Finally, non-reflective zones (relaxation zones) are included in the model in order to decrease the size of the computational domain, without having wave reflection. More information about the used boundary conditions is presented in section 3.5 and 3.6.

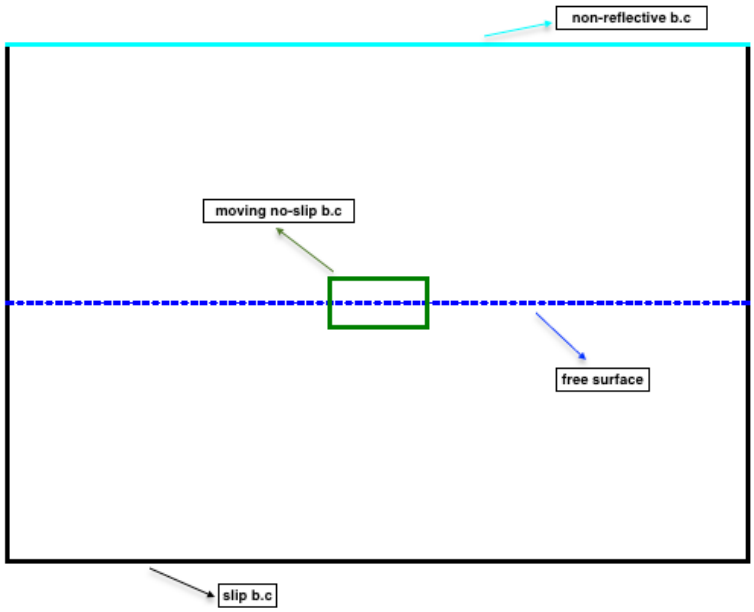

Figure 4.5: Overview of the boundary conditions for the free-surface case

4.1.1. Verification of spatial discretisation

$k-\varepsilon$ Realizable

For the $k-\varepsilon$ Realizable model four different mesh configurations were examined (Coarse, Medium, Fine, and Super Fine). The mesh refinement in the four cases is presented in Figure 4.6.

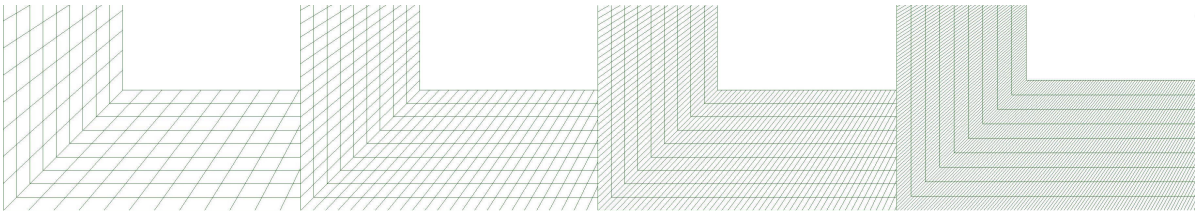

Figure 4.6: Details of the grid for the high-Reynolds turbulence models

For this type of mesh it was attempted to apply an orthogonal smoothing, for more efficient cell interpolation. However, this was not possible, as the smoothing utility swept the cells at the boundary layer of the structure. This happened because the cells at the boundary layer have a relatively high aspect ratio (in order to fulfil the y^+ criterion) and thus a small change in the cells' configuration results in high cell skewness.

The mesh verification study is performed for a small, constant time step equal to $dt = T/1600$, and for Coarse, Medium, Fine, and Super Fine meshes. The number of the cells that the examine grids contain as well as the value of y^+ are presented in Table 4.1. As can be seen y^+ is kept constant and equal to approximately 30 for all cases, in order to fulfil the y^+ criterion. In addition, the hydrodynamic moment for the

different meshes is presented in Figure 4.7.

	Coarse	**Medium**	**Fine**	**Super fine**
number of cells	9.5K	17.5K	42K	105K
$\mathbf{y^+}$	≈ 30	≈ 30	≈ 30	≈ 30

Table 4.1: Details of the meshes for $k-\varepsilon$ Realizable

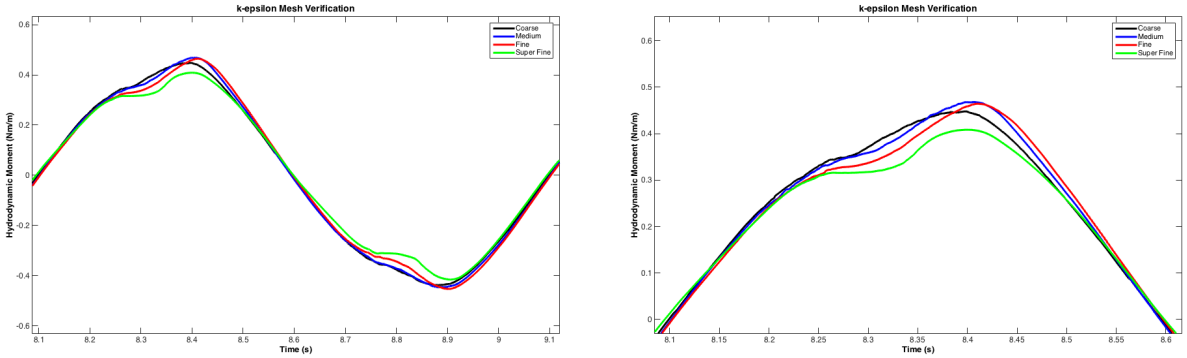

Figure 4.7: Mesh verification study for Ikeda's case for $T = 1s$ and $\phi_\alpha = 0.107rad$ using $k-\varepsilon$ Realizable turbulence model

It can be seen that the moment does not converge. This happens due to the fact that the height of the cells orthogonal to the box is really high compared to the size of the created vortices. This results to the distortion of the vortices and the decrease of the hydrodynamic moment. This phenomenon is analysed further in subsection 4.1.3.

$\underline{k-\omega \text{ SST and } kkl-\omega}$

For the low-Re models, the mesh close to the corners of the box is smoothed, in order to increase the orthogonality and thus have an accurate cell interpolation. In particular, interpolation of the cell becomes more robust as the angle of the vector, which connects the center of the two cells, decreases. Additionally, three different cell refinements (Coarse, Medium and Fine) were examined and compared with each other, for verification purposes. The number of cells and the maximum values of y^+ are presented in Table 4.2. It can be seen, that the y^+ criterion is not fulfilled in the Coarse grid, in order to examine the influence of the y^+ value on the hydrodynamic moment. Also, an overview of the examined grids is illustrated in Figure 4.8.

	Coarse	**Medium**	**Fine**
number of cells	20K	70K	280K
$\mathbf{y^+}$	3.6	1.32	0.75

Table 4.2: Details of the meshes for $k-\omega$ SST and $kkl-\omega$

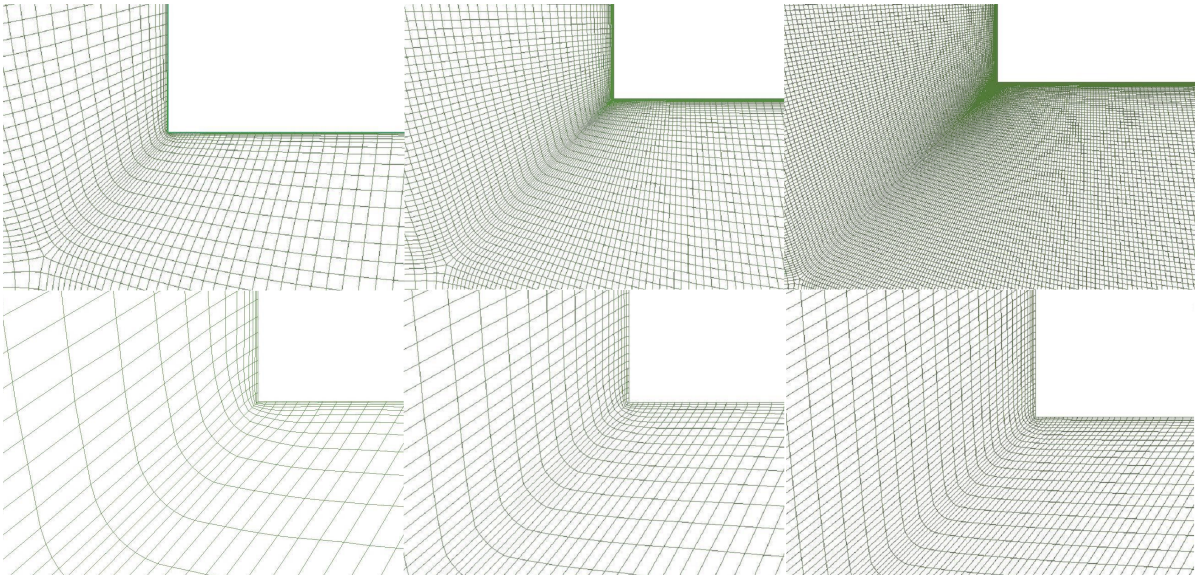

Figure 4.8: Details of the grid for the low-Reynolds turbulence models

The convergence study for the low-Reynolds number $k-\omega$ SST is presented in Figure 4.9. It can be seen that the convergence level of the hydrodynamic moment is satisfactory. In addition, the calculated damping coefficients, for the Fine and the Medium grid, are in really good agreement (less than 2% difference). The hydrodynamic moment, which is obtained from the Coarse grid, deviates from the converged solution because the maximum y^+ value of this grid exceeds considerably the limit.

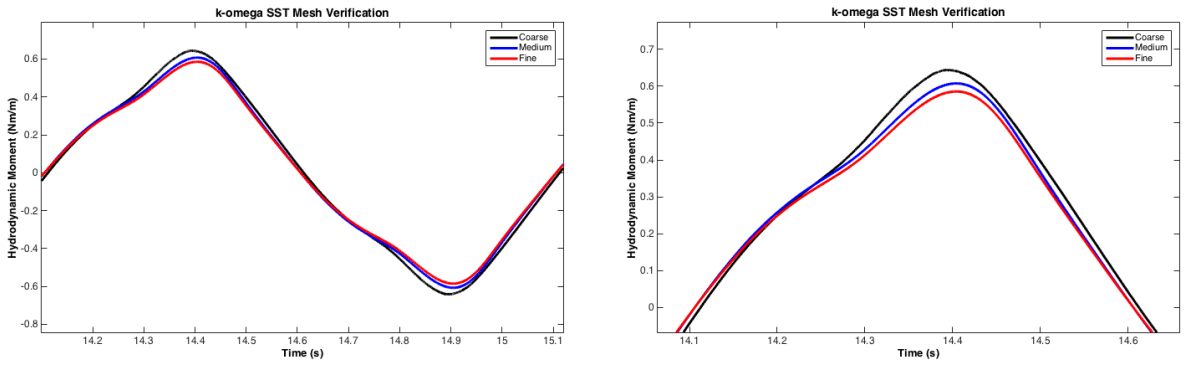

Figure 4.9: Mesh verification study for Ikeda's case for $T = 1s$ and $\phi_\alpha = 0.107rad$ using $k-\omega$ SST turbulence model

Finally, the $kkl-\omega$ turbulence model is examined. A mesh-verification study is performed for the grids, which are mentioned above. As it can be seen in Figure 4.10, the obtained hydrodynamic moments, from the Fine and the Medium grids, converge to a great degree. On the other hand, the Coarse grid diverges, as the moment has different shape and the damping coefficient differs significantly (around 25% from the Medium), compared to the other two cases. This shows strong sensitivity of the $kkl-\omega$ model to y^+ parameter, as in the Coarse case the y^+ exceeds the limit. However, when the y^+ value is within the prescribed limits, the solution obtained by using this turbulence model rapidly converges.

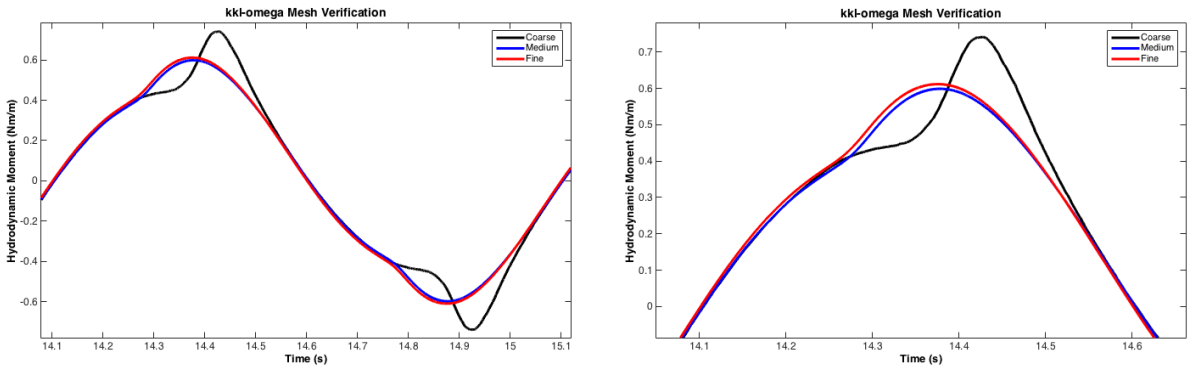

Figure 4.10: Mesh verification study for Ikeda's case for $T = 1s$ and $\phi_\alpha = 0.107rad$ using $kkl-\omega$ turbulence model

The outcome of this verification study is that the medium grid can be considered as a "converged" mesh (for both $k-\omega$ SST and $kkl-\omega$), and thus it is used for further calculations. However, only the $kkl-\omega$ turbulence model is chosen for further examination, as the $k-\omega$ SST turned to be strongly dependent on the initial values of the turbulence quantities.

More specifically, $k-\omega$ SST turbulence model proved to be sensitive to the initial and boundary conditions of the turbulent quantities (k and ω). This means that the selection of these values, significantly affects the solution and they should be selected carefully. Often, reasonless values could affect the accuracy and the reliability of the results to a great extent. In this thesis, the effect of these values (k and ω) on the results is examined. The hydrodynamic moment as a function of time for Ikeda's case ($\phi_\alpha = 0.1065rad$ and $T = 1s$) is presented in Figure 4.11. Solutions are computed for four different combinations of initial values for k and ω and compared with each other.

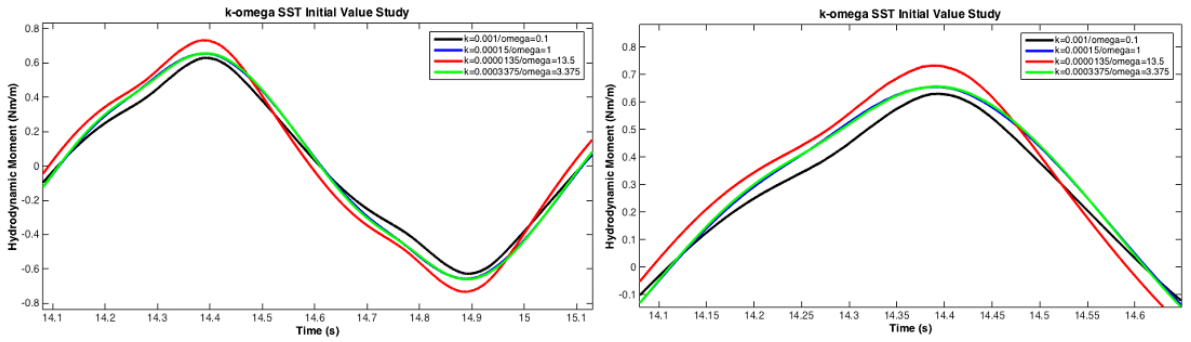

Figure 4.11: Influence of the initial values of the turbulent quantities on the hydrodynamic moment/Ikeda's case for $T = 1s$ and $\phi_\alpha = 0.107rad$

It is obvious that different initial-boundary values of k and ω, lead to different amplitude, shape, and phase shift of the hydrodynamic moment. More specifically, the turbulent (eddy) viscosity depends on the k/ω ratio:

$$\frac{k}{\omega} = \frac{\mu}{\rho}\frac{\mu_t}{\mu} \tag{4.3}$$

Equation 4.3 proves that artificial damping can be imposed on the solution, based on the k/ω ratio [64]. For example, for high values of this ratio (black curve), the eddy viscosity ratio also becomes larger and thus artificial damping is imposed on the flow field. This artificial flow damping leads to more turbulent flow and thus to lower separation and vortex creation levels (which means lower roll damping force). This results in lower total hydrodynamic moment.

It can be concluded that even though $k-\omega$ SST is proven to be the best turbulence model for industrial applications, it is strongly dependent on the initial and boundary values of the turbulent quantities and for

this reason these values should be carefully selected, based on empirical and semi-empirical formulas.

4.1.2. Verification of temporal discretisation

Apart from the mesh verification, it is of great importance to also verify the time-step. For this reason, a time verification study was performed for both $k-\varepsilon$ Realizable and $kkl-\omega$.

$k-\varepsilon$ Realizable

The time verification study of the $k-\varepsilon$ Realizable model is performed for four different time-steps. The examined time steps are: $T/200$, $T/400$, $T/800$, and $T/1600$. Figure 4.12 presents the convergence of the hydrodynamic moment for different time-steps and the same grid. (Fine mesh for the $k-\varepsilon$ Realizable was selected in the subsection 4.1.1.

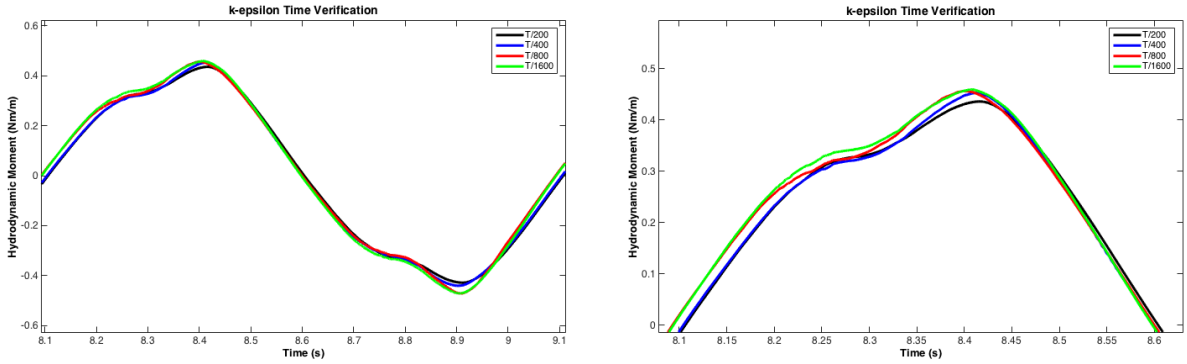

Figure 4.12: Time verification study for Ikeda's case for $T = 1s$ and $\phi_\alpha = 0.107rad$ using $k-\omega$ Realizable turbulence model

As it is depicted in Figure 4.12, the solution is converging. Especially for time steps equal to $T/800$ and $T/1600$, the hydrodynamic moment fits satisfactorily. The only area where the red and the green curves are not converging is between 8.2 and 8.3 seconds, where the moment for the $T/1600$ time step is slightly higher. However, this difference is obviously negligible.

$kkl-\omega$

A time-step sensitivity study was carried out for the $kkl-\omega$ turbulence model and for four different time-steps. The examined time steps are $T/800$, $T/1600$, $T/3200$, and $T/6400$. The last two, extensively small time-steps are chosen, in order to investigate in depth the effect of such a choice on the moment. The respective study is depicted in Figure 4.13.

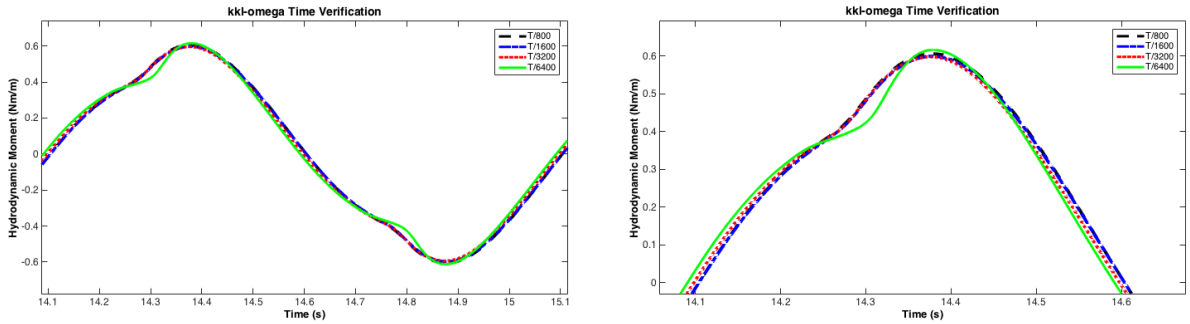

Figure 4.13: Time verification study for Ikeda's case for $T = 1s$ and $\phi_\alpha = 0.107rad$ using $kkl-\omega$ turbulence model

It can be seen, that the hydrodynamic moment for $T/800$, $T/1600$ and $T/3200$ is converging. Unexpectedly, the same is not happening for $T/6400$, as the "shape" of the moment at the peak changes. However, $T/1600$ is selected for further calculations, as it is a good compromise between accuracy of the results and computational time.

4.1.3. Turbulence model selection

After performing a sensitivity study in time and space for different turbulence models, it is concluded that the $k-\varepsilon$ Realizable (high Re) and the $kkl-\omega$ are worth considering for further examination (for the chosen time-steps and cell sizes respectively). Figure 4.14 presents the hydrodynamic moment for these two models:

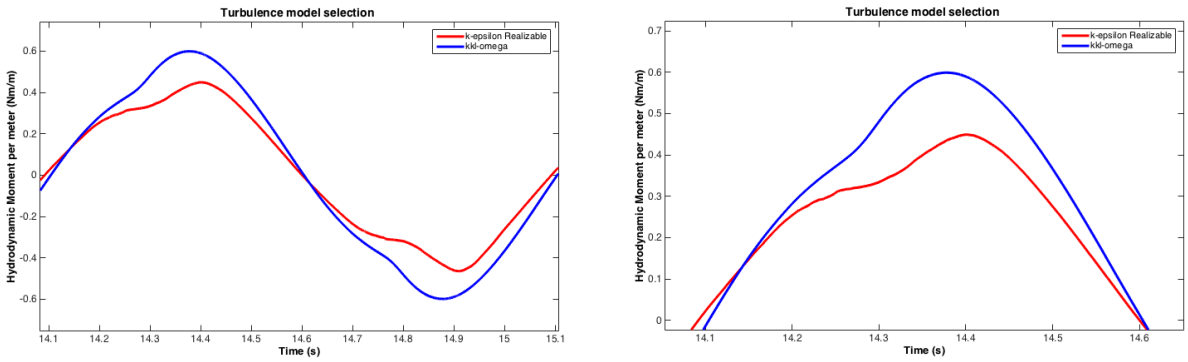

Figure 4.14: Turbulence model selection between $kkl-\omega$ and $k-\varepsilon$ Realizable/ Ikeda's case for $T = 1s$ and $\phi_\alpha = 0.107rad$ using

It can be seen that the moment estimation, from the two examined models, differs significantly. In order to examine which model captures correctly the physical phenomenon, the vorticity field is visualized as it is shown in Figure 4.15 and Figure 4.16.

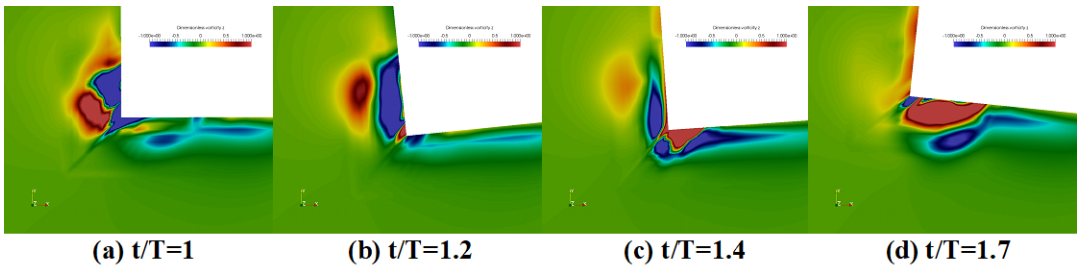

Figure 4.15: Dimensionless vorticity at different instants for the $k-\varepsilon$ Realizable/ Ikeda's case for $T = 1s$ and $\phi_\alpha = 0.107rad$

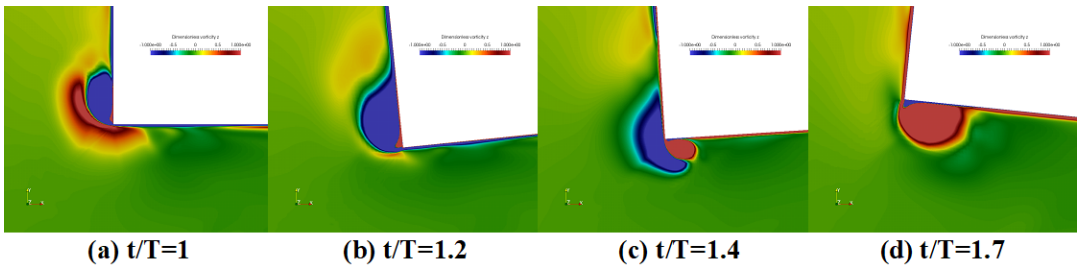

Figure 4.16: Dimensionless vorticity at different instants for the $kkl-\omega$ turbulence model/ Ikeda's case for $T = 1s$ and $\phi_\alpha = 0.107rad$

The $k-\varepsilon$ Realizable case does not capture the expected vorticity field, while the $kkl-\omega$ does (regarding the vorticity field published by Jaouen et al. [33, 34]). The main reason, for this sizeable divergence, is not the

turbulence model ($k-\varepsilon$ Realizable) directly, but the required mesh for this turbulence model. Specifically, as it is mentioned previously, the $k-\varepsilon$ Realizable is a high Reynolds-number turbulence model and thus requires a y^+ higher than 30. This requirement leads to a coarse mesh in the direction perpendicular to the structure, which distorts the vortex creation. For this reason, the $kkl-\omega$ turbulence model is finally selected for further calculations.

It is important to mention that, turbulence models should be also selected based on the Reynolds number. In the examined roll motion case, the Reynolds number is calculated as follows:

$$Re = \frac{U_\phi D}{\nu}, \tag{4.4}$$

where D is the draft, ν is the kinematic viscosity, U_ϕ is the maximum velocity of the point located at the corner of the bilge and it is equal to $L_r\dot{\phi}$, where L_r is the the lever arm.

As reference, an empirical combination of the Reynolds number for a flat plat and a cylinder is used. It can be see that for a relatively small sized structure, as in the examined case, the Reynolds number is small (approximately 30000 – case of laminar boundary layer and turbulent separation) and thus it is wise to use a low Reynolds number model.

4.1.4. Influence of roll amplitude on roll damping.

All amplitudes, which were investigated by Ikeda, for period $T = 1s$, are tested, in order to examine the accuracy of the numerical model. Initially, the influence of the roll amplitude on the hydrodynamic moment and the vorticity field is explored, as it is exhibited in Figure 4.17.

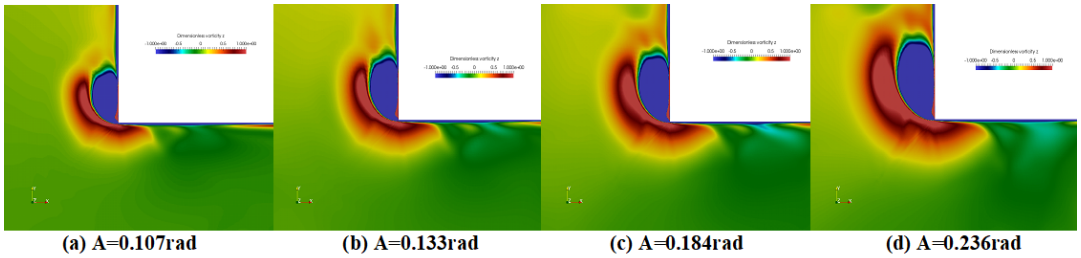

Figure 4.17: Dimensionless vorticity for various roll amplitudes/ Ikeda's case for $T = 1s$

The dimensionless vorticity field, for oscillation period (T) equal to 1 and various amplitudes is shown in Figure 4.18. It seems that the roll amplitude affects the vorticity field extensively, as the size of vortices increases with the amplitude.

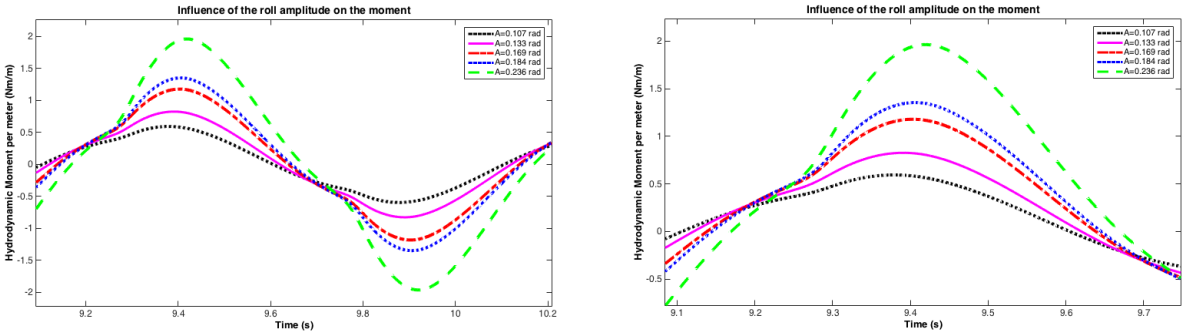

Figure 4.18: Influence of the roll amplitude on the hydrodynamic moment/ Ikeda's case for $T = 1s$ and various amplitudes

It can be seen that the amplitude of the moment is increasing with the roll amplitude. Moreover, an interesting observation is the fact that the roll amplitude affects the shape and the phase shift of the moment. The

source of these indications is probably the fact that nonlinearity increases, while roll amplitude inclines. For this reason, in order to examine the magnitude of the nonlinearity and thus the applicability of the equivalent linearisation to the damping coefficient, it is of high importance to apply a Fast Fourier Transform (FFT) to the hydrodynamic signals. The FFT expresses a time signal as a summation of harmonically related sinusoidal functions, transfers it from the time domain to the frequency domain and indicates the pairs of frequencies and amplitudes of the decomposed time trace. Figure 4.19 shows the FFT of the hydrodynamic moment, for each roll amplitude:

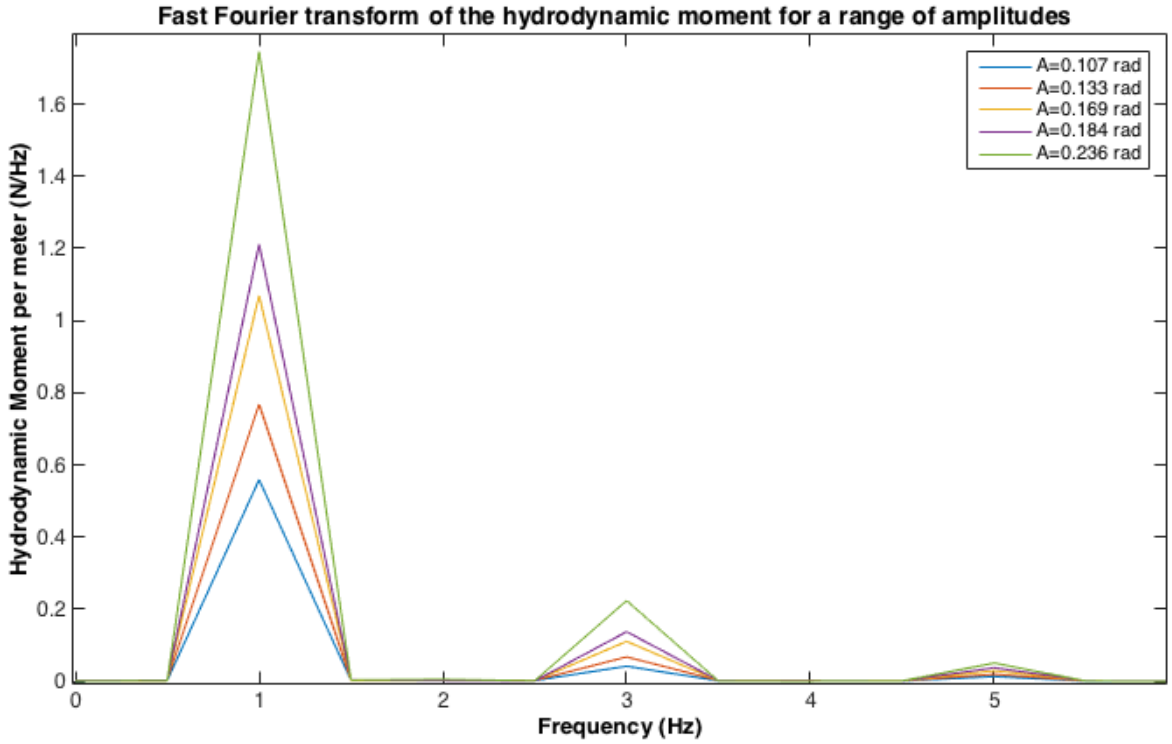

Figure 4.19: Fast Fourier transform of the hydrodynamic moment including free surface effects/ Ikeda's case for $T = 1s$ and various amplitudes

Except for the first harmonic (ω), the FFT demonstrates the existence of higher, odd numbered harmonics (3ω, 5ω etc.), which is a typical characteristic of drag (damping). Moreover, the higher harmonics are negligible, compared to the first, and for this reason the equivalent linearisation for the damping determination is a valid approach. However, as the amplitude of the roll motion amplifies, the percentage of the third harmonic also increases. Table 4.3 shows the percentage of the third harmonic (based on the first), for each roll amplitude.

Amplitude	**Percentage of the third harmonic**
0.107	7.5 %
0.133	8.8%
0.169	10.3%
0.184	11.3%
0.236	13.2%

Table 4.3: Percentage of the third harmonic of the damping moment nondimensionalized with the total damping moment, including free surface effects/ Ikeda's case for $T = 1s$ and various amplitudes

Founded on the previous statement, we can maintain that in some cases, the equivalent linearised approach might be insufficient and other extraction techniques should be used. Nevertheless, for the examined

case the equivalent linearised damping can be safely estimated.

Figure 4.20 illustrates the dimensionless damping coefficients in relation to the roll amplitude. The same graph includes the experimental results by Ikeda et al [26, 27] and the numerical results by Jaouen et al [33, 34]. The damping coefficients are calculated with the same method that Ikeda used (Morison's method, subsection 3.9.2), in order to exclude the effect of different damping extraction methods.

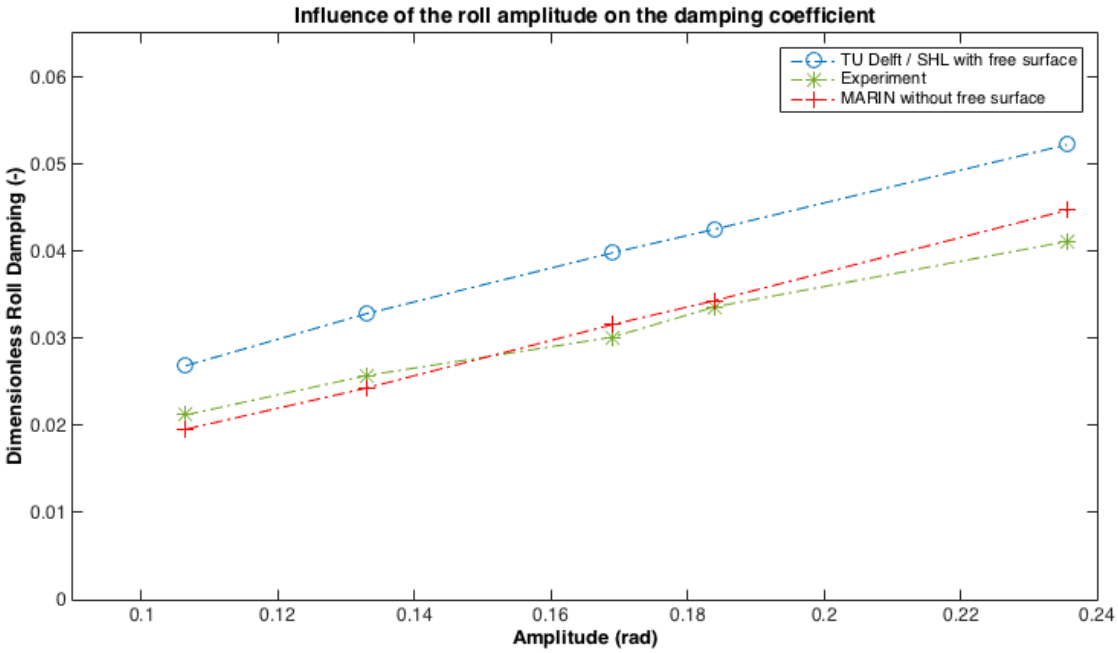

Figure 4.20: Influence of the roll amplitude on the dimensionless roll damping coefficient, including free surface effects and relaxation zones/ Ikeda's case for $T = 1s$ and various amplitudes

The obtained numerical results demonstrate a constant overestimation of the damping compared to the experimental obtained values. However, the numerical results capture accurately the linear trend of the damping coefficient with the amplitude. The error between the experimental and the numerical results is presented by Table 4.4.

Amplitude	**Percentage of the third harmonic**
0.107	21.02%
0.133	21.63%
0.169	24.31%
0.184	20.96%
0.236	21.28%
Average	21.84%

Table 4.4: Difference between the experimental and the numerical dimensionless damping coefficient including free surface effects and relaxation zones/ Ikeda's case for $T = 1s$ and various amplitudes

4.2. Ikeda's case for fully submerged cross section and free surface correction from potential theory algorithms

Free surface is extremely sensitive to high aspect ratio cells and large mesh deformations in combination with non-orthogonality. These could lead to artificially high velocities and high pressures at the free surface and at

the boundary of the hull. An additional reason for the numerical distortion of the results, when free surface is included in the model, is the existence of relaxation zones. Figure 4.21 presents extremely high artificial velocities at the free surface of the computational domain, resulted by high non-orthogonality. This extreme case was mitigated by creating a more orthogonal grid to the free surface area.

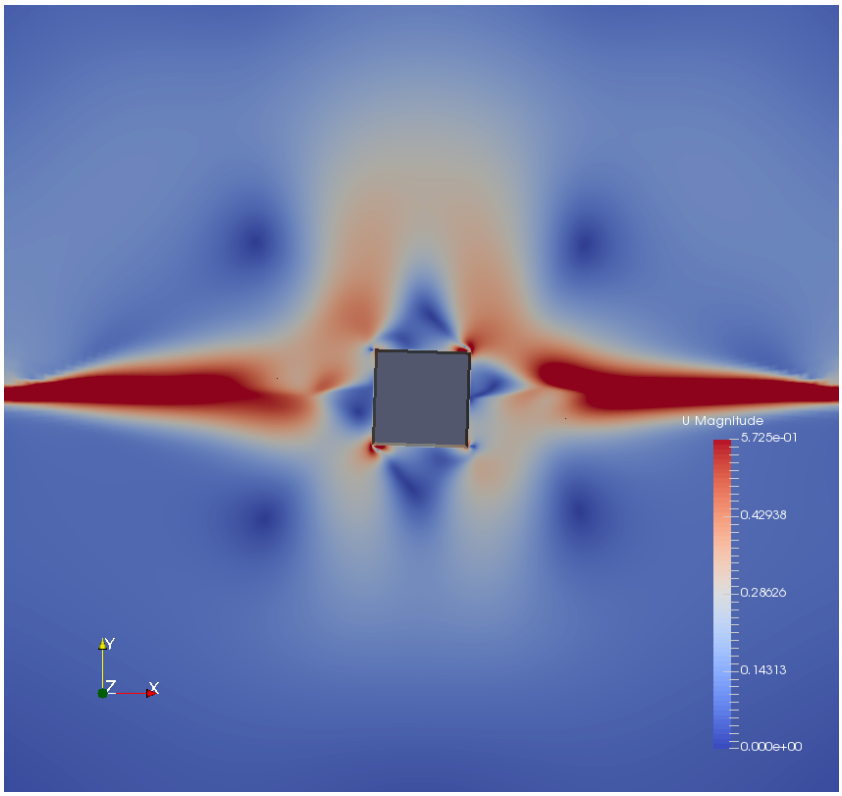

Figure 4.21: High artificial velocities at the free surface of the computational domain due to high non-orthogonality

Due to the fact that full scale barge requires to have large amplitude of roll motion (and therefore large mesh deformations) and because the roll damping coefficients with the existence of free surface and relaxation zones are overestimated, it is decided to also examine Ikeda's case without the existence of free surface in the viscous flow model. The used methodology is based on Ikeda's assumption, that the total roll damping can be expressed as a superposition of wave, eddy and frictional damping. As Korpus et al. and Jaouen et al. [33, 34, 42] proposed, viscous flow algorithms can calculate the eddy and frictional components, while potential flow simulations can estimate the wave damping. Thus, the model geometry is mirrored in the water plane and it is completely submerged. Afterwards, the forced oscillation test is performed to the fully submerged body and the total hydrodynamic moment is obtained by integrating the pressures and shear stresses at the truly submerged area only. In this case (2.3) simplifies to:

$$M_H = M_\alpha(\ddot{\phi}) + M_b(\dot{\phi}). \tag{4.5}$$

This happens because the restoring moment (M_c) is equal to zero in the absence of free surface and gravity. The rest of the procedure, in order to obtain the damping coefficient (in this case viscous part only) remains the same one as in section 4.1. Finally, the total damping coefficient is obtained by adding the wave damping (from potential-theory algorithm) to the viscous part.

The boundary condition, which is applied to the top and bottom hull, is a moving no-slip condition as in the "free-surface" case. An opening pressure (outlet) condition is applied to the far-field boundary. Figure 4.22 depicts the previous description. More information about the used boundary conditions can be found in section 3.5.

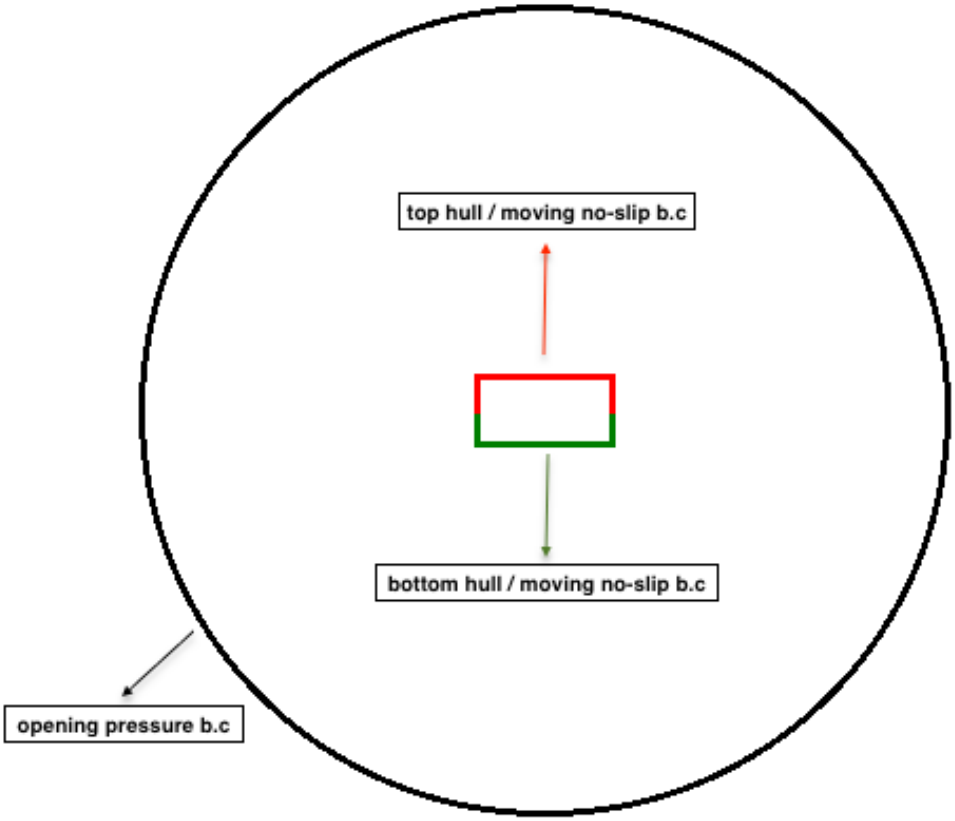

Figure 4.22: Overview of the boundary conditions for the fully submerged case

The discretisation schemes, the selected cell-size (refinement) and time-step, and the number of inner and outer iterations of the solution algorithm are entirely the same as in the free-surface case (section 4.1). The main difference between these two cases is the modelling of the free surface.

The damping coefficients are calculated with the averaging Morison's technique (as in section 4.1 and Ikeda's experiment). The influence of the roll amplitude on the hydrodynamic moment is illustrated in Figure 4.23.

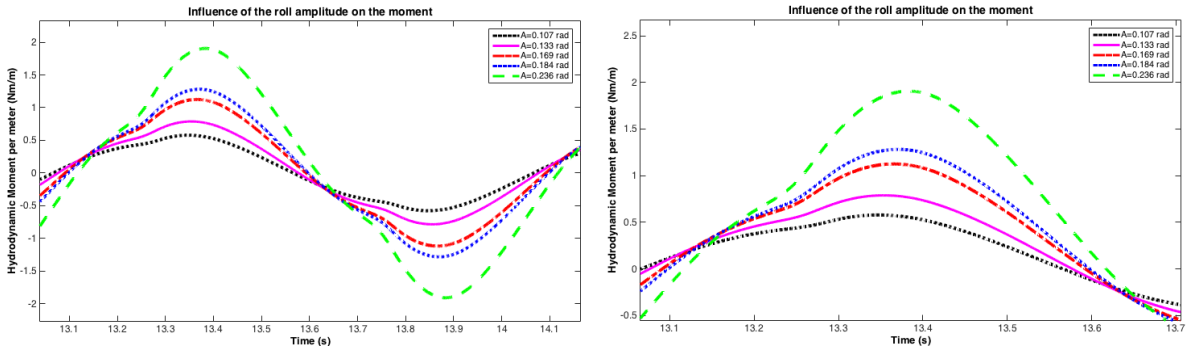

Figure 4.23: Influence of the roll amplitude on the hydrodynamic moment excluding free surface effects/ Ikeda's case for $T = 1s$ and various amplitudes

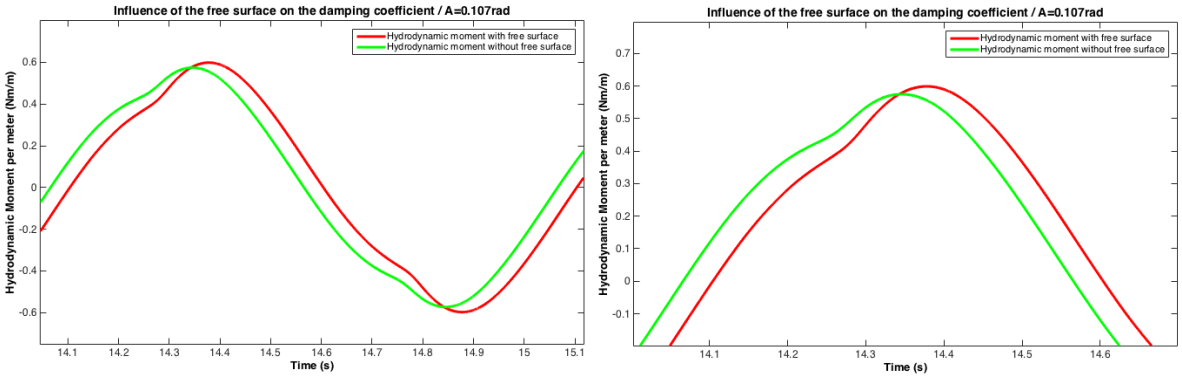

Figure 4.24: Hydrodynamic moment with free-surface effects and relaxation zones and without free-surface effects/ Ikeda's case for $T = 1s$ and $\phi_\alpha = 0.107rad$

It can be seen that the hydrodynamic moment in the submerged case behaves similarly to the "free-surface" case. However, compared to the free surface case (Figure 4.24) there is a decrease in the amplitude and a phase shift. This can be explained based on the fact that in the case where free surface is not present, the restoring part and the free surface (wave damping) are absent. Additionally, Figure 4.25 presents the FFT of the hydrodynamic moment for various amplitudes and Table 4.5 shows the percentage of the third harmonic for each roll amplitude.

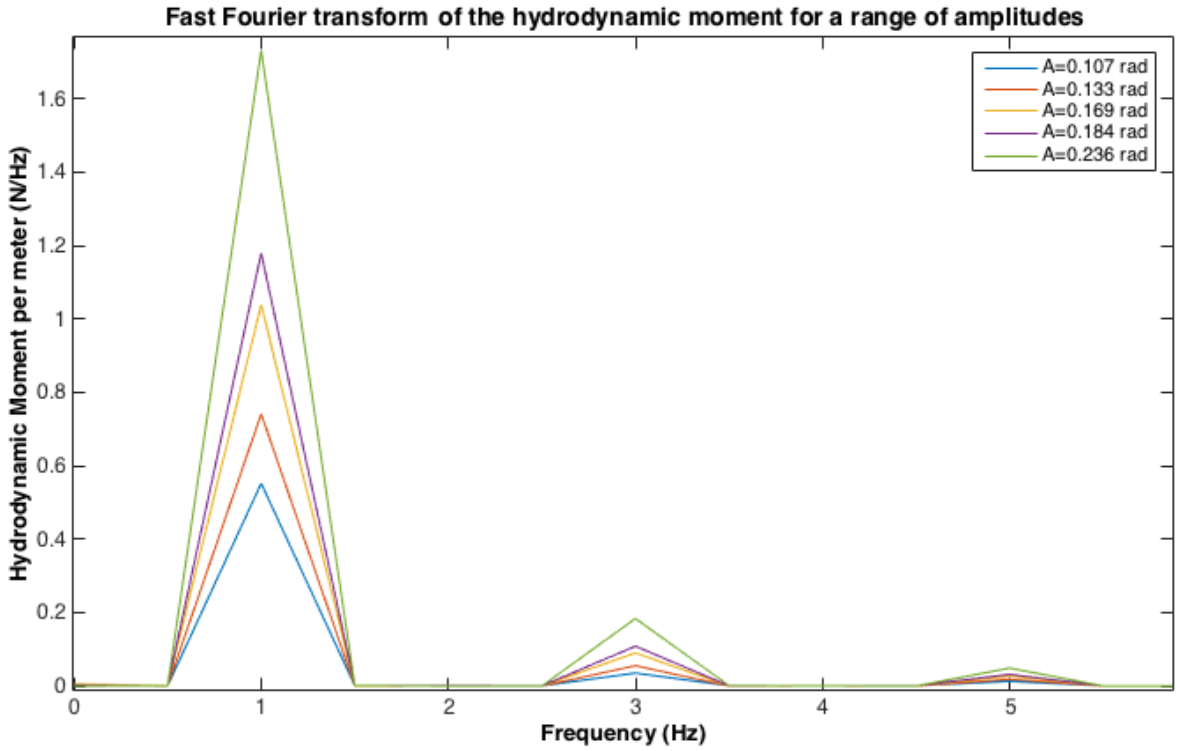

Figure 4.25: Fast Fourier transform of the hydrodynamic moment excluding free surface effects/ Ikeda's case for $T = 1s$ and various amplitudes

Amplitude	Percentage of the third harmonic
0.107	6.4%
0.133	7.5%
0.169	8.7%
0.184	9.2%
0.236	10.6%

Table 4.5: Percentage of the third harmonic of the damping moment nondimensionalized with the total damping moment, excluding free surface effects/ Ikeda's case for $T = 1s$ and various amplitudes

Figure 4.26 shows the damping coefficients for the submerged case (where the wave damping is added to the viscous part) with Ikeda's experimental data, for period $T = 1s$. Additionally, the same figure presents the numerical results obtained by Jaouen et al. [33, 34]

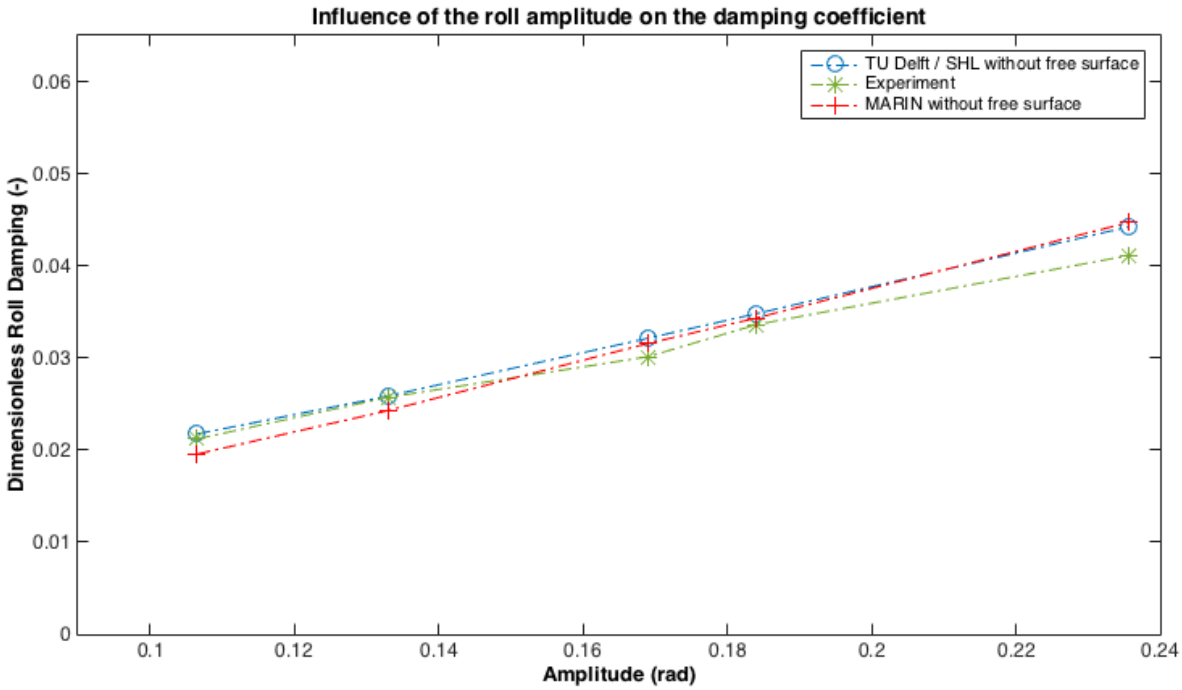

Figure 4.26: Influence of the roll amplitude on the dimensionless roll damping coefficient, excluding free surface effects/ Ikeda's case for $T = 1s$ and various amplitudes

It can be observed that the numerical results (using viscous flow algorithms) obtained by the "submerged" methodology are in excellent agreement with the experimental data and with the numerical results calculated by Jaouen [33]. Table 4.6 shows the difference between the numerical and the experimental results.

Amplitude	Percentage of the third harmonic
0.107	2.47%
0.133	0.57%
0.169	6.25%
0.184	3.42%
0.236	7.05%
Average	3.95%

Table 4.6: Difference between the experimental and the numerical dimensionless damping coefficient excluding free surface effects/ Ikeda's case for $T = 1s$ and various amplitudes

By modelling the free surface in a different way the roll damping coefficients are significantly different.

Figure 4.27 shows the damping coefficients, using different way of modelling free surface in relation with the experimental data.

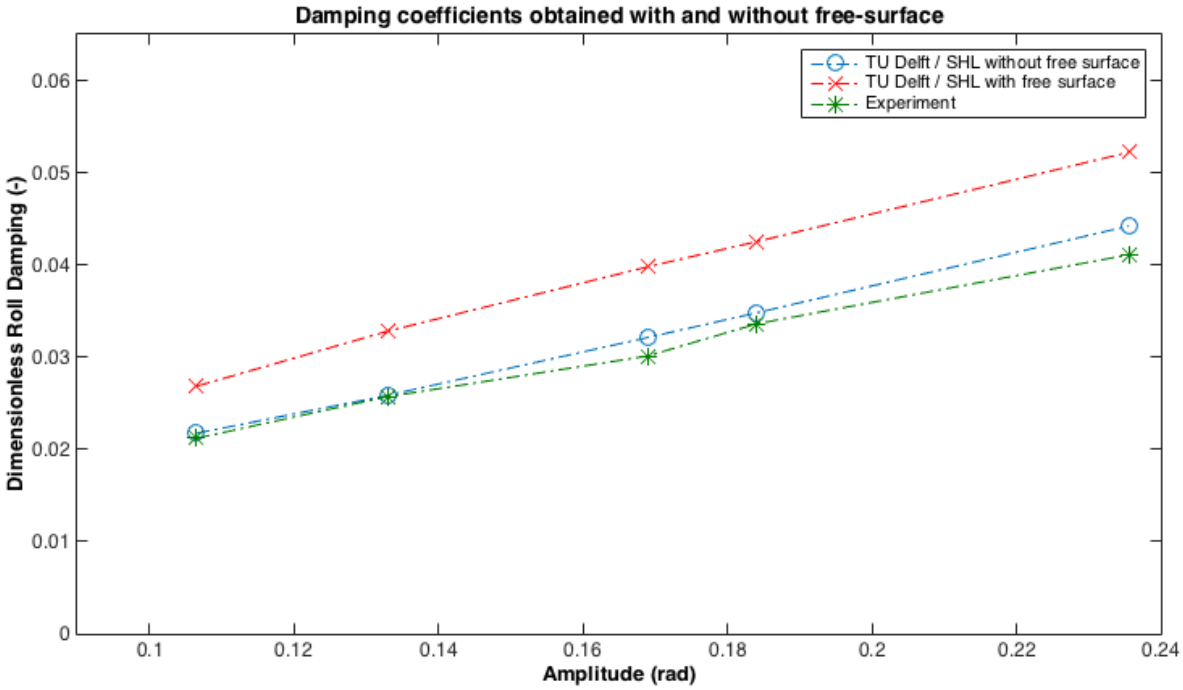

Figure 4.27: Dimensionless roll damping coefficients with free surface effects and relaxation zones and without free surface effects/ Ikeda's case for $T = 1s$ and various amplitudes

The fact that the damping coefficients derived by the "submerged methodology" are in good agreement with the experimental results while the data calculated with free surface are not, means that the existence of free surface creates complications and numerical errors (for the reasons which are mentioned earlier in this chapter). Moreover, it is important to mention that the submerged approach requires significantly less computational power compared to a model, which includes free surface effects.

Finally, Figure 4.28 represents the dimensionless roll damping coefficient as a function of the roll amplitude for two dimensionless frequencies of oscillation. It shows very good agreement between the experimental data of Ikeda and the numerical results in the case where the free surface is not included. This also verifies that the damping coefficient is linear with the roll amplitude. However, the experimental results diverge from the linear trend. This could be due to the uncertainty of the experimental data.

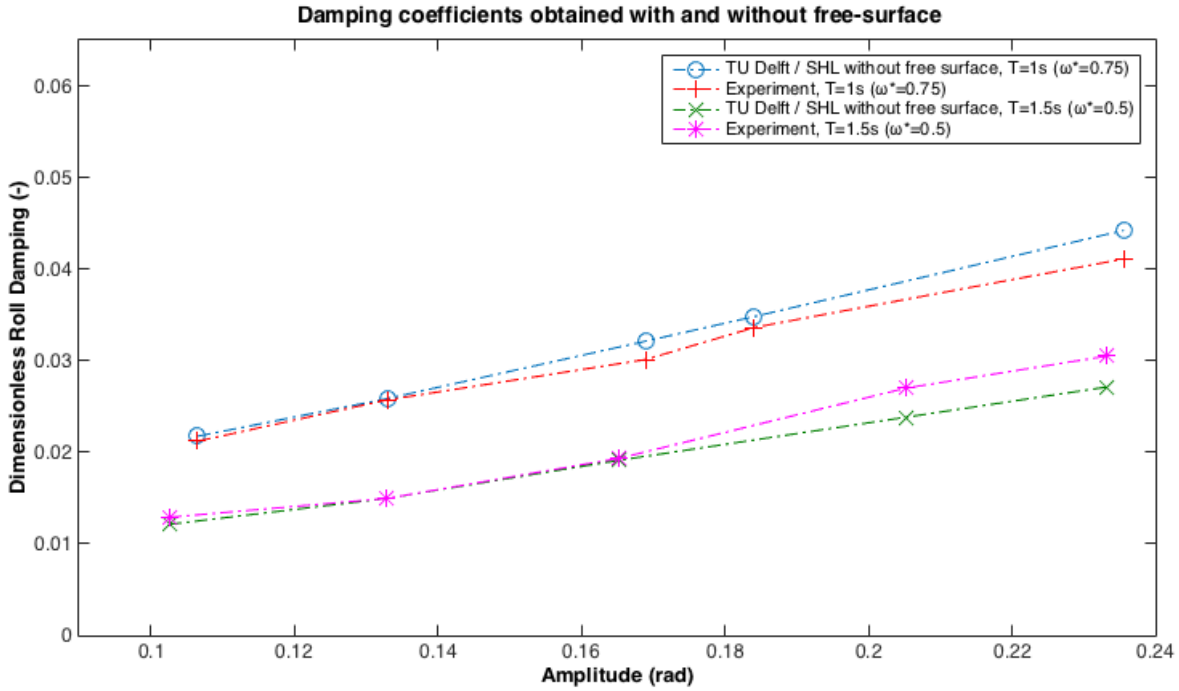

Figure 4.28: Influence of roll amplitude on the dimensionless damping coefficients for the submerged case/ Ikeda's case for $T = 1s$ and $T = 1.5s$ and various amplitudes

4.3. Ikeda's case with free surface and extended boundaries

The roll damping coefficients are overestimated, in the case where the free surface is modelled with the VoF method and the relaxation zones are used for the absorption of the reflected waves, as it is mentioned in chapters 4.1 and 4.2. In order to find the source of this over prediction, many attempts were done. One of them was to disable the relaxation zones and extend the two far-field boundaries (left and right boundaries) sufficiently in order to prevent early reflection of the generated waves (by the forced oscillation motion) on the lateral wall. Figure 4.29 illustrates the two free surface approaches.

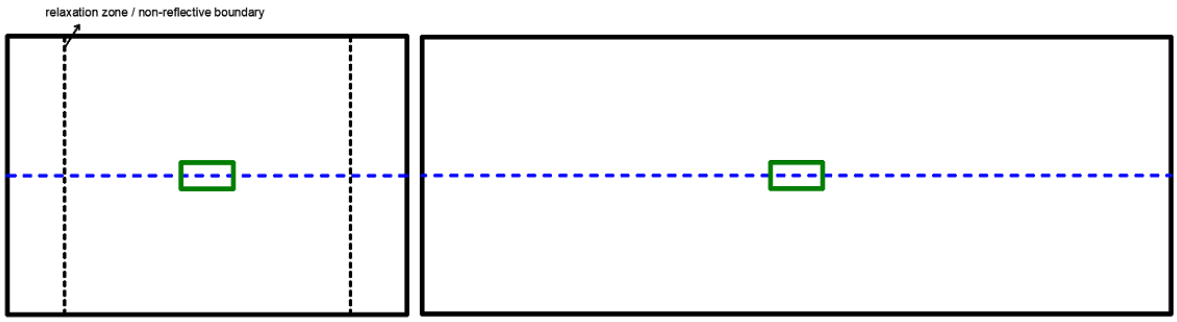

Figure 4.29: Left: Sketch of the computational domain with relaxation zones and non-extend boundaries, Right: Sketch of the computational domain without relaxation zones and extend boundaries

Additionally, the minimum length of the domain should be specified, based on the total number of roll cycles, in order to avoid any interference by reflected waves. Thus, the minimum length of the half-domain, can be calculated by equation 4.6:

$$L_{1/2} = \frac{\lambda N + 2\Delta x}{4}, \tag{4.6}$$

where $L_{1/2}$ is the minimum length of the half domain, $\lambda = 2\pi g/\omega^2$ is the approximated length of the gener-

ated wave, N is the number of cycles and Δx is half the breadth (B) of the cross section. In the examined case $\lambda \approx 1.562m$, $N = 15$, $\Delta x = 0.14m$ and thus the length of the half domain is equal to approximately 6 meters. It is important to mention that the numerical settings, turbulence model, mesh and time configurations are identical with the previous examined cases.

Figure 4.30 compares the total hydrodynamic moment in cases where the relation zones are included and excluded (extend far-field boundaries case) from the model.

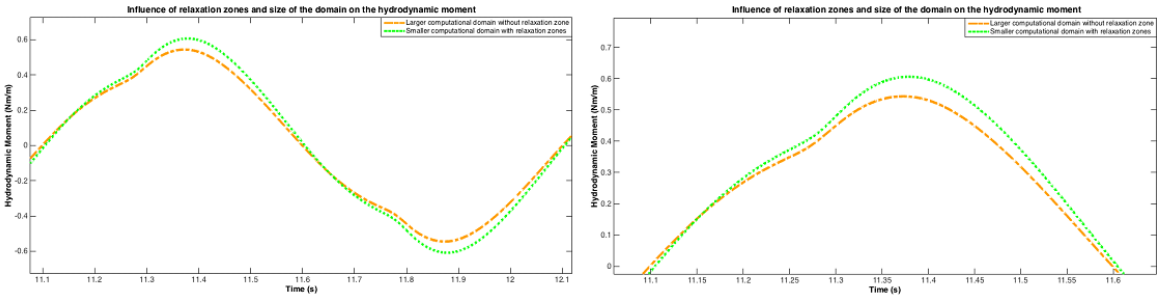

Figure 4.30: Hydrodynamic moment with larger domain (excluding relaxation zones) and smaller domain (including relaxation zone) / Ikeda's case for $T = 1s$ and $\phi_\alpha = 0.107rad$

It can be seen that the hydrodynamic moment is significantly influenced by the extension of the computational domain and the removal of the relaxation zones. More specifically, the hydrodynamic moment is remarkably decreased, compared to the initial approach. However, the shape and the phase of the moment curve are remained unchanged.

The change in the hydrodynamic moment influences the roll damping coefficient and specifically it is decreased by 13.63%. At the same time the error, between the numerical and the experimental results also reduces to 8.55%, which is notably lower from the error of the previous free surface approach (smaller domain with relaxation zones for wave absorption). Figure 4.31 compares the dimensionless damping coefficients, for variant roll amplitudes, obtained by the free surface models with and without relaxation zones. Table 4.7 presents the error between the experimental and the numerical dimensionless damping coefficients for larger domain (excluding relaxation zones) and smaller domain (including relaxation zones).

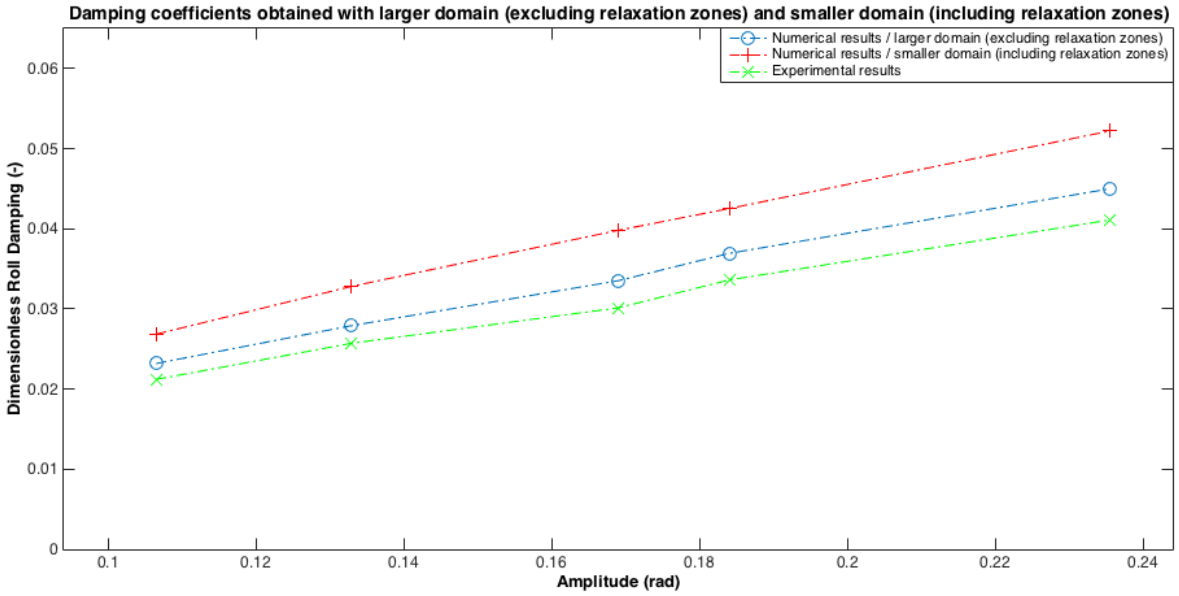

Figure 4.31: Influence of roll amplitude on the dimensionless damping coefficients for larger domain (excluding relaxation zones) and smaller domain (including relaxation zones) / Ikeda's case for $T = 1s$ and $\phi_\alpha = 0.107rad$

Amplitude	Error for larger domain (excluding relaxation zones)	Error for smaller domain (including relaxation zones)	Error reduction
0.107	8.55%	21.02%	12.47%
0.133	7.87%	21.63%	13.76%
0.169	10.10%	24.31%	14.21%
0.184	8.99%	20.96%	11.96%
0.236	8.66%	21.28%	12.62%
Average	8.83%	21.84%	13.00%

Table 4.7: Error between the experimental and the numerical dimensionless damping coefficients for larger domain (excluding relaxation zones) and smaller domain (including relaxation zones)/ Ikeda's case for $T = 1s$

The dimensionless damping coefficients with free surface and larger computational domain, excluding the relaxation zones, is again linear with the roll amplitude and the error between the experimental and the numerical results is significantly reduced, compared to the coefficients obtained with smaller computational domain (including relaxation zones). However, the dimensionless damping coefficients are still overestimated by a constant factor, with respect to the experimental data (average error 8.83% and standard deviation 0.81%).

4.4. Nonlinear form of roll damping coefficients

In subsection 3.10.2. it is described how the equivalent linearised roll damping coefficients can be expressed in its nonlinear form, in cases where the damping coefficients are linear with the roll amplitude. By following this methodology, the constant (for a specific frequency of oscillation) damping coefficients, b_1 and b_2, are calculated for all the examined numerical cases and the experimental data of Ikeda et al. [27]. In order to sum-up, Figure 4.32 presents the linearised dimensionless damping coefficients for all examined cases.

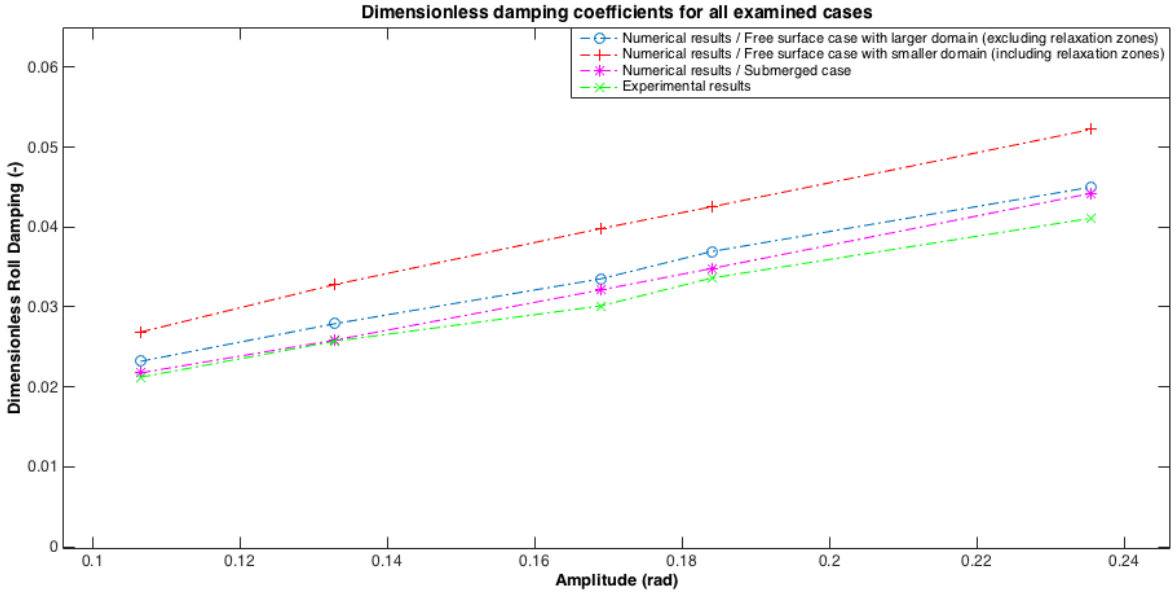

Figure 4.32: Influence of roll amplitude on the dimensionless damping coefficients for all examined cases/ / Ikeda's case for $T = 1s$

As illustrated in Figure 4.33, the dimensional damping coefficients from all cases are fitted in linear curves in order to extract the damping coefficient for the nonlinear representation.

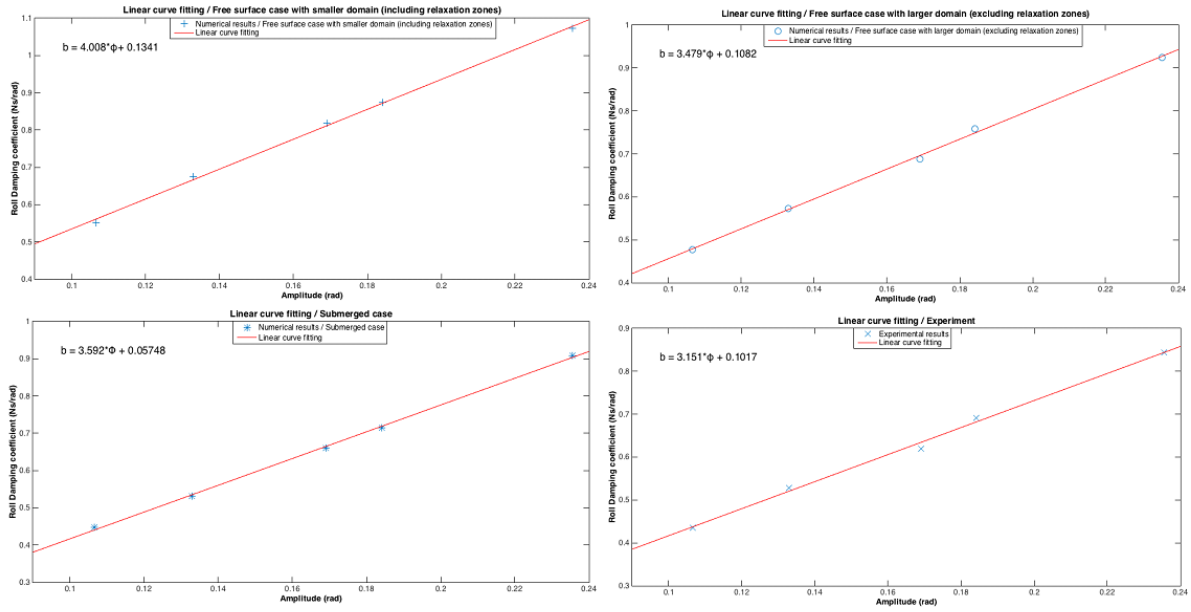

Figure 4.33: Linear curve fitting of the roll damping coefficients for the examined cases

The roll damping coefficients b_1 and b_2, in a dimensional and dimensionless form, are calculated based on the equations of the linear fitted curves (Figure 4.33) in combination with equation (3.30) and are presented in Table 4.8.

	$\mathbf{b_1}$ **(Ns/rad)**	$\mathbf{b_2}$ **(Ns^2/rad^2)**	$\mathbf{b_1^*}$	$\mathbf{b_2^*}$
Free surface case with smaller domain (including relaxation zones)	0.1341	0.7515	0.00652	0.3062
Free surface case with larger domain (excluding relaxation zones)	0.10821	0.6522	0.00527	0.2658
Submerged case	0.05748	0.6735	0.00278	0.2744
Experiment	0.1017	0.5908	0.00495	0.2407

Table 4.8: Coefficients for the nonlinear representation of roll damping for all examined cases

	Error $\mathbf{b_1}$	**Error $\mathbf{b_2}$**
Free surface case with smaller domain (including relaxation zones)	24.08%	21.39%
Free surface case with larger domain (excluding relaxation zones)	6.07%	9.44%
Submerged case	43.84%	12.28%

Table 4.9: Difference between the experimental data and the numerical results for all the examined cases, for coefficients b_1 and b_2.

Table 4.9 illustrates the difference between the experimental data and the numerical results for all the examined cases, for coefficients b_1 and b_2. As it is expected, for the free surface case with smaller domain, the nonlinear coefficients are significantly overestimated similarly to the linearised equivalent damping coefficient for the same case.

For the submerged case, the coefficient b_1 is highly overestimated by over 43%, which is an unexpected difference, as the linearised equivalent coefficient for this case is accurate. This significant error occurred due to the fact that the free surface is neglected and the wave damping, which is a big part of the coefficient b_1, is artificially implemented in the total equivalent damping coefficient. The nonlinear coefficient b_2 differs from the experimental value by 12.28%, which is a realistic deviation.

Finally, for the free surface case with larger domain, the damping coefficients b_1 and b_2 diverge from the experimental data by approximately 6% and 9.5%, respectively. As it seems, this case gives a balanced solution for both equivalent linearised and nonlinear representation of the roll damping.

4.5. Nonlinear roll damping of an FPSO

In this case, forced oscillation tests of a 2D hull section with bilge keels are performed in a still water channel, for different roll amplitudes and periods. This geometry is selected in order to investigate a more complicated case with bilge keels and at the same time to examine the spatial and temporal convergence for various turbulence models. The general outline of the test-case is described in Figure 4.34. The details of the geometry of the bilge keels are exhibited in Figure 4.35.

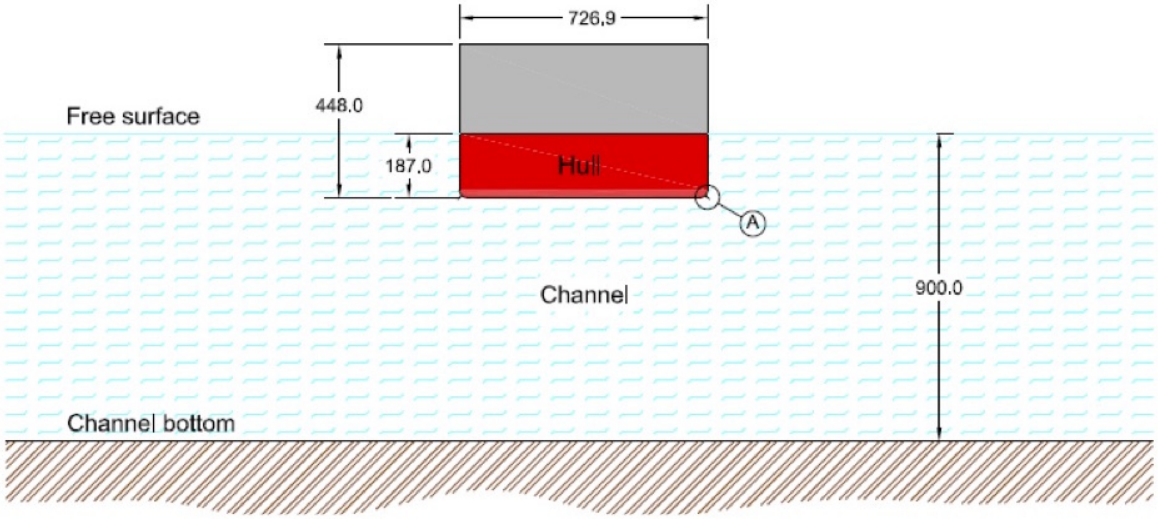

Figure 4.34: Geometry of the FPSO section

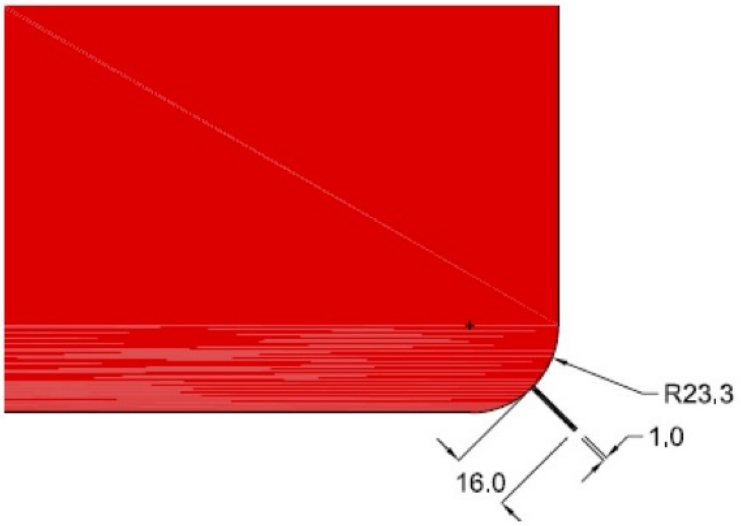

Figure 4.35: Geometry of the bilge keels of the JIP roll-motion

In this thesis, the case with roll amplitude (ϕ_α) equal to 5^o and period of oscillation (T) equal to 1.73 seconds is investigated. From experience and previous investigation, it is concluded that the Realizable $k-\varepsilon$ and all High Reynolds number turbulence models are not ideal for modelling the separated flow and the creation of vorticity at the tip of the bilge keels for this specific case (more details can be found in subsection (4.1.3)), as the Reynolds number is relatively small. For this reason, the $k-\omega$ SST and the $kkl-\omega$ turbulence models have been used. With these models the boundary layer should be refined all the way across the viscous sub layer of the boundary layer of the structure. However, the $k-\omega$ SST is very sensitive to the selected initial values of the turbulent kinetic energy and turbulent frequency. For this reason, two initial value cases are inspected.

A mesh verification study is performed for the chosen models and three mesh and cell sizes are used (Coarse, Medium and Fine). Each one has the following characteristics:

	Coarse	**Medium**	**Fine**
number of cells	26016	69850	227429
max initial cell height	$2.5 \bullet 10^{-5}$	$5 \bullet 10^{-5}$	10^{-4}
maxy$^+$	3.748	1.978	1.054

Table 4.10: Details of the mesh verification study

The selected time step for the mesh verification study is equal to $T/1600$ ($0.00108125s$), this selection is based on the analysis in Section 4.1 and 4.2 and leads to an acceptable nondimensional timestep in the simulations. The computational domain and the refinement near the bilge keels are illustrated in Figure 4.36 and Figure 4.37, respectively.

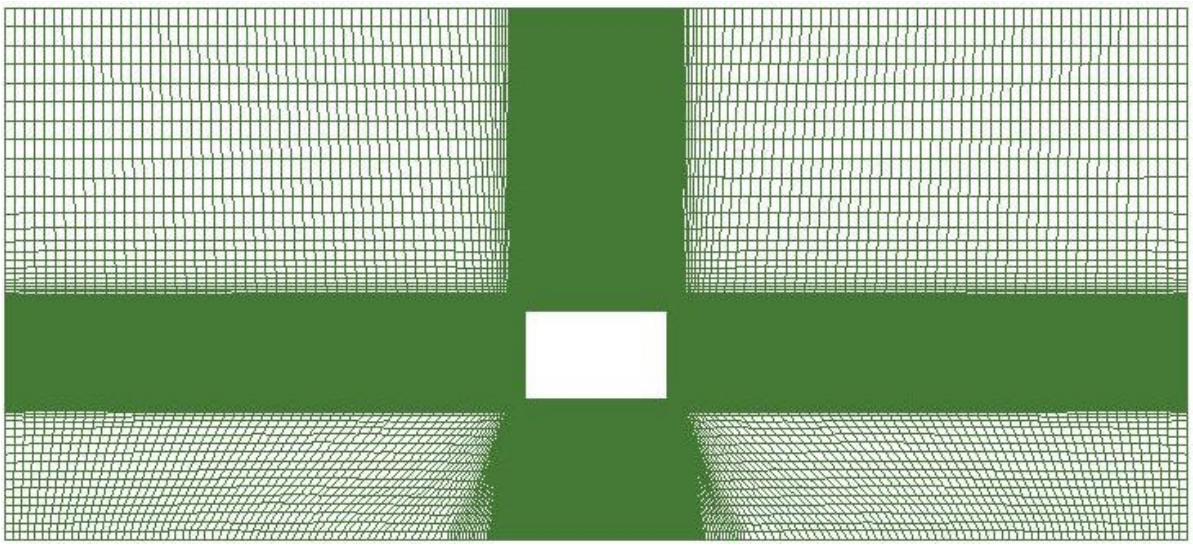

Figure 4.36: Overview of the computational mesh for the JIP roll-motion

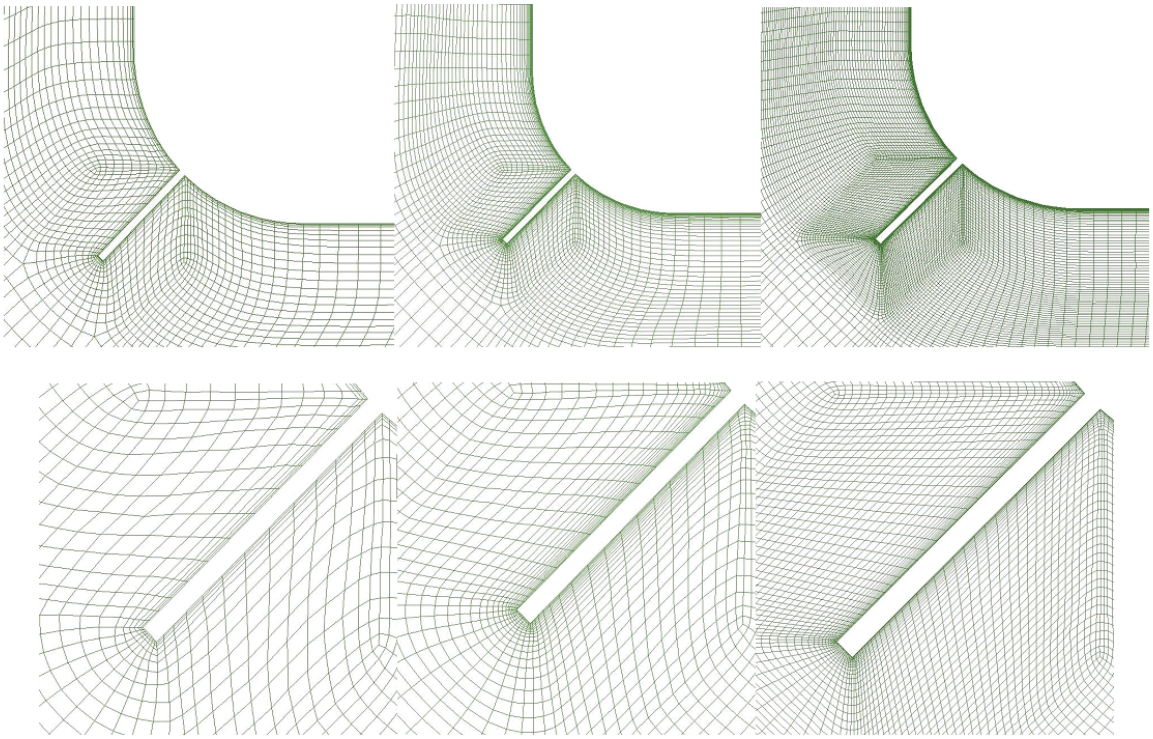

Figure 4.37: Refinement of the mesh in the vicinity of the bilge keels for the FPSO section

Figure 4.38 and Figure 4.39 present the mesh verification study based on the hydrodynamic moment, for the $k-\omega$ SST turbulent model. Each case has different initial conditions for the turbulence quantities. Figure 4.32 shows the mesh verification study for the $kkl-\omega$ turbulence model. Table 4.11 presents analytically the turbulence models and the initial conditions for each corresponding figure.

Cases	Turbulence model	Initial conditions for the turbulence quantities	Figure
1	$k-\omega$ SST	$k = 0.01$, $\omega = 0.1$	Figure 4.38
2	$k-\omega$ SST	$k = 0.00001$, $\omega_{air} = 0.078$, $\omega_{water} = 1.7$	Figure 4.31
3	$kkl-\omega$	$kl = 0, kt = 0, \omega = 0$	Figure 4.32

Table 4.11: Error between the experimental and the numerical dimensionless damping coefficient

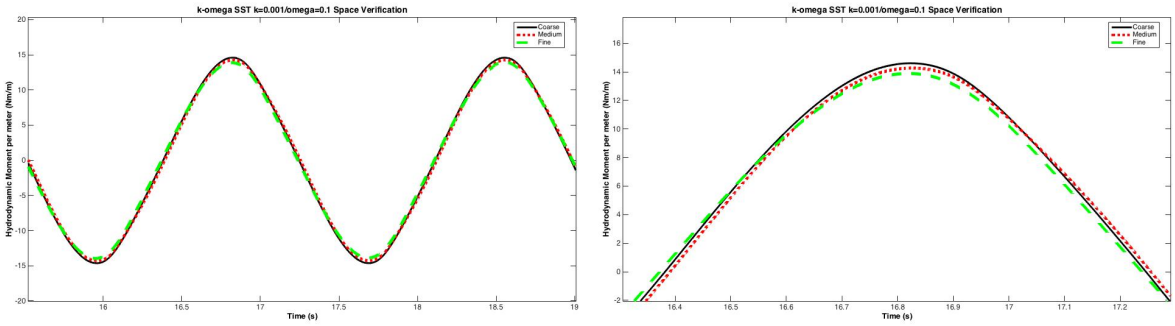

Figure 4.38: Hydrodynamic moment for $k-\omega$ SST turbulence model, roll amplitude $\phi_\alpha = 5^o$, $k = 0.001/\omega = 0.1$

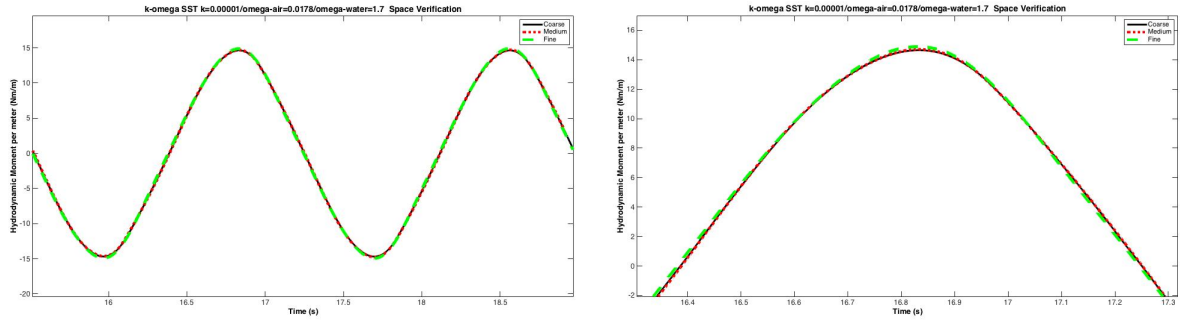

Figure 4.39: Hydrodynamic moment for $k-\omega$ SST turbulence model, roll amplitude $\phi_\alpha = 5^o, k = 10^{-5}/\omega_{air} = 0.078/\omega_{water} = 1.7$

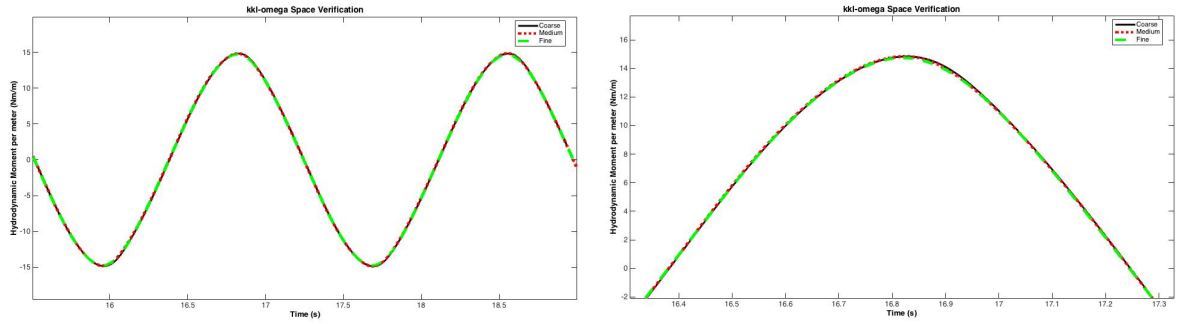

Figure 4.40: Hydrodynamic moment for $kkl-\omega$ turbulence model, roll amplitude $\phi_\alpha = 5^o, kl = 0/kt = 0/\omega = 0$

The grid convergence for case 1 is not as satisfactory as for cases 2 and 3. Especially in case 3 ($kkl-\omega$) the hydrodynamic moment clearly converges significantly as the grid becomes finer. Figure 4.41 illustrates a comparison between the examined turbulence models and initial values of the turbulent quantities.

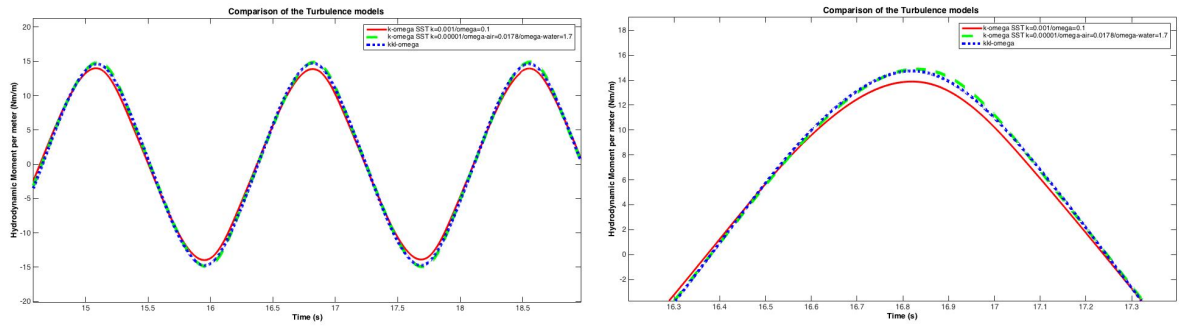

Figure 4.41: Hydrodynamic moment for different turbulence model, roll amplitude $\phi_\alpha = 5^o$

It becomes apparent that the hydrodynamic moment diverges for different k and ω. This means that the low Reynolds number $k-\omega$ SST turbulence model is affected significantly by the initial values of the turbulence quantities. The computed hydrodynamic moment strongly depends on the initial conditions chosen for the turbulent kinetic energy and frequency when the $k-\omega$ SST model is used. The $k-\omega$ SST model was developed to reduce the influence of initial and inflow boundary conditions on the solution but in this case their influence is clearly present. The $k-\omega$ SST model for initial conditions, which corresponds to case 2, is in agreement with the $kkl-\omega$ model. This happens because the initial values in case 2 represent realistically the physics of the problem (initial velocity is zero, thus the eddy viscosity ratio and the turbulent viscosity should initially be very small).

5

Numerical prediction of the roll damping characteristics of a full scale barge

5.1. Case description and geometry of the model

After an extensive examination of various methods, turbulence models, and numerical discretisation techniques for the determination of the roll damping of a rectangular shaped hull (Ikeda's case), the obtained knowledge and experience is applied to a full scale barge. The "fully submerged" approach is used, as it is proven that it can provide reliable viscous roll damping estimations and thus substantial corrections for potential flow algorithms. At the same time, this approach requires less computational time than the free surface cases. In this current thesis, three different cases are examined, with drafts equal to 35%, 47%, and 60% of the total height. The length of the examined barge is more than 100 meters and therefore a 2D model can be applied as the object is large enough in longitudinal dimension in order to make the end effects negligible. Each case has a different total Vertical Center of Gravity (VCG), in order to realistically represent, true loading conditions in operational and survival circumstances. Figure 5.1 illustrates the geometry of the examined barge and points out the different drafts and VCGs.

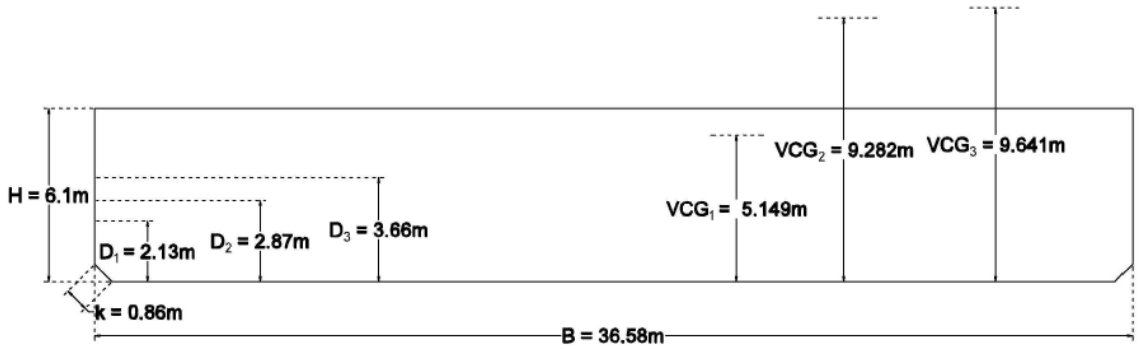

Figure 5.1: Geometry of the full-scale barge

Additionally, for each case, the viscous damping coefficients are calculated, for constant frequency of oscillation equal to its natural frequency and various roll amplitudes. The frequency of oscillation is chosen to be equal to the natural frequency, as the roll amplitude reaches its peak at this frequency area. The correct determination of the roll damping at the natural frequency (and thus at the peak roll amplitude) is of high importance, in order to increase the workability and at the same time provide safe predictions. Table 5.1

presents the properties of the three cases:

	Draft	**VCG**	**Natural frequency**
Case 1	D_1=2.13m	VCG_1=5.149m	f_1=0.945rad/s
Case 2	D_2=2.87m	VCG_2=9.282m	f_2=0.80rad/s
Case 3	D_3=3.66m	VCG_3=9.641m	f_3=0.75rad/s

Table 5.1: Overview of the examined cases

The numerical forced oscillation tests are performed for 5^o, 7.5^o, 10^o, 12.5^o, 15^o and 17.5^o in each case.

The k-omega SST turbulence model, for a high-Reynolds number, is used in order to capture the turbulence effects and the separation of flow, as accurately as possible. In this case the Reynolds number is much higher than 10^6 (because the velocities of a full scale case are high) and thus it is acceptable to use a high-Reynolds number turbulence model. Moreover, the created vortices are large enough in order to be described with a cell resolution for a high-Reynolds number model. Finally, it would be infeasible to use a low-Reynolds number model, as it would require very small cells at the boundary layer (and thus a very small time-step), compared to the size of the structure and the frequency of oscillation.

The boundary conditions and the methodology are the same as the ones described in section 4.2. A general overview of the computational grid is illustrated in Figure 5.2. Oval shape is chosen for the domain, as it is suitable for cases with rotational motion, since the mesh deformation is smoothly transferred to the outer domain.

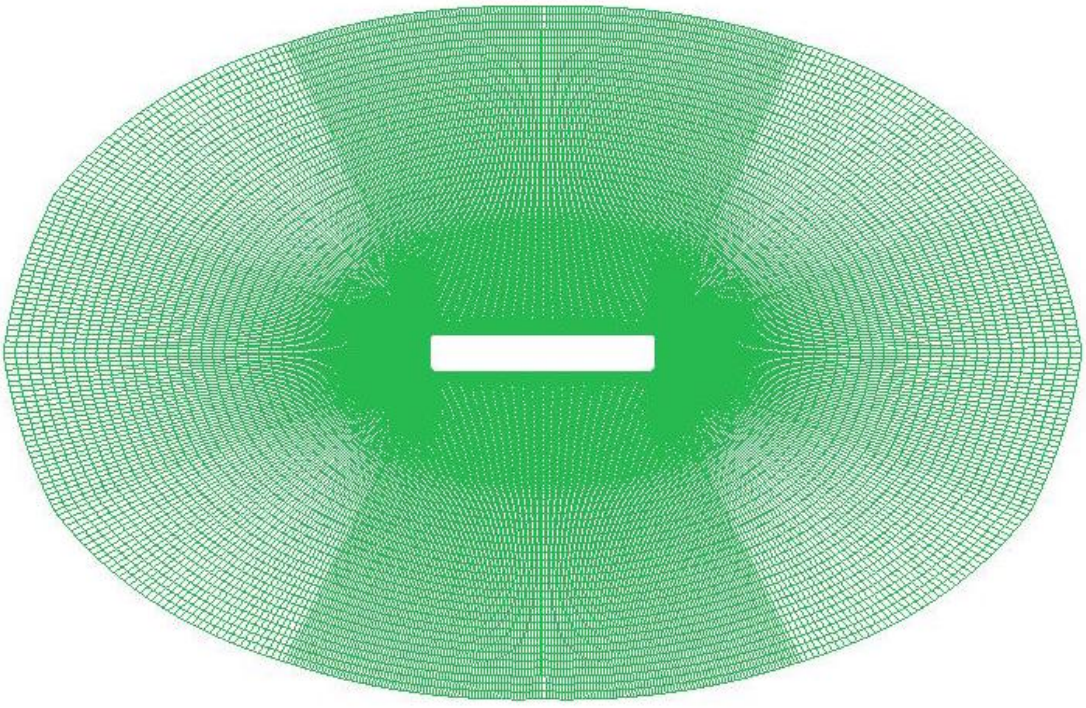

Figure 5.2: Overview of the computational grid for the full scale barge

5.2. Verification study

A verification study in space and time is performed for draft equal to 35% of the total height, and roll amplitude equal to 5^o. For the verification study the hydrodynamic moment is compared for various grid-sizes and timesteps. For the mesh verification three consecutively refined mesh configurations have been created. Details about the grids and the y^+ value are shown in Table 5.2. Moreover, Figure 5.3 illustrates the refinement of grids at the vicinity of the bilge.

	Coarse	**Medium**	**Fine**
number of cells	13.5K	54K	216K
$\mathbf{y^+}$	$20 < y^+ < 300$	$20 < y^+ < 300$	$20 < y^+ < 300$

Table 5.2: Details of the meshes for k-epsilon Realizable

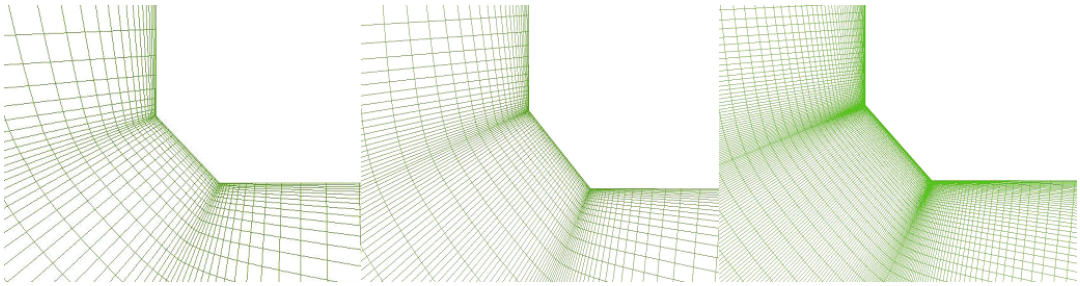

Figure 5.3: Grid refinement at the vicinity of the bilge

Figure 5.4 shows the mesh verification for the Coarse, Medium, and Fine grids. It can be seen that the solution is converging, as the mesh becomes finer. For further calculations the Medium grid has been used, as it is a good compromise between accuracy and time efficiency.

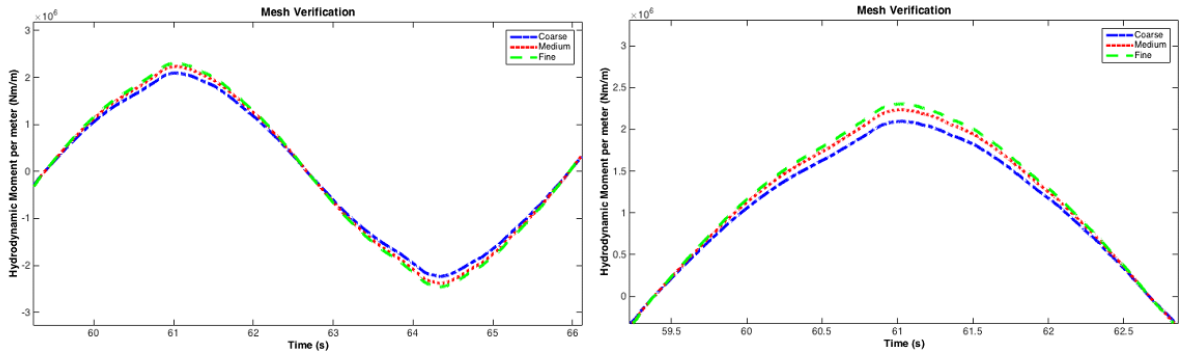

Figure 5.4: Mesh verification study for the full-scale barge

Additionally, apart from the mesh verification study, a time verification study is performed. The examined timesteps are $T/1600$, $T/3200$ and $T/6400$. Figure 5.5 shows the hydrodynamic moment for these three time-steps.

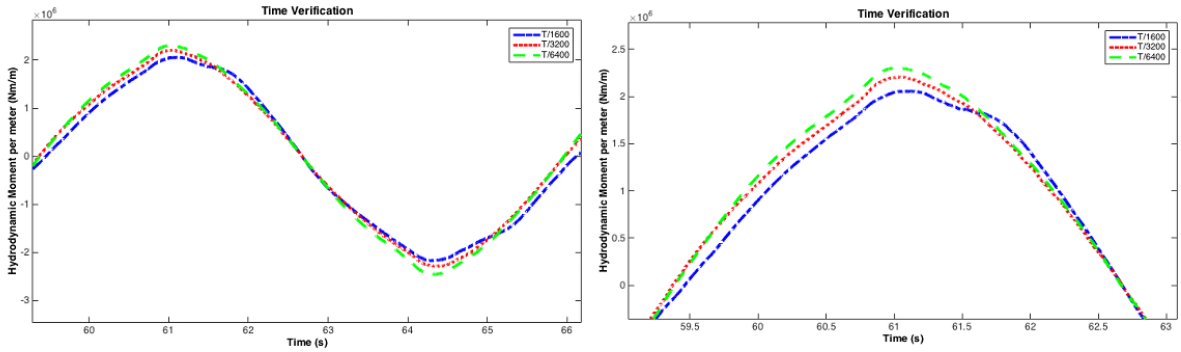

Figure 5.5: Time verification study for the full-scale barge

It can be seen that the model is more sensitive to the timestep than to the grid size. However, the hydrodynamic moment is still converging and thus $T/3200$ is chosen for further calculations.

5.3. Results

It is important to mention that the selected center of rotation is the VCG and not the center of floatation, in order to calculate the viscous roll damping in agreement with the potential theory algorithms. More specifically, all potential theory algorithms have as a point of reference the CoG and consequently all the motions are described based on this point. Moreover, the VCG above the water line, in combination with the other 6 degrees of freedom, makes this choice more realistic, as in these cases the free-floating body tends to rotate around the VCG.

Initially case 1, where the draft is equal to 35% of the total height, is examined. As it is mentioned, various roll amplitudes are examined, ranging from 5^o to 17.5^o. Figure 5.6 presents the influence of the roll amplitude on the hydrodynamic moment.

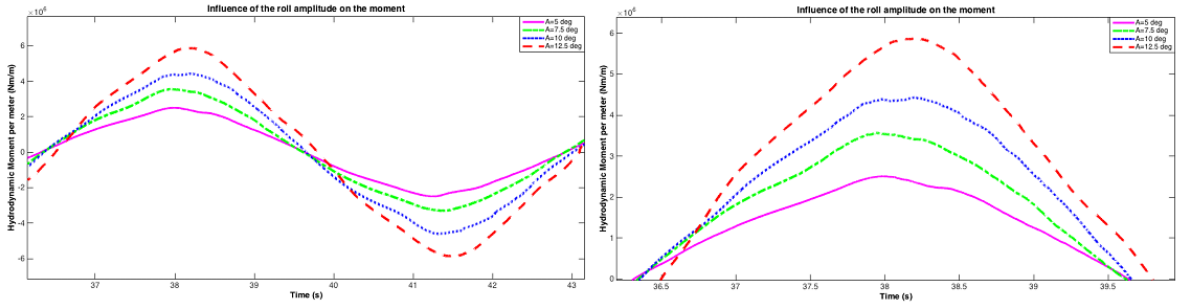

Figure 5.6: Influence of the roll amplitude on the hydrodynamic moment for the first case of full-scale barge

It can be seen that the amplitude of the hydrodynamic moment is increasing as the roll amplitude becomes larger. Furthermore, the phase of the moment curve, for roll amplitude up to 10^o, appears not to be significantly affected. Nevertheless, for roll amplitude equal to 12.5^o (or larger), the phase shift is significant.

Afterwards, the roll damping coefficients are calculated for each roll amplitude, founded on the discrete Fourier series method. Figure 5.7 illustrates the dimensionless viscous roll damping coefficients for various roll amplitudes and shows the relation between the viscous, wave, and total roll damping.

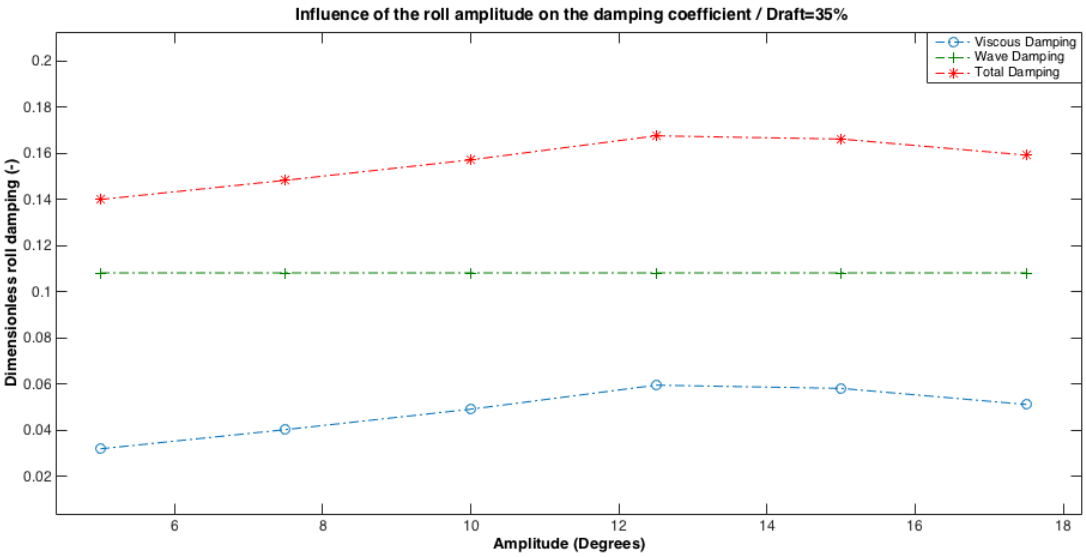

Figure 5.7: Influence of the roll amplitude on the dimensionless damping coefficients for the first case of the full scale barge

It can be seen that the viscous roll damping increases linearly as the roll amplitude becomes larger. However, this linear trend stops when roll amplitude reaches 12.5^o. After this point the viscous roll damping decreases with increasing roll amplitude. The main reason for this is the fact that in such roll amplitudes, the velocity of the barge (when it crosses the starting point) becomes extremely high and as a consequence the separation of vortices become highly intense and the created vortices end-up either away of the imaginary submerged area (in reality, in cases like these the vortices are dissipated at the free surface) or close to the axis of rotation (which means decreased lever arm). These leads decreased damping moment.

In addition, the viscous roll damping ranges between 30% and 55% of the wave damping. Table 5.3 shows the percentage of the viscous roll damping with respect to the wave damping for various roll amplitudes.

Amplitude	**Percentage of the third harmonic**
5^o	29.40%
7.5^o	37.15%
10^o	45.34%
12.5^o	54.98%
15^o	53.69%
17.5^o	47.23%

Table 5.3: Percentage of viscous roll damping with respect to the wave roll damping, for the first case of the full scale barge

Finally, Figure 5.8 presents the FFT of the hydrodynamic moment for different roll amplitudes. In all cases, the third harmonic component of the moment is less than 6% of the first harmonic and for this reason the equivalent linear damping is accurate enough.

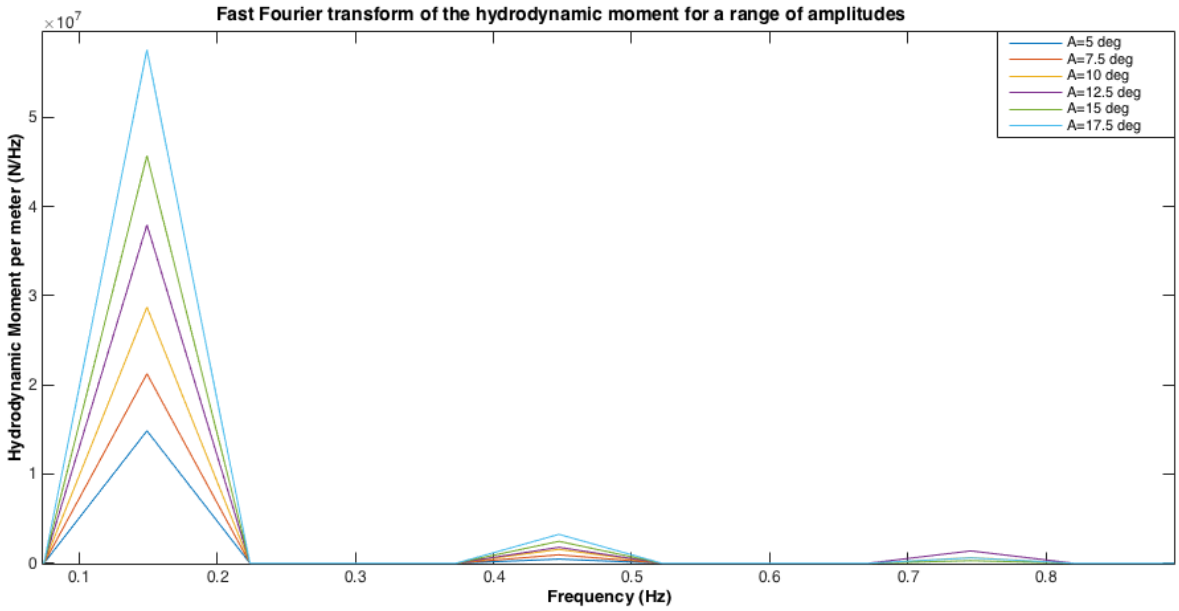

Figure 5.8: Fast Fourier transform of the hydrodynamic moment for a range of amplitudes for the first case of the full scale barge

Figure 5.9 and Figure 5.10 illustrate the influence of roll amplitude on damping coefficients, for the second and third case of the full scale barge respectively. Moreover, Table 5.4 and Table 5.5 present the percentage of viscous roll damping with respect to the wave damping for various roll amplitudes, for the second and third case respectively.

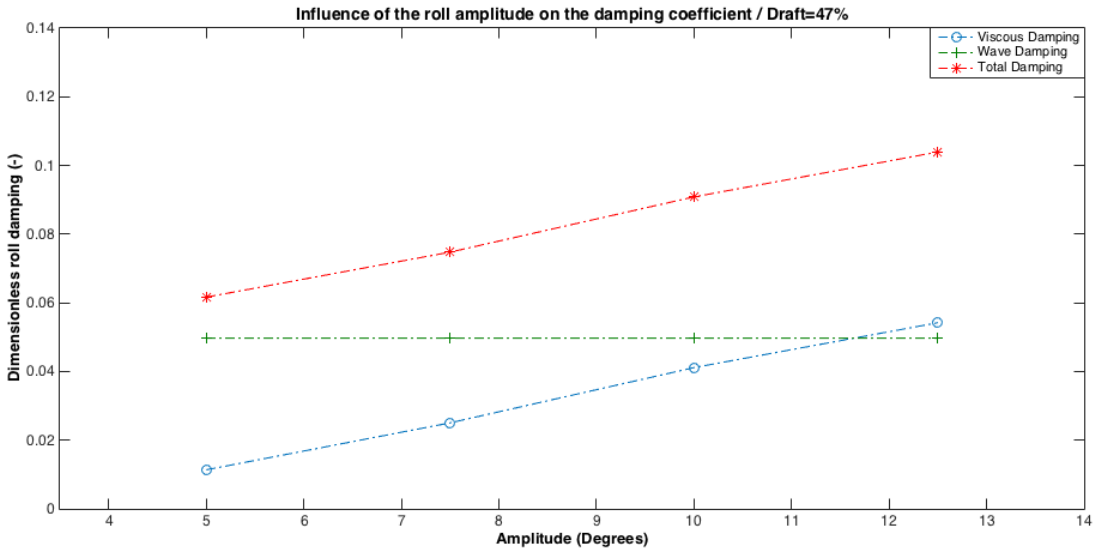

Figure 5.9: Influence of roll amplitude on dimensionless damping coefficients for the second case of the full scale barge

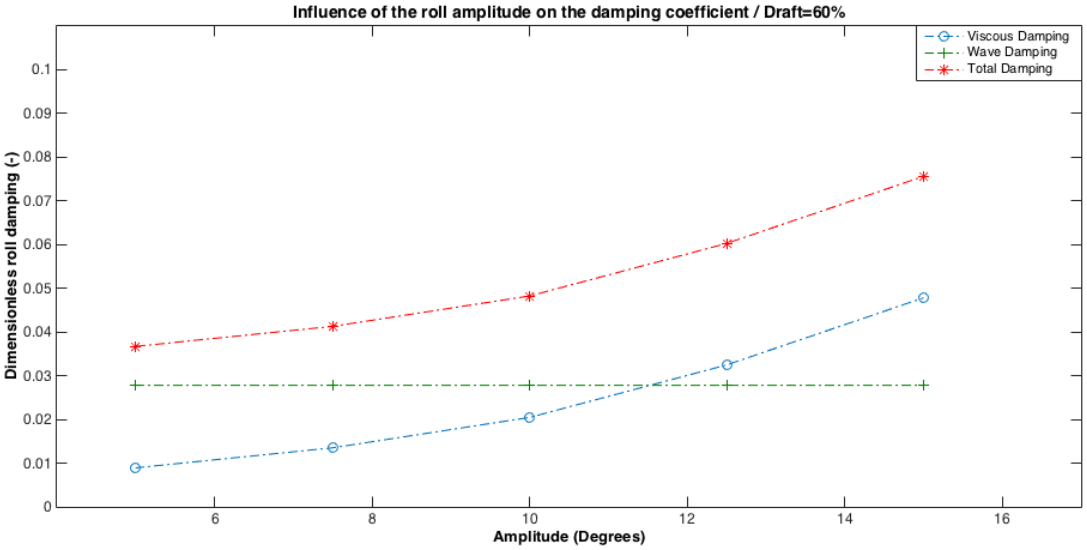

Figure 5.10: Influence of the roll amplitude on the dimensionless damping coefficients for the third case of the full scale barge

Amplitude	Percentage of the third harmonic
5^o	24%
7.5^o	50.37%
10^o	82.73%
12.5^o	109.91%

Table 5.4: Percentage of viscous roll damping with respect to the wave roll damping, for the second case of the full scale barge

Amplitude	Percentage of the third harmonic
5^o	32.13%
7.5^o	48.61%
10^o	73.63%
12.5^o	116.86%
15^o	172.09%

Table 5.5: Percentage of viscous roll damping with respect to the wave roll damping, for the third case of the full scale barge

In the second case (draft equal to the 47% of the total height) the dimensionless roll damping is linear with roll amplitude, for the examined amplitudes of oscillation. Additionally, the percentages of viscous roll damping with respect to the wave damping, are significantly higher compared to the first case. More specifically, for roll amplitude equal to 10^o, the percentage of viscous damping in the first case is equal to 45.34%, while in the second is 82.73%. This might happen because of two possible reasons:

- The frequency of oscillation is higher in the first case and for this reason the wave damping component is also bigger. Thus, it could be conclude that the increase in frequency of oscillations, results in a more significant increase in the wave damping component than in the viscous damping part
- The VCG is higher in the second case than in the first and for this reason the barge in the second case performs a pendulum like motion (as the VCG is selected as the center of rotation). For this reason, the bottom of the structure remains at the horizontal position for more time and thus the separated vortices are able to stay attached for longer period. This could lead to increase of the viscous damping component compared to the first case.

However, the described approaches are based on assumptions and for this reason should be further investigated and validated.

In the third case, damping coefficients are not entirely linear with roll amplitude. In the equation that describes the relation between the damping coefficients and the roll amplitude, a quadratic term should be included. This indicates (based on equation (3.31)) that the cubic damping term (b_3) is of high importance for this particular case.

6

Conclusions and Recommendations

6.1. Conclusions

In this section, the main conclusions of this thesis are summarized and categorized into the following subsections:

- General conclusions and remarks
- Numerical discretisation and viscous flow modelling
- Turbulence modelling
- Equivalent linearised and nonlinear roll damping

6.1.1. General conclusions and remarks

Three main approaches were examined in order to estimate by means of turbulent viscous flow simulations the hydrodynamic moment due to forced oscillation motion and calculate the roll damping coefficients. In two out of the three approaches the free surface was included in the model using the VoF method. In the first case, relaxation zones were used in order to absorb the reflected waves, and thus to decrease the size of the computational domain. In the second case, the influence of the reflected waves to the roll damping calculation was avoided by creating larger computational domain. In the third and final approach, free surface effects were neglected and only the viscous roll damping part was estimated. The total damping was calculated as a superposition of viscous damping (from viscous flow algorithm) and wave damping (potential theory algorithm).

All approaches were tested and compared with Ikeda's experimental data [27] and it is concluded that roll damping coefficients can be accurately estimated using both the second and the third methodology. This means that the viscous flow model can correctly calculate roll damping, either when the free surface effect is included (VoF modelling) or when excluded (by adding wave damping from potential theory algorithms). In more detail, the submerged case is a good compromise between computational time and accuracy. However, this method violates the physics of roll damping since it is linearly separated into several components. The method using free surface and larger domain (excluding relaxation zones) is time consuming (since it requires bigger domain) but it accurately describes the physical phenomenon. The first method (smaller domain with relaxation zones) considerably overestimated the damping coefficients, as the relaxation zones were too close to the hull and thus the numerical results were affected by their existence.

Finally, it is important to mention that as the roll amplitude increases, the generated vortices at the bilges and the third harmonic component (3ω) of the damping moment also grow, for all the examined cases.

6.1.2. Numerical discretisation and viscous flow modelling

A second order time discretisation scheme was attempted to be used, in order to increase the accuracy of the time discretisation of the momentum equation and decrease the resolution in time. However, it was impossible to stabilize it and incorporate it in the model. The second order schemes tend to be even more unstable for cases with free surface.

Additionally, free surface modelling, in viscous flow algorithms, is highly sensitive to high aspect ratio cells, mesh deformations and non-orthogonality. These can lead to artificially high velocities and high pressures at the free surface and at the boundary of the hull. As a consequence, the accuracy of the numerical results can be reduced.

6.1.3. Turbulence modelling and verification studies

Three RANS turbulence models ($k-\omega$ SST (low-Reynolds and high-Reynolds number modes), $kkl-\omega$ and $k-\varepsilon$ Realizable) were extensively examined in order to capture the physical phenomena of the forced roll motion. The main conclusion deriving from this research is that each turbulence model should be wisely used based on every considered case. As an example, refer to subsection 4.1.3., where the $k-\varepsilon$ Realizable model is used in order to capture the vortex creation due to roll motion, for a relatively small structure. In the examined case, a high Reynolds number turbulence model (which requires a y^+ higher than 30 and thus in the examined case a course mesh), is used for a low Reynolds number case. This resulted in vortex distortion and incorrect physical interpretation of separation of flow (Figure (4.15) and Figure (4.16)). On the other hand, the $kkl-\omega$ model was proven to be a robust and stable turbulence model for low-Reynolds number cases and for this reason it was finally chosen for Ikeda's validation case. More specifically, the hydrodynamic moment for $kkl-\omega$ model converged in space for $y^+ = 1.32$ and in time for $dt = T/1600$. For the full scale barge, the $k-\omega$ SST model (in high Reynolds number mode) is used, as it is the best proven option for full scale engineering applications.

An important aspect is that the $k-\omega$ SST turbulence model proved to be sensitive to the initial and boundary conditions of the turbulent quantities (k and ω), as it is described in subsection 4.1.1 and by Figure (4.11). In particular, higher initial ratio of k/ω (higher than normal) leads to higher eddy viscosity and therefore to artificial damping creation and more turbulent flow. This results in reduced hydrodynamic moment as the separation and vortex creation levels are lower. For this reason, it can be concluded that the initial and boundary condition of the turbulent quantities k and ω should be carefully selected, based on empirical and semi-empirical formulas [46, 64].

6.1.4. Equivalent linearised and nonlinear roll damping

The equivalent linearized and non-linear form of roll damping was calculated for all the examined cases, for variant amplitudes and period of oscillation $T = 1s$, and compared with the data of Ikeda [27].

The equivalent linearised damping coefficients, for the larger domain (excluding relaxation zones) and the submerged case, are in good agreement with literature data [27]. More specifically, regarding the case with extended domain, a deviation from the experimental values lower than 10% is observed. In addition, for the submerged approach, a reasonable agreement between the viscous flow model and the experimental results is found, with difference less than 7%. On the other hand, for the case with the smaller domain (including relaxation zones), the calculated dimensionless damping coefficients are overestimated. Specifically, the damping coefficients are overestimated by 20% with respect to the experimental results of Ikeda [27] due to the fact that the flow field close to the hull interacts with the relaxation zones. Finally, for the submerged case, the equivalent linearised damping, for period of oscillation $T = 1.5s$ and various amplitudes, is estimated and has good agreement with the experimental data (Figure (4.28)).

For the free surface case with smaller domain, the coefficients for the nonlinear representation of roll damping are significantly overestimated, similar to the linearised equivalent damping coefficient. For the submerged case, the coefficient b_1 is overestimated by over 43%. This significant error occurred due to the fact that the free surface is neglected and the wave damping, which is a big part of the coefficient b_1, is artificially implemented in the total equivalent damping coefficient. The nonlinear coefficient b_2 differs from the experimental value by 12.28%, which is a realistic deviation. Finally, for the free surface case with larger domain, the damping coefficients b_1 and b_2 diverge from the experimental data by approximately 6% and 9.5%, respectively.

Three different cases of the full scale barge are examined, with drafts equal to 35%, 47%, and 60% of the total height. These cases are simulated by using the submerged approach, as it is a good compromise of time efficiency and accuracy. Each case has a different total Vertical Center of Gravity (VCG) as it is presented in Figure (5.1). The roll damping of the full-scale barge, for draft equal to 35% of the total height, tends to linearly increase with the roll amplitude up to the point where the roll amplitude reaches a value equal to 12.5^o. After this point the roll damping decreases with respect to the roll amplitude. The main reason for this is the fact that in such roll amplitudes, the created vortices end-up either away from the imaginary submerged area or close to the axis of rotation. These leads decreased damping moment. In the second case the dimensionless roll damping is linear with roll amplitude, for all the examined amplitudes of oscillation. Moreover, the percentages of viscous roll damping with respect to the wave damping, are significantly higher compared to the first case. In the third case, damping coefficients are not entirely linear with roll amplitude. The equation that describes the relation between the damping coefficients and the roll amplitude should include a quadratic term. This indicates (based on equation (3.31)) that the cubic damping term is of high importance for this particular case.

6.2. Recommendations

The recommendations for future work and research, which emerged during this master thesis, are classified into the following two sub-sections:

- Body dynamics and
- Fluid dynamics and numerical modelling.

6.2.1. Body dynamics

- ✓ In a loaded transportation barge the total center of gravity is located above the waterline. This might cause strong coupling between the roll and sway motion. This significant coupling influences the viscous roll damping as well as the coupled damping terms (b_{42} and b_{24}). As it is impractical to examine this phenomenon experimentally it is of high importance to investigate the accuracy with which viscous flow simulations capture the physics of this case.
- ✓ As the amplitude of the roll motion increases, the third harmonic component (3ω) of the total damping force becomes more important. In cases like this, the equivalent linearised approach can be very well insufficient for the intergraded calculation of the damping coefficients. For this reason, other extraction techniques should be investigated and used.
- ✓ The shape of the hull influences the vortex shedding considerably and therefore the viscous roll damping. For this reason, it is of high importance to investigate the impact of different hull shapes on the viscous damping coefficient. Viscous flow simulations can effectively and accurately provide an overview of this correlation.
- ✓ For increased VCG a floating body performs a pendulum like motion. It is of high importance to examine the influence of this unique motion on the vortex creation and thus on the viscous roll damping.
- ✓ It is of high significance to examine in more detail the behaviour of roll damping for variable frequency of oscillation, while the roll amplitude will remain constant.

6.2.2. Fluid dynamics and numerical modelling

- ✓ Richardson extrapolation is a powerful acceleration method, which is used in order to improve the rate of convergence of a sequence. This method can be used in order to increase the order of accuracy of the obtained roll damping coefficients. Thus, Richardson interpolation for different time-steps and grid-sizes is an efficient approach to obtain a higher order of accuracy of a damping coefficient.
- ✓ As it is repeatedly mentioned, the free surface is highly sensitive to the mesh quality and this can influence the accuracy of the results. However, the true source of this sensitivity might be the fact that the discretisation of the Navier-Stokes equations, in the current viscous flow algorithm, is based on their conservative form. As it is mentioned in section 3.3, density is discontinuous at the interface (because the phase fraction alpha is also discontinuous) and thus its value rapidly decreases (or increases) when the fluid phase changes. When the conservative form of the Navier-Stokes equations is discretised, density is included in the discretisation, and as a result this discontinuity affects the momentum. This results in artificially high velocities at the free surface. Finally, it is important to mention that the creators of VoF (Hirt and Nichols [24]) are using the non-conservative form of the Navier-Stokes equations. For this reason, the non-conservative form of Navier-Stokes equations should be examined for cases with free surface.
- ✓ The accuracy of time discretisation of the momentum equation is of high importance in order to correctly estimate the solution and thus the damping coefficients. An increased level of temporal accuracy can be achieved by using a higher order discretisation or higher resolution in time. The current simulations where performed for a first order temporal discretisation and for this reason a main future goal is to stabilize a higher order scheme in time (like Crank-Nicolson), in order to reduce the computational time and increase the accuracy of the solution.
- ✓ Turbulence modelling for roll damping determination has been extensively examined in the current thesis. However, the used RANS models are not designed for this type of physical phenomenon. The ideal turbulence model should be able to capture accurately flow separation, transitional flows and vortex creation. Moreover, it should be independent of the initial values of the turbulent quantities. The most suitable turbulence model for the described physical phenomena is LES (Large Eddy Simulation) and for this reason it should be investigated in the future in order to predict the flow field due to roll motion.

A

Appendix

A.1. Reynolds averaging technique

Osborne Reynolds proposed an averaging technique in order to describe the chaotic behaviour of a fluid's velocity in a turbulent flow. More specifically he expressed the velocity of a turbulent flow as a summation an average value and a fluctuation around this average value A.1.

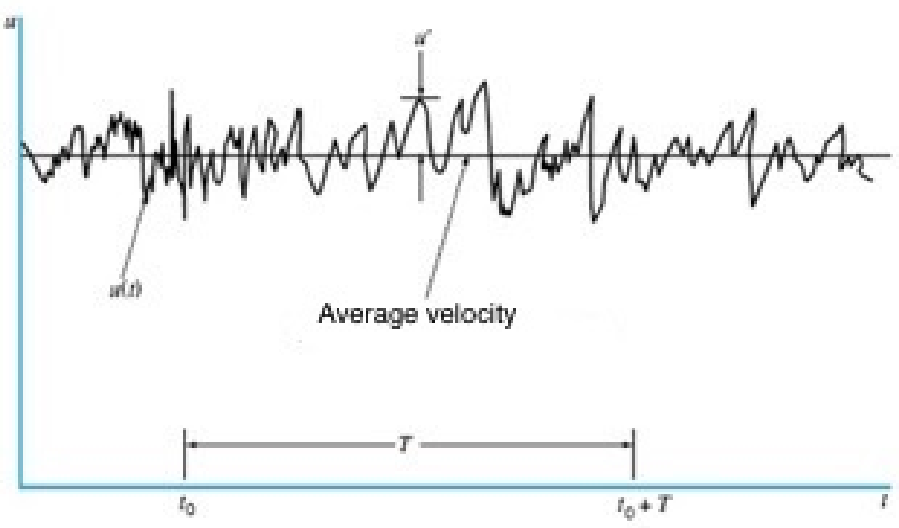

Figure A.1: Velocity of turbulent flow

$$u(x,t) = \bar{u}(x) + u'(x,t) = U + u' \tag{A.1}$$

$$\bar{u}(x) = lim\frac{1}{T}\int u(x,t)dt \tag{A.2}$$

B

Appendix

B.1. Boundary conditions

In the following tables, the boundary conditions for the free surface and the submerged cases for the $kkl-\omega$ are specified.

	U	p_rgh	alpha	k/kl	ω	ν_t
Barge	movingWall Velocity	fixedFluxPressure	zeroGradient	zeroGradient	zeroGradient	ν_tLowRe
Walls	slip	zeroGradient	zeroGradient	zeroGradient	zeroGradient	zeroGradient
Atmosphere	pressureInlet OutletVelocity	totalPressure	inletOutlet	inletOutlet	inletOutlet	calculated
Front/Back	empty	empty	empty	empty	empty	empty

Table B.1: Implemented boundary conditions in the viscous flow algorithm for free surface case and $kkl-\omega$ turbulence model

	U	p_rgh	k/kl	ω	ν_t
Barge	movingWall Velocity	fixedFluxPressure	zeroGradient	zeroGradient	ν_tLowRe
Up/ Down	zeroGradient	fixedValue (0)	zeroGradient	zeroGradient	zeroGradient
Front/Back	empty	empty	empty	empty	empty

Table B.2: Implemented boundary conditions in the viscous flow algorithm for submerged case and $kkl-\omega$ turbulence model

fixedValue: It is a Dirichlet boundary condition. More specifically, this boundary condition provides a fixed value constraint at the chosen boundary.

movingWallVelocity: It is a Dirichlet boundary condition. This type of boundary condition provides a velocity boundary condition in the cases of moving walls. It similar to the fixed value boundary condition, nevertheless the velocity value of the boundary is variable and based on other conditions (specified by the user or by the "environment")

zeroGradient: It is a Neumann boundary condition. This means that, a zero gradient condition (normal special derivative to the boundary) is applied from the internal field onto the patch face. In the pressure case, this is not an actual boundary condition, but a result of the Navier-Stokes equations at the boundary for specified fixed-value velocity boundary condition.

fixedFluxPressure: It is a Neumann boundary condition. It is similar to the zeroGradient condition for the pressure. The difference is that this condition is suitable for variable velocity boundary condition. This means that the pressure gradient is calculated based on the velocity, which is specified by the respective boundary condition.

totalPressure: This boundary condition provide a total pressure condition. (explain)

inletOutlet: This boundary condition provides a generic outflow condition, with specified inflow for the case of return flow. (explain)

pressureInletOutletVelocity: This velocity inlet / outlet boundary condition is applied to pressure boundaries where the pressure is specified. A zero-gradient condtion is applied for the outflow (as defined by the flux). For the inflow, the velocity is obtained from the patch-face normal component of the internal-cell value. (explain)

calculated: In this boundary condition, it is assumed that the value is assigned (calculated) via field assignment.

empty: OpenFoam always creates 3D cases. This boundary condition is used in order to reduce a case from 3D to 2D. For this reason, the empty boundary condition is used to the faces, in which no solution is needed.

nutLowReWallFunction: It is a wall function boundary condition for the ν_t. For further explanation about the wall functions.

B.2. Numerical schemes

In OpenFoam the mathematical operators (in this equation and generally) can be expressed with the following way in:

ddtScheme: first and second time derivatives $\Rightarrow \frac{\partial}{\partial t}, \frac{\partial^2}{\partial^2 t}$

gradScheme: gradient $\Rightarrow \nabla$

divScheme: divergence $\Rightarrow \nabla\bullet$

laplacianScheme: Laplacian $\Rightarrow \nabla^2$

interpolationScheme: cell to face interpolations of values

snGradSchemes: component of gradient normal to a cell face

Its differential operator can be discretized using many possible ways. Below, the chosen schemes (for each mathematical operator group) are presented.

ddtScheme	gradScheme	laplacianScheme	interpolationScheme	snGradSchemes
Euler	cellLimited Gauss linear 1	Gauss linear corrected	linear	corrected

div(rhoPhi,U)	div(phi,alpha)	div(phirb, alpha)	div(phi,k) / div(phi, epsilon)	div(phi, nuTilda)	div((muEff* dev(T(grad(U)))))
Gauss linearUpwind	Gauss vanLeer	Gauss interfaceCompression	Gauss linearUpwind	Gauss linear	Gauss linear

Bibliography

[1] Ahmed S., Duan, W. Y. 'Forced Roll Simulations and Ship Roll Damping Computations using URANS' . Islamabad, Pakistan: 13th Internation Bhurban Conference on Applied Sciences & Technology (2016, Junuary 12-16).

[2] Atkins Research and Development & National Maritime Institute. 'Barge Motions Research Project: Phase 2 Report Part 1, Forced Rolling Tests in Still Water, for a Consortium of Companies Organised by Noble Denton and Associated Ltd'. Deft University of Technology (1979, April).

[3] Atkins Research and Development & Der Norske Veritas. 'Barge Motions Research Project: Phase 2 Report Part 2, Comparison of Hydrodynamic Coefficients Calculated by Different Computer Programs'. Deft University of Technology (1979, October).

[4] Bonfliglio, L., Brizzolara, S. & Chryssostomidis, C. 'Added Mass and Damping of Oscillating Bodies: a fully viscous numerical approach'. Recent Advances in Fluid Mechanics, Heat & Mass Transfer and Biology.

[5] Bonfliglio, L., Vernengo, G., Brizzolara, S. & Bruzzone, D. 'A Hybrid RANSE - Strip Theory Method for Prediction of Ship Motions'. Maritime Technology and Engineering III, pp.241-250 (2016, June).

[6] Chakrabarti, S. 'Empirical Calculation of Roll Damping for Ships and Barges'. International Journal of Marine Energy 28, 915–932 (2001).

[7] Chakrabarti, S. K. 'Hydordynamics of Offshore Structures'. Computational Mechanics Publications (1987).

[8] Charles, H. 'Numerical Computation of Internal and External Flows', Volume 1, Fundamentals of Computational Fluid Dynamics. ELSEVIER (2007).

[9] Chanony, F. - Marin. 'Validation and verification of FreSCo for viscous flows around oscillating bodies - Roll motion'.(2009, September 11).

[10] Chen, H. & Christensen, E. D. 'Computation of Added and Damping Coefficients of a Horizontal Circular Cylinder in openFOAM'. Proceedings of the ASME 2016 35th International Conference on Ocean, Offshore and Arctic Engineering, Busan, Korea (2016, June 19-24).

[11] Chen, L., Sun, L., Zang, J., Hillis, A. J. & Plummer, A. R. 'Numerical Study of Roll Motion of a 2-D Floating Structure in Viscous Flow'. Journal of Hydrodynamics ELSEVIER (2015, July).

[12] Crepier, P. 'Validation of URANS CFD Code ReFRESCO Roll Damping Simulations'. Promotion ENSI, Naval Architecture and Offshore Engineering (2011).

[13] Damián, S. M. 'Description and Utilization of interFoam Multiphase Solver' - Final Work - Computational Fluid Dynamics.

[14] Davis, P. L., Rinehimer, A. T. & Uddin, M. 'A Comparison of RANS-Based Turbulence Modeling for Flow over a Wall-Mounted Square Cylinder'. 20th Annual Conference of the CFD Society of Canada, At Canmore, Alberta, Canada (2012, May).

[15] Eslamdoost, A. 'Roll Motion of a Box and Interaction with Free Surface. Project work for the PhD course in OpenFOAM'. Gothenburg, Sweden (2009, December).

[16] Falzarano, J., Somayajula, A. & Seah, R. 'An overview of the prediction methods for roll damping of ships'. USA: Techno-Press, Ltd. (2015, May 8).

[17] Ferziger, J. & Peric, M. 'Computational Methods for Fluid Dynamics', 3rd Edition. New York: Springer (2002).

[18] Furst. 'Numerical Simulation of Transitional flows with laminar kinetic energy'. 18th International Conference, ENGINEERING MECHANICS 2012, pp. 309-315 (2012, May 14-17).

[19] Hajiarab, M. 'Roll Damping Prediction of a Free Floating Barge' - PhD thesis. Newcastle, UK: School of Marine Science and Technology (2013, April).

[20] Handschel, S. & Abdel-Maksoud, M. 'Improvement of the Harmonic Excited Roll Motion Technique for Estimating Roll Damping'. Ship Technology Research (2016, November 22).

[21] Handschel, S., Feder, D. F. & Abdel-Maksoud, M. 'Estimation of Ship Roll Damping - a Comparison of the Decay and the Harmonic Excited Roll Motion Technique for a Post Panamax Container Ship'. Proceedings of the 12th International Conference on the Stability of Ships and Ocean Vehicles. Glasgow, UK (2015, June 14-19).

[22] Hemida, H. 'OpenFOAM tutorial: Free surface tutorial using interFoam and rasInterFoam'. Goteborg, Sweden (2008, April 14).

[23] Himeno, Y. 'Prediction of Ship Roll Damping - State of Art'. Michigan: The University of Michigan (1981).

[24] Hirt, C. & Nichols, B. 'Volume of Fluid (VOF) Method for the Dynamics of Free Boundaries'. Journal of Computational Physics 39, 201–225 (1981).

[25] Huang, J & Stern, F. 'Coupled Ghost Fluid/Two-phase Level Set Method for Curvilinear Body-fitted Grids'. International Journal for Numerical Mthods in Fluids (2007, November).

[26] Ikeda, Y., Fujiwara, T. & Katayama, T. 'Roll Damping of a Sharp-Cornered Barge and Roll Control by a New-Type Stabilizer'. Singapore: Proceedings of the Third International Offshore and Polar Engineering Conference (1993, June 6-11).

[27] Ikeda, Y., Himeno, Y. & Tanaka, N. 'On Eddy Making Component of Roll Damping Force on Naked Hull'. Journal of the Society of Naval Architects of Japan (1997).

[28] Irkal Mohsin, A. R., Nallayarasu, S. & Bhattacharyya, S. K. 'CFD approach to roll damping of ship with bilge keel with experimental validation'. Applied Ocean Research (ELSEVIER). Chennai, India (2015).

[29] Irkal Mohsin A. R., Nallayarasu, S. & Bhattacharyya, S. K. 'Experimental and CFD simulation of roll motion of ship with bilge keel'. International Conference on Computational and Experimental Marine Hydrodynamics (2014).

[30] ITTC. 'Numerical Estimation of Roll Damping'. International Towing Tank Conference (2011).

[31] Jacobsen, N. G. 'Wave2foam Manual'. Deltares, The Netherlands (2017, August).

[32] Jacobsen, N. G., Fuhrman, D. R. & Fredsoe, J. 'A Wave Generation Toolbox for the Open-source CFD Library: OpenFoam®'. International Journal for Numerical Methods in Fluids (2011).

[33] Jaouen, F., Koop, A. H. & Vaz, G. 'Prediction Roll Added Mass and Damping of a Ship Hull Section Using CFD'. Rotterdam, The Netherlands: Proceedings of ASME 30th International Conference on Ocean, Offshore and Arctic Engineering (2011, June 19-24).

[34] Jaouen, F., Koop, A. H., Vas, G. & Crepier, P. 'RANS Predictions of Roll Viscous Damping of Ship Hull Sections'. Wageningen, The Netherlands: V International Conference on Computational Methods in Marine Engineering (2011, Junuary).

[35] Jasak, H. 'Dynamic Mesh Handling in OpenFOAM'. 47th AIAA Aerospace Sciences Meeting Including The New Horizons Forum and Aerospace Exposition. Orlando, Florida (2009, January 5 - 8).

[36] Jasak, H. & Turovic, Z. 'Automatic mesh motion for the unstructured Finite Volume Method' (2006, November).

[37] Jasak, H. & Turovic, Z. 'Dynamic Mesh Handling in openFOAM Applied to Fluid - Structure Interaction Simulations'. V European Conference on Computational Fluid Dynamics. Lisbon, Portugal (2010, June).

[38] Journée, J. M. J., Massie, W. W. 'Offshore Hydrodynamics'. Delft University of Technology (2001, January).

[39] Katayama, T., Yildiz, B. & Umeda, J. 'Numerical Estimation and Validation of Shallow Draft Effect on Roll Damping'. The 14th International Ship Stability Workshop (ISSW), Kuala Lumpur, Malaysia (2014).

[40] Kawahara, Y., Maekawa, K. & Ikeda, Y. 'A Simple Prediction Formula of Roll Damping of Conventional Cargo Ships on the Basis of Ikeda's Method and Its Limitation'. Journal of Shipping and Ocean Engineering , pp. 201-210 (2002).

[41] Kok, J. C. 'Resolving the dependence on free-stream values for the k-omega turbulence model'. AIAA Journal (1999, July).

[42] Korpus, R. A. & Falzarano, J. M. 'Prediction of Viscous Ship Roll Damping by Unsteady Naver-Stokes Techniques' (1997, May).

[43] Lavrov, A., Rodrigues, J. M., Gadelho, J. F. M., Guedes Soares, C. 'Calculation of Hydrodynamic Coefficients of Ship Sections in Roll Motion Using Navier-Stokes Equations'. Centre for Marine Technology and Ocean Engineering (CENTEC) 133(2017)36-46 ELSEVIER (2017).

[44] Menon, S. 'Coupled Level-Set with VOF interFoam. CFD with OpenSource software' - A course at Chalmers University of Technology (2016, Junaury 15).

[45] Menter, F. R., 'Two-Equation Eddy-Viscosity Turbulence Models for Engineering Applications', AIAA Journal, vol. 32, no 8. pp. 1598-1605 (1994).

[46] Menter, F. R., 'Zonal Two Equation k-ω Turbulence Models for Aerodynamic Flows', AIAA Paper 93-2906 (1993).

[47] Metrikine, A. 'Dynamics, Slender Structures and an Introduction to Continuum Mechanics CT 4145'. Delft, The Netherlands: Lecture Notes.

[48] Moradnia, P. 'Project Work for the PhD Course in OpenFOAM, A tutorial on how to use Dynamic Mesh solver IcoDyMFOAM'. Göteborg - Sweden (2008).

[49] Moukalled, F., Mangani, L. & Darwish, M. 'The Finite Volume Method in Computation Fluid Dynamics'. Switzerland: Springer (2016).

[50] Piehl, H. R. 'Ship Roll Damping Analysis'- Dissertation University Duisburg-Essen (2016, April 22).

[51] Pope, S. B. 'Turbulent Flows'. Cambridge University Press.

[52] Rusche, H. 'Computational Fluid Dynamics of Dispersed Two-phase Flows at High Phase Fractions' - PhD thesis. Imperial College of Science, Technology & Medicine, London (2002, December).

[53] Sarkar, T. & Vassalos, D. 'A RANS-based Technique for Simulation of the Flow Near a Rolling Cylinder at the Free Surface'. Journal of Marine Science and Technology (2000).

[54] Tryggvason, G., Scardovelli, R. & Zaleski, S. 'Direct Numerical Simulations of Gas-liquid Multiphase Flows'. Cambridge University Press (2011).

[55] Van't Veer, R. & Fathi, F. 'On the roll damping of an FPSO with riser balcony and bilge keels'. RINA William Froude Conference: Advances in Theoretical and Applied Hydrodynamics, Portsmouth, United Kingdom (2010).

[56] Versteeg H. K. & Malalasekera W. 'An Introduction to Computational Flyid Dynamics, The Finite Volume Method'. Longman Scientific & Technical (1995).

[57] Vugts, J. H. 'The Hydrodynamics Coefficients for Swaying Heaving and Rolling Cylinders in a Free Surface'.

[58] Vugts, J. H. 'The Hydrodynamics Forces and Ship Motions in Waves'.

[59] Vukcevic, V., Jasak, H. & Gatin, I. 'Implementation of the Ghost Fluid Method for free surface flows in polyhedral Finite Volume framework'. Computer and Fluids, ELSEVIER (2016, May)

[60] Wassermann, S., Feder, D. F. & Abdel-Maksoud, M. 'Estimation of ship roll damping-A comparison of the decay and the harmonic excited roll motion technique for a post panamax container ship'. ELSEVIER (2015, November 25).

[61] Wemmenhove, R. 'Numerical Simulation of Two-Phase Flow in Offshore Environments' (1982, June).

[62] Wesseling, P. 'Principles of Computational Fluid Dynamics'. Delft: Springer Series in Computation Mechanics (2009).

[63] Wesseling, P. 'Elements of Computational Fluid Dynamics'. Delft, The Netherlands: Lecture notes (2011, September).

[64] Wilcox, D. C. 'Turbulence Flow for CFD'. California: DCW Industries (2006).

[65] Yakhot, V., Orszag, S. A., Thangam, S., Gatsaki, T. B. & Speziale, C. G. 'Development of Turbulance Models for Shear Flows by a Double Expansion Technique' American Institute of Physics (1992, July).

[66] Yang, B., Wang, Z. C. & Wu, M. 'Numerical Simulation of Naval Ship's Roll Damping Based on CFD'. Dalian Naval Academy. China (2012).

[67] Yeung, R. W., Liao, S. W. & Roddier, D. 'On Roll Hydrodynamics of Rectangular Cylinders'. Proceedings of the 8^{th} International Offshore and Polar Engineering Conference, Montreal, Canada (1988, May 24-29).

[68] Yıldız, B., Cakıcı, F., Katayama, T. & Yılmaz, H. 'URANS prediction of roll damping for a ship hull section at shallow draft'. Springer (2015, July).

[69] Zhou, Y.H., Ma, N., Shi, X., Zhang, C. 'Direct calculation method of roll damping based on three-dimensional CFD approach'. Journal of Hydrodynamics (2013, August 24).